Accurate Nonempirical Range-Separated Hybrid van der Waals Density Functional for Complex Molecular Problems, Solids, and Surfaces

Vivekanand Shukla[1,†] Yang Jiao[1,†] Jung-Hoon Lee[2,3] Elsebeth Schröder[1]
Jeffrey B. Neaton[4,5,6] and Per Hyldgaard[1,*]

[1]*Department of Microtechnology and Nanoscience-MC2,*
Chalmers University of Technology, SE-41296 Gothenburg, Sweden
[2]*Computational Science Research Center, Korea Institute of Science and Technology,*
Seoul 02792, Republic of Korea
[3]*Molecular Foundry, Lawrence Berkeley National Laboratory, Berkeley, California 94720-7300, USA*
[4]*Materials Sciences Division, Lawrence Berkeley National Laboratory,*
Berkeley, California 94720-7300, USA
[5]*Department of Physics, University of California, Berkeley, California 94720-7300, USA*
[6]*Kavli Energy NanoScience Institute at Berkeley, Berkeley, California 94720-7300, USA*

We introduce a new, general-purpose, range-separated hybrid van der Waals density functional termed vdW-DF2-ahbr within the nonempirical vdW-DF method [Hyldgaard, *et al. J. Phys. Condens. Matter* **32,** 393001 (2020)]. It combines a correlation from vdW-DF2 with a screened Fock exchange that is fixed by a new model of exchange effects in the density-explicit vdW-DF-b86r or rev-vdW-DF2 functional [Hamada, Phys. Rev. B **89,** 121103(R) (2014)]. The new vdW-DF2-ahbr prevents spurious exchange binding and has a small-density-gradient form set from many-body perturbation analysis. It is accurate for bulk as well as layered materials, and it systematically and significantly improves the performance of the present vdW-DFs for molecular problems. Importantly, vdW-DF2-ahbr also outperforms present-standard (dispersion-corrected) range-separated hybrids on a broad collection of noncovalent-interaction benchmark sets, while at the same time successfully mitigating the density-driven errors that often affect the description of molecular transition states and isomerization calculations. vdW-DF2-ahbr furthermore improves on state-of-the-art density-functional-theory approaches by succeeding at challenging problems. For example, it (1) correctly predicts both the substrate structure and the site preference for CO adsorption on Pt(111), (2) it outperforms existing nonempirical vdW-DFs for the description of CO_2 adsorption in both a functionalized and in a simple metal-organic framework, and (3) it is highly accurate for the set of base-pair interactions in a model of DNA assembly.

I. INTRODUCTION

The van der Waals density-functional (vdW-DF) method [1–18] for strictly nonempirical density-functional theory (DFT) has been successfully applied in materials and chemistry for more than two decades. vdW-DF [4,5,19,20] opened the door for early DFT predictions of adhesion among graphene sheets and in lubricants [4], weak molecular binding [21–27], and the weak adhesion of nucleic bases and other organics on graphene and oxides [28–30].

The functionals of the vdW-DF method have no empirical parameters and avoid double counting of correlation. Predating the set of also popular dispersion-corrected DFTs [31–41], the accuracy and robustness have systematically improved over time.

The success of vdW-DF motivates continued investments to design even better nonempirical versions of vdW-DF. The vdW-DF method is built from many-body perturbation theory (MBPT) analysis of the nature of the fully interacting electron ground state. This strategy led, for example, to a straightforward extension to include spin [13,18]. We can also directly interpret the quality and performance differences in terms of the spatial variation in and hence nature of the different contributions to the exchange-correlation (XC) energy [42–44].

The vdW-DF method provides a formally exact framework for a systematic inclusion of nonlocal-correlation effects [43]. Part of the MBPT foundation for the vdW-DF

*hyldgaar@chalmers.se
†These authors contributed equally to this work.

method [1–3,5,7,9,12,43,45,46] was first described in the same paper that established logic for correlations in the constraint-based generalized-gradient approximation (GGA) [46]. As such, it represents a third generation of XC-energy functionals in an electron-gas tradition that started with the local spin-density approximation [47–49] (LDA) and led to the highly successful Perdew-Burke-Enzerhof (PBE) [50] and PBEsol [51] GGAs. The overall logic of this tradition is to gradually introduce a controlled increase in flexibility so that we can reliably benefit from more of the pool of physics insight and trusted MBPT inputs [5,7,8,43,45,46,52,53].

Finding an accurate general-purpose functional is important since theory often concerns complex materials, i.e., systems where the atomic structure is not fully established. There, DFT calculations must be used to first assert which are the most plausible of several candidate motifs, for example, as in Ref. [44]. The consistent-exchange vdW-DF-cx version [10] (abbreviated CX) is crafted to seek high accuracy simultaneously for molecules, bulk, and surfaces [11], but (as discussed elsewhere [43]) it uses a type of XC guidelines [7,46,54] that favor dense-matter and noncovalent (NOC) interaction problems [17,18,43,55]. The vdW-DF2-b86r (abbreviated B86R) [56] uses a different nonlocal correlation [8] but retains and, in fact, enhances the general-purpose character [55]. Other vdW-DFs [5,8,16,57–61] often perform best for a more limited range of problem types [55] (see Supplemental Material [62] for an illustration of molecular-performance variations and Table SI for a list of functional abbreviations that we systematically use below). All of the vdW-DFs, including the unscreened-hybrid forms [14,15], fail in some cases to correctly balance vdW attraction with the repulsion provided by the gradient correction to exchange [4,20,63,64], for example, in complex metal-organic-framework systems [44]. Nevertheless, in DFT we seek to characterize and predict molecular-reaction energies and transition barriers at the 1-kcal/mol (or 43-meV) limit that defines so-called chemical accuracy [65–69]. Higher accuracy still is needed to understand chemical fuels [8,70–74], CO_2 capture [44,75–81], batteries [82–85], and biochemistry [18,26,86,87]. These are cases where we must understand the role of NOC interactions [69] as they act in concert and competition [11,29,88]. To secure reliable characterizations and to correctly assert the relevant structural motifs in complex materials, we must correctly balance the XC terms in just one general purpose, yet highly accurate, vdW-DF design that also avoids density-driven DFT errors [44,89,90].

This paper reports the design and testing of a range-separated hybrid (RSH) vdW-DF. It is termed vdW-DF2-ahbr and abbreviated AHBR because it builds on the vdW-DF2 nonlocal-correlation description and an analytical-hole (AH) analysis [17,91] of the nature of exchange in the B86R variant [56]. We show that it stands out by having an exceptional general-purpose capability and clearly outperforms even the recent AHCX design of a RSH vdW-DF [17], for reasons we explain.

Figure 1 summarizes our assessment of performance over broad molecular properties, illustrating that AHBR is both highly accurate and has an excellent transferability. We find that AHBR can navigate generic density-driven functional errors [89,90,92] that, for example, often affect molecular transition states.

We propose that the new AHBR be used to test the status of the vdW-DF method, as we also partly illustrate, because it is free of a performance bias. The performance of RSH HSE + D3 [93–95] is independent of the benchmark type in the very broad GMTKN55 suite [69] on broad molecular properties. The unscreened-hybrid B3LYP + D3 [95–97] is an improvement over HSE + D3 on molecular transition states and NOC interactions but not across the board [69]; see Supplemental Material Tables SII and SIII [62]. HSE + D3 and B3LYP + D3 are widely used in materials science and chemistry, respectively, and their transferability set the bar for the generic vdW-DF method testing. The new RSH AHBR (black curve in Fig. 1) outperforms HSE + D3 (gray) across all types of molecular properties and matches (clearly improves) the B3LYP + D3 performance [69] for the important group 3 of molecular transition-state benchmarks (for the rest of the GMTKN55 benchmarks). As summarized in Fig. S1 and documented in Tables SII and SIII of the Supplemental Material [62], these observations hold for either of the weighted-mean-absolute-deviation measures that are suggested and used in Ref. [69]. Unlike AHCX (dark red), AHBR is more successful than HSE + D3 and B3LYP + D3 on, for example, the BH76 benchmark set on molecular-barrier heights, problems that are sensitive to density-driven DFT errors [89,90]. The AHBR provides systematic accuracy gains over present-standard hybrid choices.

The specific contributions of the paper can be summarized as follows. We first complete a robust plane-wave-based assessment across the full GMTKN55 benchmark suite [69], documenting that the unscreened-hybrid extension [14] of B86R abbreviated DF2-BR0 provides the best performance on molecular properties. This is true for the GMTKN55 suite and among all of the vdW-DFs including the RSH vdW-DFs in Fig. S2 of the Supplemental Material [62]. Our broad documentation is consistent with a very recent independent observation for proton transition barriers [98]. We proceed to define the AHBR, the RSH generalization of DF2-BR0, using an AH characterization for exchange effects in B86R. We validate that AHBR is an exceptional performer across GMTKN55, Fig. 1, and retains a strong performance for bulk and some layered materials. Finally, we illustrate the usefulness of AHBR for DNA assembly and molecular adsorption problems, finding good agreement on quantum-chemistry reference calculations, the correct site preference for the CO/Pt(111) problem, and good performance for characterization of CO_2 uptake in two metal-organic frameworks (MOFs) [44,75,78,81].
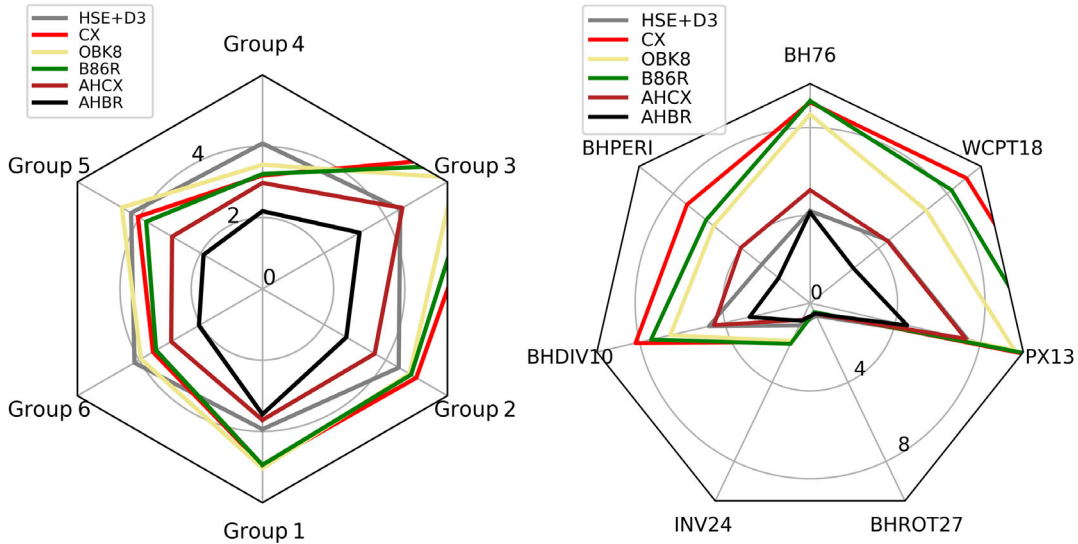
FIG. 1. Performance comparison of vdW-DFs as averaged over the six groups of molecular benchmarks in the GMTKN55 suite [69] (left panel) and as tracked for individual transition-state benchmark sets of group 3 (right panel): barrier-height benchmarks for small and cyclic molecules (with labels BH76 and BHPERI), for diverse, inversion, and rotation processes (with labels BHDIV10, INV24, and BHROT27, respectively), as well as for proton exchange and transfer problems (labels PX13 and WCPT18). The GMTKN55 suite also probes performance on small-system reaction energies (group 1), large-system reaction energies and isomerizations (group 2), as well as total, inter-, and intramolecular noncovalent interactions (groups 6, 4, and 5, respectively). We report mean absolute deviations (MADs) in kcal/mol compared with coupled-cluster reference energies at reference geometries [69]. For comparison, we also include an assessment of dispersion-corrected HSE + D3 [69,93–95] and the recently defined RSH vdW-DF-ahcx (abbreviated AHCX) [17]. Regular functionals exemplified by the three vdW-DFs with best overall molecule performance, CX [10], B86R [56], and vdW-DF-optB88 (or optB88-vdW, abbreviated OBK8) [57], are often challenged by density-driven DFT errors [90] in such problems.

The rest of the paper is organized as follows. The theory Sec. II presents an overview of the vdW-DF method, analysis of the B86R-exchange hole, and contains the formulation of the new AHBR. Section III contains our results and includes a discussion, including illustrations of AHBR accuracy. Section IV contains our conclusion and outlook. The paper has two appendixes giving computational details, including the electrostatic-environment approach used to complete plane-wave benchmarking across the GMTKN55 suite.

II. THEORY

Central in MBPT and in the electron-gas foundation of DFT [46,48,99–103] is the screened density response $\delta n(\omega)$ to some external-potential change $\delta \Phi_{\text{ext}}^{\omega}$ oscillating at frequency ω. In MBPT, we can, at least in principle, compute the nonlocal response function $\chi_\lambda(\mathbf{r}, \mathbf{r}'; \omega) \equiv \delta n(\mathbf{r})/\delta \Phi_{\text{ext}}^{\omega}(\mathbf{r}')$, often expressed as a function of a complex frequency $\omega = iu$. We can also do that at a range of an assumed reduced strength $0 < \lambda < 1$ of the electron-electron interaction $\lambda \hat{V}$. Assuming access to this knowledge, the adiabatic connection formula (ACF) permits an exact determination

$$E_{\text{XC}} = - \int_0^1 d\lambda \int_0^\infty \frac{du}{2\pi} \text{Tr}\{\chi_\lambda(iu)V\} - E_{\text{self}}, \quad (1)$$

of the XC-energy functional E_{XC}. Here, $V = |\mathbf{r} - \mathbf{r}'|^{-1}$ denotes the matrix element of the electron-electron interaction $\hat{V}$, u is an imaginary frequency argument in the response description, while the last term is the electron self-energy $E_{\text{self}} = \text{Tr}\{\hat{n}V\}/2$. The expressions for E_{XC} and E_{self} involve Coulomb-weighted traces, that is, integrations in spatial coordinates of $|\mathbf{r} - \mathbf{r}'|^{-1}$ times $\chi_\lambda(\mathbf{r}', \mathbf{r}; \omega)$ and times the electron density $n(\mathbf{r}')$, respectively. Also, we (at every coupling-constant value λ) add an auxiliary potential that keeps the electron density $n(\mathbf{r})$ unchanged across the implied adiabatic turn-on of the electron-electron interaction $\hat{V}_\lambda = \lambda \hat{V}$. The actual XC potential used in the Kohn-Sham (KS) scheme for efficient DFT calculations is simply the $\lambda \to 0$ limit of this auxiliary potential. It is given by a functional derivative of the XC energy, as discussed many places elsewhere.

In MBPT, we compute the response functions $\chi_\lambda(\omega)$ as a ground-state expectation value of correlations between density fluctuations [104]. As such, $\chi_\lambda(\omega)$ is directly reflecting the Lindhard-type screening that exists in the electron gas at assumed coupling constant λ, as discussed, for example, in Ref. [43]. The screening is given by the dielectric function $\kappa_\lambda(\omega) = (1 + \lambda V \chi_\lambda)^{-1}$. For practical DFT, we seek XC-functional approximations that contain the most pertinent physics content of the widely complex, many-body interacting processes that define $\chi_\lambda(iu)$. The massive DFT usage allows us to get successively more

adept at this as long as we stay systematic and can interpret performance differences, for example, within MBPT.

In the electron-gas tradition for XC-functional designs [5,7,12,17,43,46,48,100,101,103,105–108], we focus the discussion on the XC hole $n_{XC}(\mathbf{r}; \mathbf{r}')$ that results from a complex-frequency integration over $\chi_\lambda(iu)$. The XC hole $n_{XC}(\mathbf{r}; \mathbf{r}')$ expresses the tendency for a given electron at position $\mathbf{r}$ to suppress the electron occupation at neighboring positions $\mathbf{r}'$. Importantly, the introduction of this hole permits an ACF-based interpretation of the XC-energy functional [9,48,100],

$$E_{XC} = \frac{1}{2} \int_{\mathbf{r}} \int_{\mathbf{r}'} \frac{n(\mathbf{r}) n_{XC}(\mathbf{r}; \mathbf{r}')}{|\mathbf{r} - \mathbf{r}'|} \qquad (2)$$

that has analogies in electrostatics. However, the XC hole reflects the impact of zero-point dynamics, i.e., virtual collective (plasmon) excitations in the electron distribution [43,45,101,109].

The exchange-hole component $n_x(\mathbf{r}; \mathbf{r}')$ of this total XC hole describes the impact of Pauli exclusion. The Fock-exchange approximation $n_x^{Fo}(\mathbf{r}; \mathbf{r}')$ to n_x results from considering one-particle density matrices formed from the KS-wave-function solutions, for example, as summarized in the discussion provided in Ref. [17].

A. The vdW-DF framework

To begin our summary of vdW-DF, we note that since LDA and GGAs are completely set from a modeling of an underlying XC hole [9,17,48,100,101,110,111], we are also ready to capture vdW forces as defined from an electrodynamics coupling of electron-density fluctuations [4,9,43,45,46,105,112,113]. Any XC functional can be seen as the net binding energy of the electrons and associated XC holes, Eq. (2). However, it is also clear that the electron and the associated (GGA-type) XC hole form an antenna of charged parts that have a mutual zero-point energy dynamics. The electron-XC-hole pairs will interact even across regions that have but a sparse or no electron density [71,114]. In fact, this electron-gas electrodynamics coupling [1,2,9,43,45,46,115] is a systematic generalization of the original London picture of dispersion forces among noble-gas atoms [112,116].

The vdW-DF method achieves a systematic extension of MBPT-based GGAs by recasting the exact XC functional as an electrodynamics problem [3,9,43,117,118], while counting (via a frequency contour integration) the coupling-induced shifts in energies for collective excitations [9,101,113]. Thus, for the vdW-DF XC-energy description, we rely on a formally exact recast of the ACF result [9,12,43],

$$E_{XC} = \int_0^\infty \frac{du}{2\pi} \mathrm{Tr}\{\ln[\kappa_{ACF}(iu)]\} - E_{self}. \qquad (3)$$

In Eq. (3), we introduce an effective, spatially nonlocal, dielectric functional function $\kappa_{ACF}(iu)$. The formal XC evaluation is given as a weighted λ average of $\kappa_\lambda(\omega)$ and hence of χ_λ [9,12,43], and there is full equivalence of Eqs. (1) and (3), given consistent approximations. The recast is also equivalent to the XC-hole [48,100] formulation, Eq. (2). The electrodynamical recast, Eq. (3), simplifies the porting of the ideas of the cumulant expansion [119,120] to vdW-DF development work. Specifically, we can link the Ashcroft-Langreth-Lundqvist picture of vdW-binding contributions [1,45,46,105,108] and the MBPT input to the constraint-based GGAs [9,46,50,51,101]. In turn this allows the vdW-DF method to provide an effective (MBPT-guided) approximation to the λ-averaged response description, Eq. (3), as discussed in Refs. [5,7,9,12,13,43].

In the vdW-DF method, we furthermore use a so-called internal functional E_{XC}^{in} to first set a lowest-order (GGA-level) approximation for the screening. The screening is described by a truly nonlocal dielectric function $\epsilon(\omega)$ (but we suppress spatial coordinates in this discussion). This dielectric function has collective excitations, plasmons, that set the start of the response modeling given by an effective electron-gas susceptibility $\alpha(\omega) = [\epsilon(\omega) - 1]/4\pi$ [9,12,101]. First, we approximate the plasmon propagator as $S_{XC}(\omega) = \ln[\epsilon(\omega)]$ and rely on an explicit two-pole approximation that reflects plausible assumptions and all plasmon-related conservation laws [5,43]. Next, the formal relation

$$E_{XC}^{in} = \int_0^\infty \frac{du}{2\pi} \mathrm{Tr}\{\ln[\epsilon(\omega)]\} - E_{self} \qquad (4)$$

sets the details of the plasmon dispersion as the implied contour integration naturally sums the plasmon-pole contributions as ln singularities [9,43,101,113]. In summary, we have a formal link between the GGA-level internal functional and structure of the starting approximation $S_{XC}(\omega)$ for an emerging description of the actual plasmon dynamics [5,43].

We also explicitly enforce a longitudinal projection of the response in the dielectrics approximation function

$$\kappa_{ACF}(\omega) = -\nabla \cdot \epsilon(\omega) \nabla V / 4\pi. \qquad (5)$$

We note that having this projection inside the recast ACF, Eq. (4), produces terms that capture the vdW attraction as described in the presence of electron-gas screening [43]. Moreover, the use of $\epsilon(\omega) = \exp[S_{XC}(\omega)]$ implies a cumulant-or-cluster-expansion logic [119–123] in the response description [43]. This allows the vdW-DF method to also pick up high-order susceptibility and screening effects [9,43], i.e., balance the vdW attraction by other nonlocal-correlation effects [43].

Finally, given the choice of GGA-level plasmon modeling, Eq. (4), we repeat the contour integration evaluation with Eqs. (3) and (5) to secure efficient kernel-based evaluation of nonlocal-correlation energies [5,6]. This approach means that the vdW-DF versions have no discernible cost increase

over GGA in plane-wave codes [86,124–126]. Similarly, the new class of RSH vdW-DFs [17] has the same costs as the HSE [91,93,94], i.e., a RSH that is based on the PBE [50] GGA. However, the use of the vdW-DFs sometimes requires a better convergence of the electron-density variation [57,60,126].

The resulting nonempirical vdW-DF description stands out, for example, in the class of vdW-inclusive functionals by treating all interaction contributions on the same electron-gas footing. We avoid auxiliary inputs beyond ground-state DFT and all need for semiempirical adjustments, for example, to ameliorate double counting of nonlocal correlations. The vdW-DF method is set up to describe vdW interactions as they emerge in concert and competition with covalent and ionic binding [11] and with orbital-interaction shifts produced by wider nonlocal-correlation effects [43,119,120]. The latter effects are, for example, documented to counteract contributions to vdW interaction contributions from the high-density regions near the nuclei as well as from the saddle point of the electron-density variation that exists between fragments [42,43]. Noting that formal MBPT sets the nature of the exact XC energy, we seek to use the MBPT as a guide [5,7]. This is done, for example, by trying to recycle [5,6,8,9,43,45,46,103,105] the accuracy gains that were made on the exchange description in the MBPT-based GGAs [46,50,51,101,103,110,127,128].

B. vdW-DF versions

Prior vdW-DF versions [4,5,8,13,14,17] involve a controlled introduction of systematic design changes. For example, vdW-DF1 [5–7] and vdW-DF2 [8] have the same overall structure but differ in whether we prioritize MBPT or scaling insight on exchange [7,8,103,127] to model the collective-excitation response that forms the starting point of the E_c^{NL} evaluation. They also differ in how we enforce [4,12,64,110] a method criterion that the actual exchange component of a vdW-DF should not itself lead to spurious weak binding [63,64], since the vdW attraction is a correlation effect [129].

For a computationally efficient evaluation [5,124], the standard general-geometry formulation expands the recast ACF, Eq. (3), to second order in the (nonlocal) plasmon propagator $S_{\mathrm{XC}}(\omega) = \ln[\epsilon(\omega)]$ [5,7,43]. Formally, the expansion is written

$$E_{\mathrm{XC}}^{\mathrm{DFs}} \approx E_{\mathrm{XC}}^{\mathrm{in}} + E_c^{\mathrm{NL}} \qquad (6)$$

$$E_c^{\mathrm{NL}} = \int_0^\infty \frac{du}{4\pi} \mathrm{Tr}\{S_{\mathrm{XC}}^2(iu) - (\nabla S_{\mathrm{XC}} \cdot \nabla V/4\pi)^2\}, \qquad (7)$$

where $E_{\mathrm{XC}}^{\mathrm{in}}$ and Eq. (4) set the details of $S_{\mathrm{XC}}(iu)$ [5,12].

In all present vdW-DFs, the internal $E_{\mathrm{XC}}^{\mathrm{in}}$ functional is chosen semilocal (GGA-like), comprising LDA correlation and a simple choice of physics-motivated gradient-corrected exchange [5,8,46,127]. This choice avoids double counting of nonlocal correlations [5,12,43]. The gradient-exchange

choices used in $E_{\mathrm{XC}}^{\mathrm{in}}$ are defined by formal-MBPT input. That input is used through the Langreth-Perdew and Langreth-Vosko (LV) analysis of a screened-exchange nature [5,7,54,103] (that is natural for bulk and metals) in the first general-geometry release vdW-DF1. It is set as the Schwinger exact-exchange-scaling analysis [8,127] in the second vdW-DF2. The Schwinger MBPT result is instead relevant for capturing exchange effects in molecules [8]. This fact is, for example, revealed by a demonstration that it leads to a nonempirical derivation of Becke-88 exchange [131] when interpreted in the GGA framework [132].

The ACF foundation, Eqs. (3)–(5), motivates the use of Eq. (6) to pick the exchange [43]. That is, we should ideally use the internal-exchange formulation, and hence, the $S_{\mathrm{XC}}(iu)$ form, to also define the actual exchange. However, the inner functional is deliberately kept simple, while the overall exchange design must also reflect other considerations. Taken together, these observations mean that it is presently not possible to directly implement this idea. The general-geometry vdW-DFs therefore have a looser connection between the XC terms,

$$E_{\mathrm{XC}}^{\mathrm{DFs}} \equiv E_{\mathrm{XC}}^0 + E_c^{\mathrm{NL}}, \qquad (8)$$

where $E_{\mathrm{XC}}^0 = E_{\mathrm{XC}}^{\mathrm{in}} + \delta E_x^0$ permitting a crossover term δE_x^0, even if it is not compatible with the ACF [43].

The top panel of Fig. 2 compares the so-called exchange-enhancement factor F_x that defines the nature of the
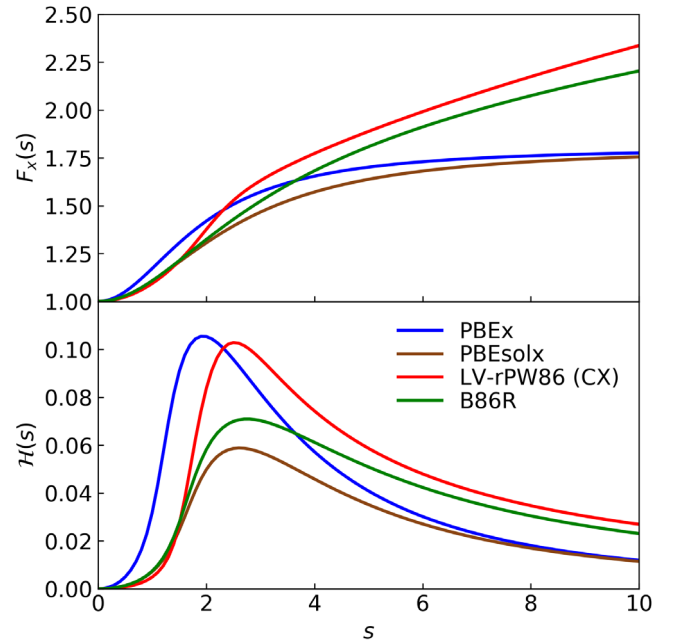

FIG. 2. Comparison of exchange-enhancement factor $F_x(s)$ (top panel) and of the Gaussian-exponent prefactor $\mathcal{H}(s)$ that determines the main damping in the AH modeling for the density-density correlation defining the underlying exchange holes [17,91].

gradient-corrected exchange in all GGA descriptions as well as in present vdW-DFs. We show the variation with the scaled density gradient $s = |\nabla n|/(2nk_F)$ [where $k_F = (3\pi^2 n)^{1/3}$ is the local Fermi wave vector] for the four XC-functional cases that are of interest here. The exchange energy in any semilocal (GGA-type) approximation, that the present vdW-DFs also use, must take the form [133]

$$E_x^{\text{GGA}} = \int_{\mathbf{r}} n(\mathbf{r}) \epsilon_x^{\text{LDA}}(n(\mathbf{r})) F_x(s(\mathbf{r})). \qquad (9)$$

Here, $\epsilon_x^{\text{LDA}} = -3k_F/4\pi$ denotes the LDA exchange result, i.e., the exchange-energy-per-particle value that characterizes a homogeneous system [at density $n = n(\mathbf{r})$]. The variations in this gradient-corrected exchange are thus set alone by the enhancement form of factor $F_x(s)$. For $E_{\text{XC}}^{\text{in}}$, the enhancement is set as a quadratic expansion $F_x^{\text{in}}(s) = 1 + \mu s^2$; see Refs. [5,7,8].

Exchange descriptions of the popular constraint-based GGAs arise when one imposes an exchange-hole-conservation criterion in the modeling of density gradient effects. This was first done in the (revised) PW86 [64,110]. It was repeated in the popular PBE [50] and PBEsol [51] designs while then also paying attention to preventing the exchange-hole depth from dramatically exceeding the local-electron density. The PBE and PBEsol also adhere to a local implementation of the so-called Lieb-Oxford bound [134,135] on the high-s $F_x(s)$ variation, but the actual (globally implemented) bound does not, in practice, impacts this discussion of picking a robust GGA-type (or hybrid-type) exchange for the vdW-DFs [4,17,64].

For the vdW-DFs, we must craft an asymptotic $F_x(s)$ behavior that produces an adequate but not excessive repulsion by gradient corrections to exchange for weakly interacting molecules [4,44,63,64,88]. This is to ideally eliminate (without overcompensating) spurious weak-system binding by the errors in the LDA exchange description [4,63,64].

The actual exchange descriptions in vdW-DF1 and vdW-DF2 are set as in the revPBE [136] variant of PBE and as the refitted PW86 form [64], respectively. In both cases, the selections are made following analysis of the weak binding of noble-gas and small-molecule dimers; see Refs. [4,64]. Both of these exchange choices are more repulsive than the PBE exchange; i.e., they have a gradient correction to exchange that gives a stronger push to separating fragments. That extra repulsion is needed [44,64] since, in the vdW-DFs, we are also upgrading to a truly nonlocal-correlation description E_c^{NL}. That new term includes vdW forces [43] and gives a stronger attraction mechanism than what exists in PBE.

The CX [9,10,43], and hence, with the CX0P and AHCX hybrid extensions [15], aligns the two ways that exchange insight underpins the vdW-DF details, in the inner functional E_{XC}^0 and in Eq. (8), as far as possible. The idea is to

look at the impact of XC balance on the binding-energy descriptions instead of on the total-energy descriptions [10]. The move to reconcile the inner and actual exchange has the benefit that we use the Lindhard-screening logic implied in the expansion Eqs. (6) and (7), as well as current conservation [9,43], to effectively balance XC terms.

Our general design strategy is to maximize the role of MBPT inputs, like Lindhard screening, because it is a promising path to securing high accuracy broadly in one general-purpose XC design [101,137,138]. In formal MBPT, we summarize the net impact on the electron-electron interactions in terms of a so-called self-energy term $\Sigma_{\text{XC}}(\mathbf{r}, \mathbf{r}', \omega)$. It determines how single-electron excitations propagate in the fully interacting system [43,101,137,138]. It plays a similar role as the DFT exchange-correlation potential $v_{\text{XC}}(\mathbf{r}) = \delta E_{\text{XC}}/\delta n(\mathbf{r})$ that defines the independent-particle dynamics of the DFT representation of the same system (except that it is both frequency dependent and truly nonlocal) [47,138]. A key argument for the vdW-DF design strategy is that the formal-MBPT description of the total energy is tolerant [137]; i.e., one can get good results even when interaction effects are merely approximated by perturbation theory for the self-energies $\Sigma_{\text{XC}}(\mathbf{r}, \mathbf{r}', \omega)$. We get a sound electron-response description as long as we keep those (so-called skeleton) diagrams that capture the essential physics and dominant features of the electron-gas response [7,43,45–47,101,103,105,138]. Also, in principle, that robustness extends to the choice of E_{XC}, thanks to the Sham-Schlüter relation between $v_{\text{XC}}(\mathbf{r})$ and $\Sigma_{\text{XC}}(\mathbf{r}, \mathbf{r}', \omega)$ [138].

It is important to observe, however, that we do not in CX (or in AHCX) enforce a complete exchange alignment for all types of problems. The Lindhard screening and current conservation are essential parts of the ACF result for the exact XC functional [43]. The CX and associated hybrid designs allow us to use this idea, but only for descriptions of system processes where the important density changes are set by density regions with moderate values $s \lesssim 2.5$ [10]. This criterion, i.e., that relevant binding or process-energy contributions to the XC-energy differences should converge relatively fast with s [10,43,44,139], holds for typical bulk and surface problems [43,88,140], where the use of the CX, CX0P, AHCX tool chain is suggested [17,18]. It is a welcome bonus for CX and AHCX that the CX criterion (and CX accuracy) often seems to hold also for many molecular problems [10,17,43,44,141,142]. However, there are also cases where we can document a large binding impact of density changes and where the interaction problem is not completely set by low-to-moderate s values. This happens for CO_2 uptake in a diamine-functionalized MOF [44].

The fact that there is a condition on the CX and AHCX implementation of the Lindhard logic also suggests a potential susceptibility to density-driven errors [90,92]. Such errors undercut overall arguments for a generic XC

robustness of CX and AHCX, at least for the systems where the sensitivity is identified [90,143]. The translation of MBPT robustness [137] into XC-design robustness is vulnerable because the Sham-Schlüter equation [138] also includes factors, i.e., independent-particle Green's functions G_0, that are set by KS energy levels and by the spatial variation in the KS orbitals that arise in the XC approximation. In order for an XC approximation to inherit the $\Sigma_{XC}(\mathbf{r}, \mathbf{r}', \omega)$ robustness, it should deliver a near-exact density variation. Also, density-driven errors emerge, for example, by self-interaction error (SIE) effects in negatively charged ions [89], and they can, as such, reflect large density changes [44]. The CX and AHCX rely on the ACF [43], but once the CX usage is pushed beyond the small-to-moderate-s criterion [10,44], the consistency benefit is gone. The inherent Lindhard-screening logic and current-conservation mechanism are then no longer able to enforce an automatic XC-hole conversation on the LV-exchange description [43]. While the high-s form of CX exchange, i.e., the rPW86, also reflects a separately implemented (older) XC-hole conservation criterion [64,110], the strong MBPT connection is lost. In this type of large-s problem, we expect that the use of modern constraint-based PBE and PBEsol exchange would be the safer approach. In summary, we cannot expect that CX (and hence, AHCX) will always remain a robust choice.

C. The logic of the B86R variant

Improvement in accuracy generally followed from coupling the vdW-DF1 and vdW-DF2 correlation to other (less repulsive) exchange choices, for example, with the suggestions for OBK8, C09, OB86, B86R, and vdW-BEEF variants [56,57,59,60,144]. The same is true for the CX release (and formal spin and hybrid extensions [13–15,17,18,43]) that uses a Lindhard-screening logic to balance the XC components in typical binding cases [10]. The balance question is also central for the DF3-opt1 and DF3-opt2 designs [16]. Some of these vdW-DFs emphasize MBPT input on the gradient correction to exchange [7,10,56,59,101,103].

The introduction of variants has advantages for illustrating usefulness but complicates the search for further systematic progress. The variants (as well as CX) enhanced the range of applications that can easily be addressed with the vdW-DF method (beyond the reach of vdW-DF1 and vdW-DF2), as summarized in a number of reviews [12,43,71,81,145] as well as perspectives [65,66,146]. However, flexible variants might effectively be compensating for possible E_c^{NL} limitations since they fit the choice of δE_x^0 to a target or expected representative application [57,58,144,147]. Having too much flexibility can diffuse the underlying drive for seeking increasingly more versatile XC functionals: We could inadvertently be hiding an actual method limitation.

Nevertheless, for our overall XC development goals, we need to supplement CX and AHCX by a new RSH

vdW-DF that is more robust toward density-driven errors. Unfortunately, simply creating a RSH vdW-DF right off of vdW-DF2 (from an analysis in Ref. [17]) in a design termed DF2-AH, does not meet the need. This is made clear in the Supplemental Material [62] with observations summarized in the discussion below.

Fortunately, the B86R variant of vdW-DF2 does offer a realistic path to craft a new general-purpose nonempirical RSH vdW-DF, the AHBR. Importantly, as we explain below, the AHBR and B86R also offer a valuable contrast to AHCX and CX when it comes to prioritizing among possible MBPT inputs. That is, the combination of AHBR and AHCX gives us an option for a controlled "functional-derivative" or "functional-contrast" analysis: We can interpret and learn from observations of performance variations in terms of well-understood design differences. A similar idea of making a functional-difference analysis was also explored for adsorption studies in Refs. [88,115]. Nicely enough, we discover that the resulting AHBR design also has a better-than-AHCX resilience toward the density-driven errors in molecular-barrier-height problems as well as in some large-system isomerization problems; see Fig. 1 and Ref. [90].

In practice, our AHBR development work starts from inspecting the B86R exchange and by providing an AH modeling of the B86R-exchange hole, adapting Ref. [91]. This work is an extension of the analysis presented for CX and for vdW-DF2 (and revisited for PBE and PBEsol) in Ref. [17]. Like vdW-DF2 and CX, the B86R respects the lesson [64] that the asymptotic form of the exchange-enhancement factor should rise as $s^{2/5}$ asymptotically to appropriately counteract errors in the exchange contributions to (weak) binding [63]. The B86R accomplishes that by relying on a revised Becke86b exchange [56,148]. It is fully characterized by the exchange enhancement

$$F_x^{B86R}(s) = 1 + \frac{\mu_{GEA} s^2}{(1 + \mu_{GEA} s^2/\kappa)^{4/5}}, \qquad (10)$$

where $\mu_{GEA} = 10/81$ is the small-s expansion coefficient. This low-s form is aligned with the correct gradient-expansion result from a diagrammatic MBPT analysis [51,54,101], when interaction lines are interpreted as bare Coulomb matrix elements [51,103,149,150]. In contrast, the LV (and hence, CX) exchange results when screened interaction lines are used when evaluating the same diagrams [46,103]. We also note that the use of $\kappa = 0.7114 < 1$ in Eq. (10) implies a smaller prefactor on the asymptote $F_X(s) \sim s^{2/5}$ than what applies for CX and OB86 [10,60].

Since B86R relies on vdW-DF2 correlation, it has only a weaker consistency in that both exchange and correlation energies are set by MBPT inputs that are valid for molecular-type problems. As noted above, the E_c^{NL} is here set from a Schwinger exchange-scaling argument from

which one can derive Becke88 exchange [132], while the μ_{GEA} value ignores higher-order screening effects for setting gradient-corrected exchange [103]. The exchange enhancement of the internal functional is set as $F_x(s) = 1 + 0.2097s^2$, while the expansion of Eq. (10) is given by $\mu_{\text{GEA}} = 10/81$. This means that B86R does not have full alignment of the inner functional and the actual exchange-energy terms, something that CX maintains up to $s = 2$–3 by systematically relying on diagrammatic MBPT while assuming screened interaction lines in the diagrammatic interpretation [7,43,103]. However, we do find that the use of $\mu_{\text{GEA}} = 10/81$ and $\kappa < 1$ in Eq. (10) brings the B86R [56] exchange-enhancement values $F_X(2 < s < 10)$ closer to PBEsol exchange [51], without giving up the asymptotic $F_X(s) \sim s^{2/5}$ behavior that is also necessary [64]. We observe that PBEsol reflects a more modern approach to set exchange by enforcing XC-hole conservation [50,51,128] than the rPW86 [64,110], i.e., the large-s part of the CX exchange-energy design.

In summary, switching between CX-AHCX and B86R-AHBR means using different assumptions when setting the exchange impact on both the plasmon modeling [5,7,8] and on the actual XC balance. However, the switching is still done while staying within the same framework of MBPT analysis [7,9,43,46,50,51,56,101,103,127,149]. There are arguments for and against CX-AHCX and B86R-AHBR (just as there are for PBE and PBEsol in the GGA framework). Here we employ broad testing to assert which priority brings the greater benefits within the present range of vdW-DF design ideas.

Since AHBR is intended as a key part of our performance-contrast strategy, we must also secure and validate a general-purpose capability in this new nonempirical RSH vdW-DF. Here we benefit from past investments: The logic of the unscreened-hybrid "vdW-DF + 0" class [14,15] (that generalizes PBE0 [151,152]) leads, for example, to the formulation of the B86R-based DF2-BR0. We included a code option for this in the QUANTUM ESPRESSO (QE) code suite [153–155], while releasing the CX-based hybrid CX0 and CX0P, and we now report a full GMTKN55 assessment for DF2-BR0; see, for example, Figs. S1 and S2 and Tables SII–SX of the Supplemental Material [62]. We discover that there are very few outliers in the DF2-BR0 benchmark results [156] and that the performance gain of DF2-BR0 is particularly strong for the important transition-state problems. The fact that DF2-BR0 delivers well-balanced progress across general types of molecular problems is an additional strong motivation to complete and launch the screened-hybrid AHBR here.

D. Analytical-hole design of AHBR

The bottom panel of Fig. 2 compares the key exponent form $\mathcal{H}(s)$ that defines the long-separation shape of the exchange hole that is assumed to be of a modified Gaussian type [17,91,128,157]. In short, taking inspiration

from the exchange-hole form $n_x^{\text{LDA}}(\mathbf{r}; \mathbf{r}')$ that is known from LDA [48,49,108,157], one expects an exponential suppression,

$$n_x(\mathbf{r}; \mathbf{r}') \propto \exp\left[-\mathcal{H}(s(\mathbf{r}))(sy)^2\right], \quad (11)$$

where $y = k_F(\mathbf{r})|\mathbf{r} - \mathbf{r}'|$, and where the Gaussian suppression $\mathcal{H}(s)$ depends on the local value of the scaled density gradient $s(\mathbf{r})$ [128]. The ideas of the analytical exchange-hole modeling, as well as the logic and details of Eq. (11), are presented and discussed in Refs. [17,91,93,157].

The details of this Gaussian-suppression factor $\mathcal{H}(s)$ must be asserted to complete this AH model of a given XC functional. Technical details for vdW-DFs are discussed in Ref. [17]. The $\mathcal{H}(s)$ variation is given by a rational function [91] with parameters fitted subject to constraints so as to accurately describe, for example, the B86R-exchange behavior without introducing any spurious variation (that cannot be ascribed any physical meaning) [17,91,93,157]. The procedure for setting the parameters of $\mathcal{H}$ used previously to discuss and understand the PBE, PBEsol, CX, and AHCX exchange is repeated here for B86R. Table XI of the Supplemental Material SM reports $\mathcal{H}(s)$ parametrizations that underpin the now extended range of RSHs, including AHBR (that is based on understanding B86R exchange).

Figure 3 contrasts the dependence of the exchange hole on the local-electron-density environment for PBE, PBEsol, and B86R exchange. The panels show spatial variations of the exchange holes that result in the AH exchange modeling at a set of increasing values for the scaled density gradient s. The exchange hole n_x (of a given XC functional) is represented by its so-called dimensionless form $J(s(\mathbf{r}); \mathbf{r}, \mathbf{r}')$ defined by

$$n_x(\mathbf{r}, \mathbf{r}') = n(\mathbf{r}) \times J(s(\mathbf{r}); \mathbf{r}' - \mathbf{r}). \quad (12)$$

In the GGA-exchange model framework that we work with [17,91,93,128], the density suppression (by exchange effect) induced at position $\mathbf{r}'$ by an electron at $\mathbf{r}$ can be completely expressed in terms of a locally scaled distance $y = k_F(\mathbf{r})|\mathbf{r}' - \mathbf{r}|$ defined by the Fermi wave vector k_F [17]. As indicated in Eq. (12), the shape of J depends on the local value of the scaled density gradient $s(\mathbf{r})$. However, the entire $J(s, y)$ variation is set by finding parametrizations of the Gaussian-damping functions $\mathcal{H}(s)$ discussed above and plotted in the lower panels of Fig. 2. Thus, by tracking the shape of $J(s, y)$, the panels of Fig. 3, we summarize the full details of the exchange modeling [17]. The actual exchange-hole modeling (for PBE, PBEsol, and B86R, respectively) at any given position $\mathbf{r}$ is revealed by simply inserting the relevant local values for $s(\mathbf{r})$ and $k_F(\mathbf{r})$.

The right panel of Fig. 3 represents our new AH modeling for exchange effects in B86R. It is fully summarized in the J^{B86R} variation that is, in turn, sufficient to both recoup the B86R-exchange term $E_x^{\text{B86R}}(s)$ and set
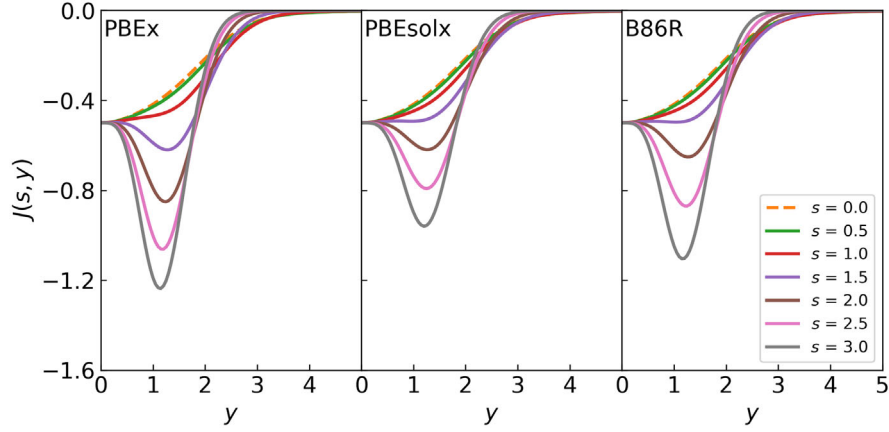
FIG. 3. Radial variation in the scaled exchange hole $J(s, y = k_F(\mathbf{r})|\mathbf{r} - \mathbf{r}'|) = n_x(\mathbf{r}, \mathbf{r}')/n(\mathbf{r})$ for PBE, PBEsol, and B86R, all as described in an AH model parametrization [17,91]. The shapes of these holes define the exchange components of PBE [50], PBEsol [51], and B86R, respectively. Using the latter exchange-hole model, we define the here-released RSH AHBR following the design steps that we recently documented in crafting AHCX [17].

AHBR below, adapting Refs. [17,91]. We find that, initially (at small-s values,), the B86R-exchange hole follows the PBEsol-exchange nature but does gradually roll over to a more PBE-exchange-type behavior. It also eventually approaches a CX-like behavior at large-s values where it respects the lessons of the analysis in Ref. [64]. Interestingly, the B86R exchange does, for $s \lesssim 3$, perform better than (CX and) PBE exchange in terms of avoiding the formation of deep exchange holes: The modeling of the B86R-exchange hole means that the suppression remains smaller than the local value of the electron density [50,51,128] (at $s \lesssim 3$).

We compare this AH analysis for the B86R-exchange-hole variation also with that for CX and AHCX [17], using the lower panel of Figs. 2 and 1 of Ref. [17]. First, it is clear that setting the exchange enhancement by μ_{GEA} brings the B86R closer to PBEsol exchange than the CX exchange design. Since the B86R exchange is still constrained by the input from Ref. [64], the large-s behavior rolls over toward that of CX. Moreover, being an intermediate of the PBEsol and of the CX exchange-hole modeling (Fig. 1 of Ref. [17]) the B86R has an mid-s-range behavior (around $s \approx 3$–4) that is close to the PBE hole form. This is again a more trusted behavior than that for rPW86 (that enters in CX).

From the AH analysis of B86R, Figs. 2 and 3, we complete the RSH nonlocal-correlation functional AHBR, following the same steps as previously described for AHCX [17]. The key observation is that our knowledge of the J^{B86R} variation allows us project out the short-range (SR) exchange-energy component $E_x^{\mathrm{B86R,SR}}[n; \gamma]$ from the exchange term E_x^{B86R} of B86R. The projection $E_x^{\mathrm{B86R,SR}}[n; \gamma]$ is again a density functional. As indicated, however, it also depends on the inverse length scale γ that we assume in the RSH design [17,93,94] for the screening in the Fock-exchange term [91,158]

$$E_{\mathrm{FX}}^{\mathrm{SR}}(\gamma) = \frac{1}{2} \int_{\mathbf{r}} \int_{\mathbf{r}'} \frac{n(\mathbf{r}) n_x^{\mathrm{Fo}}(\mathbf{r}'; \mathbf{r})}{|\mathbf{r} - \mathbf{r}'|} \mathrm{erfc}(\gamma|\mathbf{r}' - \mathbf{r}|), \quad (13)$$

where "erfc" denotes the error-function complement. The overall RSH vdW-DF form is [17,93,94]

$$E_{\mathrm{XC}}^{\mathrm{AHBR}}[n] = E_{\mathrm{XC}}^{\mathrm{B86R}}[n] + \alpha(E_{\mathrm{FX}}^{\mathrm{SR}}(\gamma) - E_x^{\mathrm{B86R,SR}}[n; \gamma]), \quad (14)$$

where α denotes the extent that we mix in the screened-Fock-exchange energy $E_{\mathrm{FX}}^{\mathrm{SR}}(\gamma)$.

A robust and computationally efficient determination of $E_x^{\mathrm{SR,B86R}}[n; \gamma]$ is a key benefit of working with the AH modeling [17,91]. To complete the RSH vdW-DF construction, Eq. (14), we need $E_x^{\mathrm{SR,B86R}}[n; \gamma]$. It is given in analogy to Eq. (9) but set by a modified exchange-enhancement factor $F_x^{\mathrm{SR}}(k_F(\mathbf{r}), s(\mathbf{r}))$. Thanks to the AH modeling of the B86R-exchange energy, above, we can complete an analytical evaluation of the formal expression

$$F_x^{\mathrm{B86R,SR}}(k_F, s) = -\frac{8}{9} \int_0^\infty y J^{\mathrm{B86R}}(s, y) \mathrm{erfc}(\gamma y/k_F) dy. \tag{15}$$

In fact, we get all the exchange details of the new AHBR from the corresponding AHCX details, Ref. [17], by simply switching from the CX- to the B86R-specific parametrization of the AH modeling; see Supplemental Material Table SXI [62].

Both RSH vdW-DFs, the new AHBR and the AHCX, can be used when screening of the Fock exchange is essential, for example, for descriptions of adsorption at metal and high-dielectric-constant surfaces [17,146,159].

The AHBR is deliberately kept free of fitted parameters. The extent and nature of the screened-Fock-exchange

inclusion could be adjusted but should then be given by physical inputs. Implementation of a formal thermodynamics criterion, in effect that the functional exhibits a piecewise linearity with the addition of a fractional electron [160–162], can set the value of the inverse screening length γ [158,163–165]. Similarly, the extent of Fock-exchange mixing α can be set by a coupling-constant analysis [15,42,130] or by demanding that the resulting dielectric constant is consistent with that implied in the Coulomb range separation [166–170]. In this AHBR launching work, we illustrate and contrast only generic RSH vdW-DF usage (that is, at fixed, HSE-standard values for α and γ).

III. RESULTS AND DISCUSSION

The DFT result data are obtained using our in-house version of the QE code suite. This code also has generic subroutines for calling RSH vdW-DFs [17] (already released to QE 7.0), and it benefits from the adaptively compressed exchange evaluation of Fock exchange [17,155,171]. Appendixes A and B provide an overview of the computational details that we use in general demonstrations and for the GMTKN55 assessment work, partly summarized in Fig. 1 already.

The CX and hence AHCX emphasis on screened LV exchange [46,54,103] means that they are naturally set up for accuracy in metal systems [43,120,121,172] and, we expect, broadly for bulk and many surface problems, including adsorption [17,18]. The new RSH vdW-DF has an advantage in being a general-purpose choice for molecular properties; see Fig. 1. Here we assert and discuss whether the new AHBR will remain an option also for bulk and adsorption, and whether it also works in a biochemistry and green-technology context. Our full GMTKN55 assessment (see Supplemental Material [62]) is part the AHBR documentation, and we extract a number of observations also from that mapping.

We note that the move to hybrids, including the RSH vdW-DFs [17], can help in counteracting excessive charge transfer and hence some density-driven errors [89,90]. This is true in the raw, fixed-parameters form presented above and because the AHCX and AHBR come with an option for γ tuning so as to also impose the thermodynamics (fractional-electron) constraint on the designs [160,165]. We expect that such tuned-AHBR usage will help further on controlling (density-driven) errors. However, we do not use that potential to gain additional XC-functional consistency in this first assessment.

A. Bulk-structure performance

Figure 4 documents a robust bulk-system performance of the new RSH AHBR. More broadly, Fig. 4 contrasts the performance for bulk of a new, second tool chain (comprising AHBR-B86R) with that of the first (AHCX-CX) [18] (and of DF2-AH). We do not report data for the
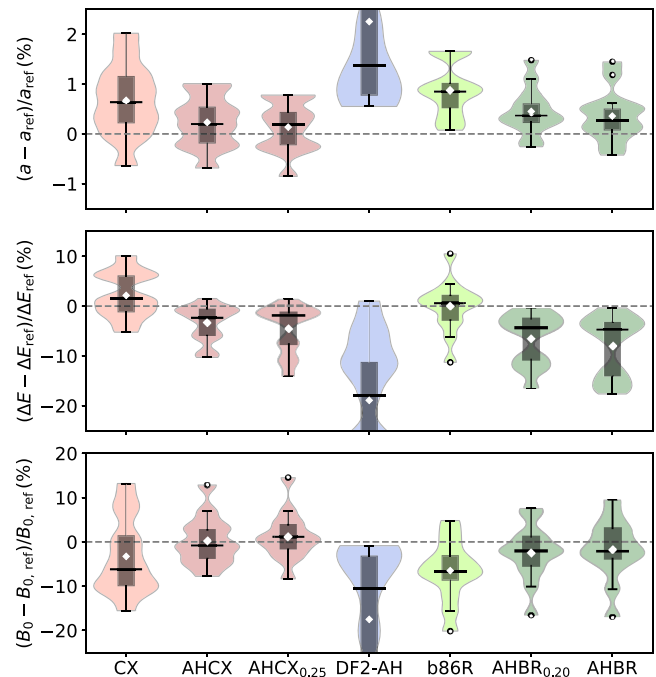

FIG. 4. Bulk-system performance as asserted in percentage deviations for the CX-AHCX and B86R-AHBR descriptions of lattice constants a, bulk cohesive energies E_{coh}, and bulk moduli B_0. We also show the impact of setting the Fock-exchange mixing. The default AHCX and AHBR mixing value is set at 0.20 and 0.25, respectively, while a subscript identifies an adjustment. For completeness, we furthermore include a performance assessment for DF2-AH, the RSH form of vdW-DF2 that is implicitly defined by analysis in Ref. [17]. We compare our results (listed in the Supplemental Material [62]) computed in the Born-Oppenheimer approximation, with experimental values (back-corrected for vibrational effects) [55]. The violin plots summarize result-statistics data for 13 solids (five transition metals, one simple metal, four semiconductors, and three ionic insulators), with the CX and AHCX results repeated from Ref. [17]. The set of horizontal bars (of diamonds) reflects the mean (median) deviation in the distributions, while the boxes identify the so-called interquartile range; see text. Outliers (identified in the text) are shown by open circles.

unscreened-hybrid components (DF2-BR0, CX0, CX0P) as we also consider metals [17].

The violin plots summarize the deviations in percentage of computed results for lattice constants a, cohesive energies E_{coh}, and bulk moduli B_0 from back-corrected experimental values for five transition metals (Cu, Ag, Au, Pt, and Rh), one simple metal (Al), four semiconductors (Si, C, SiC, and GaAs), and three ionic insulators (LiF, MgO, and NaCl) as in Ref. [17]. Tables SXIII–SXV of the Supplemental Material [62] present a more complete quantitative presentation contrasting the values computed in the two tool chains with the experimental values (that are back-corrected for vibrational effects) and with those we obtain for the RSH DF2-AH [17]. The subscript on one AHBR-data (and on one AHCX-data) label identifies the

TABLE I.   Comparison of vdW-DF performance on Pt- and noble-metal structure and elastic response: Lattice constants a (in Å), cohesive energies E_{coh} (in eV), and bulk moduli B_0 (in GPa). The Supplemental Material [62] gives full listings for our computed a, E_{coh}, and B_0 results for these transition metals and nine other materials. Experimental values back-corrected for vibrational effects (as indicated by an asterisk) are taken from Ref. [55].

	CX	AHCX	AHCX$_{0.25}$	B86R	AHBR$_{0.20}$	AHBR	Experiment*
Cu a	3.576	3.587	3.592	3.602	3.613	3.617	3.599
E_{coh}	3.781	3.348	3.264	3.582	3.160	3.064	3.513
B_0	163	148	146	151	141	136	144
Ag a	4.065	4.078	4.082	4.104	4.115	4.118	4.070
E_{coh}	2.955	2.774	2.737	2.779	2.592	2.549	2.964
B_0	115	105	104	102	95	95	106
Au a	4.101	4.098	4.097	4.134	4.127	4.126	4.067
E_{coh}	3.634	3.440	3.398	3.402	3.205	3.158	3.835
B_0	171	168	167	153	152	151	182
Pt a	3.929	3.910	3.906	3.952	3.929	3.925	3.917
E_{coh}	6.226	5.524	5.259	5.999	5.131	4.930	5.866
B_0	284	298	298	264	278	279	286

extent of Fock-exchange mixing. A corresponding specification is suppressed for "AHBR = AHBR$_{0.25}$" ("AHCX = AHCX$_{0.20}$") since this mixing reflects a recommended default, as we explain in the following subsection.

To contrast functional performance on bulk, we compare the position of the mean (median) deviation shown by a central bar (diamond) and the so-called interquartile range shown as a bar. This bar reflects the difference of positions for the first and third quartile of the performance distribution (for each functional). We also consider the presence or absence of outliers (open circles), by which we mean a performance that lies beyond markers (whiskers) that identify 1.5 times the interquartile range. Lattice-constant outliers are Au (Au and Ag) for AHBR$_{0.20}$ (AHBR) while cohesive-energy outliers are Au and Rh for B86R. There are more outliers for the bulk modulus: Rh for AHCX/AHCX$_{0.25}$, GaAs for B86R, and Au for AHBR and AHBR$_{0.20}$.

Figure 4 shows that there is a systematic AHBR improvement for lattice constants and bulk moduli compared to B86R, at both 0.20 and 0.25 Fock-exchange mixings. However, the B86R is more accurate than AHBR for predictions of the bulk cohesive energies.

Figure 4 also shows that the RSH AHCX is overall a better performer for bulk than AHBR$_{0.20/0.25}$. This is consistent with findings that CX has a small bulk-performance edge over B86R [17,55,172]. This observation holds, for example, for the lattice constant. However, AHBR is accurate on structure and hence useful also for substrate descriptions in heterogeneous systems. For example, the lattice-constant accuracy on noble metal and Pt metals remains within 0.5% deviations relative to (back-corrected) experimental values; see Table I.

As an interesting aside, we document that RSH DF2-AH (implicitly defined in Ref. [17]) is not well suited for bulk-system use. This is not surprising since there are real issues with using vdW-DF2 for bulk systems [60]. Tables SXIII–SXV of the Supplemental Material [62] show that there are large deviations between DF2-AH (and vdW-DF2) predictions and back-corrected experimental values for all of the investigated bulk properties. In the violin plot Fig. 4 we do not even depict the full extent of the interquartile range which for DF2-AH is set by first- and third-quartile relative deviations (0.78% and 3.5% for a, 11% and 29% for E_{coh} and −3% and −34% for B_0). Unlike AHBR, the DF2-AH is simply not a reliable option for bulk and hence for substrates in adsorption studies.

We ascribe the absence of vdW-DF2 and DF2-AH robustness (for descriptions across general molecular properties and bulk) to the fact that their designs depart from some of the ideas that emerged in the electron-gas tradition [7,12,43,46,47,51,101,106,109,110,128]. Use of diagrammatic-MBPT input, as summarized in Refs. [54,101,103], are prioritized in the design of PBEsol (unscreened) exchange [51] and in CX, with its emphasis on LV-screened exchange [7,10,103]. However, the design of (r)PW86 [64,110] that defines the vdW-DF2 and DF2-AH exchange, does not prioritize this MBPT input to the same extent.

Finally, Fig. 4 shows that the AHBR and AHCX bulk-structure characterizations are relatively insensitive to the choice of the Fock-exchange mixing. The AHCX design is set with a default 0.20 Fock-exchange mixing [17], but the overall bulk performance does improve slightly by going from AHCX = AHCX$_{0.20}$ to AHCX$_{0.25}$.

B. Binding in layered matter

We assess the RSH vdW-DF performance on layered systems using diffusion Monte Carlo (DMC) results [173–177] as reference data. We also discuss random-phase-approximation (RPA) literature results [178–180] and recent measurements of the cleavage energy in graphite

TABLE II. Comparison of vdW-DF performance on layered materials: Layer-binding E_{bind} (in meV/atom) and optimal layer separation d_{opt} (in Å) for graphite (sp^2-hybridized carbon) as well as graphene and α-graphyne bilayers (with sp-sp^2-hybridized carbon), hexagonal boron nitride (hBN) and phosphorus; see DMC Refs. [173–177,183] for summaries of in-plane atomic configurations. Stacking labels AA and AB (Ab) identify the geometries with carbon layers in full alignment and displaced one third (one ninth) of the sum of in-plane lattice constants, respectively. Stacking label AA' (for hBN) identifies in-plane alignment of boron atoms in one layer with nitrogen atoms in the other layer. For graphite, we also compare computed C_{33} values (in GPa) with an experimental result for a high-quality monocrystalline system with a large characteristic domain size 8.3 μm.

	Stacking	Benchmark	vdW-DF	CX	AHCX	vdW-DF2	B86R	AHBR$_{0.20}$	AHBR	RPA	DMC/Experiment
Graphite	AB-crystal	E_{bind}	55	67	72	54	62	63	64	48[a]/62[b]	60 ± 5[c]
		d_{opt}	3.57	3.26	3.27	3.51	3.30	3.31	3.31	3.34[a]/3.34[b]	3.43 ± 0.04[d]
		C_{33}	27.3	40.3	43.2	35.7	40.6	42.3	42.6	36[a]/38[e]	48.4 ± 5.3[e]
Graphite	AA-crystal	E_{bind}	50	54	52	47	49	44	43	⋯	36 ± 1[f]
		d_{opt}	3.73	3.55	3.55	3.67	3.54	3.56	3.57	⋯	3.63[f]
Graphene	AB-bilayer	E_{bind}	25	30	33	25	28	⋯	29	46[g]	18 ± 1[h]
		d_{opt}	3.61	3.29	3.29	3.53	3.33	⋯	3.33	3.39[g]	3.384[h]
Graphene	AA-bilayer	E_{bind}	22	24	26	21	22	⋯	23	⋯	12 ± 1[h]
		d_{opt}	3.76	3.58	3.57	3.69	3.57	⋯	3.58	⋯	3.495[h]
α-Graphyne	AB-bilayer	E_{bind}	20	20	23	18	17	⋯	18	⋯	23[I]
		d_{opt}	3.47	3.30	3.26	3.36	3.26	⋯	3.25	⋯	3.24[I]
α-Graphyne	Ab-bilayer	E_{bind}	19	19	21	18	16	⋯	17	⋯	22[I]
		d_{opt}	3.65	3.49	3.43	3.52	3.42	⋯	3.41	⋯	3.43[I]
hBN	AA'-bilayer	E_{bind}	24	29	32	24	26	⋯	28	19[g]	20(18)[j]
		d_{opt}	3.58	3.26	3.24	3.51	3.31	⋯	3.28	3.34[g]	3.25/3.50[j]
Phosphorus	AB-crystal	E_{bind}	79	127	124	83	117	⋯	112	⋯	81 ± 6[k]
		d_{opt}	5.69	5.19	5.26	5.67	5.27	⋯	5.33	⋯	5.2[k]

[a]Reference [178].
[b]Reference [179].
[c]Reference [173]; we report the raw DMC E_{bind} value (omitting an estimate for vibrational effects) for a relevant comparison.
[d]Reference [173]; the authors warn that (in-plane-size) convergence at large layer separations is not sufficient to accurately fit d_{opt}.
[e]Reference [184].
[f]Reference [174].
[g]Reference [180].
[h]Reference [183].
[i]Reference [175].
[j]Reference [176]; E_{bind} value without correction for infinite-layer extension is presented in parentheses. No fit for d_{opt} given.
[k]Reference [177]; the d_{opt} is extracted from Fig. 1 of that reference.

[181,182]. The graphite DMC study [173] came with both a raw DMC result and with an estimate for the expected correction (4 meV/atom) for vibrational effects in graphite. Our computed results (as well as the RPA literature results) are obtained in the Born-Oppenheimer approximation and should be compared with the raw DMC values listed in Table II.

For our RSH and nonhybrid-vdW-DF characterizations, we use a two-step approach, seeking to compare all functionals at a fixed in-plane structure that is close to experiments. First, we determine the in-plane lattice constants using a set of CX calculations (as CX is strong on structure [18,43] and hence has in-plane lattice constants that are close to experiment and thus to the values used in the set of DMC studies). This is generally done by variable-cell calculations. For the phosphorus crystal, the in-plane a_1 lattice constant is soft [177] (but the other in-plane lattice constant a_2 is still set by covalent bonds). There, we keep

a_1 fixed at the experimental (bulk) value (4.374 Å) while we use CX calculations to determine a_2. Further computational details are described in Appendix A.

Second, at fixed in-plane lattice vectors, we compute the total unit-cell energy $E(d)$ as a function of the layer separation d. For the RSH and regular vdW-DFs, we thus determine the optimal separation value d_{opt} and the asymptotic system value E_{asymp} (taken as the system energy at $d = 20$ Å). We extract the layer-binding energy

$$E_{bind} = [E(d_{opt}) - E_{asymp}]/N, \qquad (16)$$

where N denotes the number of atoms in the unit cell.

We note that the typical DMC binding-energy definition, Eq. (16), differs from the binding-energy definition (meV per layer atom) that is used for the discussion of early bilayer vdW-DF studies [4,20,28]. This has led to

confusion in vdW-DF presentations, for example, in Ref. [183]. We include new vdW-DF1 and vdW-DF2 characterization, now using the definition Eq. (16) for comparisons.

Table II reports our comparison of CX, AHCX and B86R, AHBR performance relative to the DMC reference data. In graphite, the CX and AHCX functionals give E_{bind} results that are larger than the DMC reference value, even allowing for error bars reported in Ref. [173]. However, the B86R and AHBR results for E_{bind} at 62–64 meV/atom are in excellent agreement with the relevant (that is, the raw) DMC reference value of 60 ± 5 meV/atom for the regular (AB-stacked) graphite crystal [173].

We observe that the B86R and AHBR results for the optimal layer separation at $d_{opt} = 3.30$–3.31 Å are smaller than the reported DMC value of 3.43 ± 0.04 Å and more in line with the experimental characterization [185] at $d_{opt} = 3.35$ Å. The graphite-AB DMC study has a lower convergence (with regard to in-plane extension) results for large layer separation, and the authors warn that it impacts the d_{opt} fit [173].

At the same time, there are good reasons to trust the graphite-AB DMC result of Ref. [173] for E_{bind}. The trust comes from recent high-precision measurements of the graphite cleavage energy giving binding-energy results of 54 and 55 meV/atom [181,182]. Including the estimate of a 4-meV/atom vibrational correction, there is full alignment with the graphite-AB DMC $E_{bind} = 60 \pm 5$ meV/atom result [173]. In turn, given the trust in the DMC result, we conclude that AHBR is highly accurate for graphite-AB binding; see Table II. In fact, for the regular graphite crystal, CX, B86R, and AHBR provide an E_{bind} description that is closer to DMC than one of the RPA results (at $E_{bind}^{RPA} = 48$ mev/atom) [178]. A second RPA study [179] (at $E_{bind}^{RPA} = 62$ mev/atom) is closer to the DMC result and fully agrees with our B86R and AHBR descriptions. However, the authors of that second RPA study warn that there can be an impact of RPA convergence [179].

Table II furthermore includes a comparison of the vdW-DF results for the C_{33} elastic constant, and we contrast those with recent ultrasound measurements on high-quality monocrystalline graphite samples with domain sizes increasing from 1.3 to 8.3 μm [184]. For the sample with a 1.3-μm domain size, the measured C_{33} value 40.1 ± 0.9 is in agreement with experiments on highly oriented graphite in the 36.5–38.7 GPa range [186,187], which also agrees with RPA studies [178,184]. However, for the large-domain sample, the measured C_{33} value increases to 48.4 ± 5.3 GPa, suggesting that defects impact the elastic behavior of highly-oriented-graphite samples. Again, we keep the in-plane lattice constant $a = 2.461$ Å fixed at the CX characterization of graphite for all functional studies and compute C_{33} from the double derivative of the $E_{bind}(d)$ variation. We find that our vdW-DF2 result aligns with the

RPA results and that our CX and B86R results agree with the recent measurements on the sample with a 1.3-μm domain size. We also find that the use of AHCX and AHBR leads to C_{33} predictions that best agree with the measurement on the high-quality sample with the 8.3-μm domain size.

Considering next the metastable graphite configuration with an AA stacking [174], we find that CX, AHCX, and B86R all make larger errors. However, we also find that AHBR, through its inclusion of a screened-Fock-exchange component, is able to correct much of the B86R overestimations. The AHBR result lands at about a 7–8 meV/atom deviation from the DMC reference data. The AA configuration may be seen as the barrier of an in-plane slip process of graphite (generalizing a picture that applies for polymers [188,189]). We therefore interpret the reasonable robustness of the AHBR characterization for graphite-AA as another example of success at characterizing transition states.

We also assess the performance for bilayer graphene in AB and AA stackings, and for the closely related hexagonal boron nitride (hBN) in AA' stacking against DMC studies [176,183]. These studies are again obtained for systems with a dense in-plane electron distribution; however, there is significantly less binding contribution in the unit cells. Part of the reason for that is evident by inspecting Fig. 8 of Ref. [43], noting that the dominant contribution in layered materials arises from the moderately low electron variation that exists between the layers: In a bilayer form, there is only half as many such regions as in the corresponding bulk. The layer binding is further reduced because bilayer systems lack the coupling to layers that are farther away, for example, as discussed in Refs. [190,191].

For the graphene bilayer system in both AB and AA stackings, we find that AHBR differs more (by about 11 meV/atom) from the DMC results [183]. The B86R and AHBR do perform better than CX and AHCX and are still significantly closer than the one RPA description that we find [180].

The AHBR description also differs from the DMC result for a hBN bilayer system. Here, it is instead a RPA result [180] that is close to the DMC value [176]. Our AHBR result differs 8 meV/atom from the DMC reference, in line with the status for graphite in AA stacking.

We note in passing that vdW-DF and vdW-DF2 are often closer to the DMC values for binding energies than B86R and AHBR (or CX and AHCX). However, Table II makes it clear that vdW-DF and vdW-DF2 systematically overestimate the layer-binding separation.

We also consider the AHCX and AHBR performance at α-graphyne bilayers, cases in which some of the carbon atoms in each plane are in the sp-hybridized form [175]. Here, interestingly we find that AHCX slightly outperforms the AHBR description on both structure and binding energies. However, the performance of AHBR as a new general-purpose RSH vdW-DF is still good, landing within

5 meV/atom of the DMC reference description. We also note that both AHCX and AHBR correctly predict the 1 meV/atom preference that separates the two competing motifs (AB and Ab stacking [175]) for these weakly bonded systems.

Finally, we assert the AHBR and AHCX performance for phosphorus bulk in the stable AB stacking. The DMC reference data [177] have E_{bind}, and we can extract an estimated value also for d_{opt}. We find again that vdW-DF2 and vdW-DF are closer than AHBR and AHCX for the layer-binding energy but not for structure. The AHBR (AHCX) estimate is 2% or 0.13 Å (1% or 0.06 Å) too large on d_{opt} while it overestimates E_{bind} by 31 meV/atom (43 meV/atom) relative to the DMC result 81 ± 6 meV/atom [177].

C. Robust molecular benchmarking and setting the Fock-exchange mixing in AHBR

Our use of the plane-wave code QE gives us the prerequisites for delivering a high-quality (in principle, complete-basis-set) assessment. We can secure a robust characterization as long as we also include all relevant electrons in the pseudopotentials (PPs) and compensate or control spurious electrostatic and vdW-type intercell interactions in our periodic-cell calculations. However, there are dramatic SIE effects or density-driven errors, and hence challenges with plane-wave benchmarking, in the study of negatively charged atoms and radicals [17,89]. The last electron will not necessarily remain bonded unless we work with small unit cells that artificially raise the vacuum floor in QE [17]. Because we seek to approach the complete-basis-set limit, we cannot provide a meaningful direct assessment of performance for the G21EA and WATER27 benchmark sets [192] of the GMTKN55 suite. Nevertheless, in Appendix B, we document that using a dielectric-environment extension [193] permits us to circumvent the SIE challenges and reliably complete general functional assessments.

Figure 1 summarizes the performance statistics for the top-performing regular vdW-DFs, including the CX and B86R, and both of the corresponding RSH vdW-DFs, the AHCX and the new AHBR. Details of this GMTKN55-based assessment are given in the Supplemental Material [62] Tables SII–SX. It covers almost all of the vdW-DFs that are coded in QE version 6.7 [194], the related revised VV10 [58,61], as well as the dispersion-corrected [95] revPBE + D3 [136] and HSE + D3 [93,94]. For comparison, we also list literature mean absolute deviation (MAD) results [69] for revPBE + D3, HSE + D3, SCAN + D3 [52,95], and B3LYP + D3, as obtained in orbital-based DFT.

The right panel focuses on the seven sets in the important GMTKN55 group 3 of molecular-barrier benchmarks reporting MADs relative to coupled-cluster quantum chemistry calculations [69] (in kcal/mol). The left panel presents the broader GMTKN55 performance overview

(characterized by weighted MAD values, i.e., the WTMAD1 measure introduced in Ref. [69]) and thus also covers the GMTKN55 groups 1 and 2 assessments for small- and large-molecule reactions and transformations, as well as groups 6, 4, and 5 of benchmarks covering total, inter- and intramolecular NOC interactions.

Figure 1 shows that the new RSH AHBR design is robust; i.e., it shows resilience toward density-driven errors [90]. This class of DFT problems affects barrier-height problems that in turn define the GMTKN55 benchmark group 3. Accuracy for transition states, and hence for predicting reaction rates, is considered a challenge even when the issue is considered in isolation [90,195]. It is exciting that AHBR provides balanced progress; i.e., it works just as well (maybe even better) for transition-state problems as it does for molecular-reaction energies.

For the benchmarking summarized in Fig. 1, and generally throughout the paper, we deliberately keep the RSH parameters fixed at the default HSE specification for the screening-length parameter [94], 0.106 inverse bohr, assuming also a fixed 0.25 (0.20) fraction for the mixing of short-range Fock exchange for AHBR (AHCX). These defaults are used throughout the paper, although we also sometimes illustrate the impact of switching between the two (standard, 0.20 and 0.25) choices for the extent of Fock-exchange mixing, as marked by subscripts (for example, $AHBR_{0.20}$).

In fact, we set this default recommendation for the AHBR Fock-exchange mixing, $AHBR = AHBR_{0.25}$, by directly relying on the broad GMTKN55 molecular benchmarking for this second-generation RSH vdW-DF. For individual problems and benchmarks, we could proceed to make a system-specific analysis to establish a plausible choice of the Fock-exchange mixing and screening, for example, as pursued in Refs. [158,163–170,196]. Here we observe that using $AHBR_{0.25}$ is systematically more accurate than $AHBR_{0.20}$ on molecular properties. We pick $\alpha = 0.25$ to give an impression of the accuracy that we can hope to get from AHBR usage.

We also note in passing that the suggested default AHCX 0.20 mixing came from a coupling-constant analysis of the contribution of CX correlation to the atomization energies [15,69]. The logic of that specification needs not hold for CX0P and AHCX when it comes to large systems (or bulk), let alone for AHBR. Looking at the full survey, in the Supplemental Material [62], we find that moving the AHCX to 0.25 Fock-exchange mixing gives a small performance gain both overall and for all but the NOC-interaction benchmark groups 4 and 5. The impact is in any case limited.

D. Navigating density-driven errors

It is natural to discuss the progress of AHBR as a molecule performer in terms of the resilience toward density-driven errors [89,90,92,143,195,197,198]. The promise of AHBR's

success in these key challenges is implied in Fig. 1, and here we provide details.

Any given XC approximation will cause an incorrect XC energy, and thus, DFT-total-energy evaluation, even if we have access to the exact density. However, there are additional challenges because the DFT calculations (based on the specific XC-functional approximation) can sometimes lead to an electron-density solution that is far from the exact density. This extra sensitivity causes performance outliers with a dramatically reduced accuracy of the system-specific DFT study [90]. Important examples are the generic-DFT failure to correctly confine the last electrons in some negatively charged ions [17,89], charge trapping in oxide defects [199] and color centers [200], molecular-reaction barrier heights [90], the CO-adsorption site-preference challenge on Pt(111) [92], and, we expect, adsorption-induced dissociation in the presence of large charge transfer [198].

The BH76 molecular-barrier-height benchmark has already been discussed as a key challenge for securing robustness, i.e., a driver for us to complete the design of the AHBR. It is also clear that the density-driven errors directly impact negatively charged ions and radicals [17,89], and hence the performance on, for example, the G21EA and the WATER27 sets in groups 2 and 4; see also Appendix B. Reference [90] additionally highlights the G2RC and RSE43 benchmark sets as being prone to density-driven errors.

For molecules, it is possible to use calculations of the Hartree-Fock (HF) electron-density solution to spot when we can expect density-driven errors [90,143]. For such cases, one would, in general, expect that moving to a hybrid is motivated, but there are also molecular cases where use of the unscreened-hybrid PBE0 [151,152] cannot by itself correct the issue [197].

The HF-based tests for density sensitivity [90] are carried out using our PPACF code contribution [15,42–44] to the QE DFT suite. For a given problem, we first pursue self-consistent HF calculations (for all reactants and products) to obtain the density variations denoted $n^{\text{HF}}(\mathbf{r})$ in that approximation. We also compute density variations denoted $n^{\text{LDA}}(\mathbf{r})$ using self-consistent LDA [49]. Next, we obtain so-called post-PBE energies [143] (for all reactants and products) denoted $E^{\text{HF-PBE}}$ and $E^{\text{LDA-PBE}}$ by evaluating the total DFT-PBE energies on the set of fixed $n^{\text{HF}}(\mathbf{r})$ and $n^{\text{LDA}}(\mathbf{r})$ density variations, respectively. In practice, this is done by manually changing the FUNCTIONAL entries to "PBE" in the QE-output xml files before starting PPACF for non-self-consistent total-energy evaluations. Finally, we compute process-energy differences denoted $\Delta E^{\text{HF-PBE}}_{\text{proc}}$ and $\Delta E^{\text{LDA-PBE}}_{\text{proc}}$ for the set of $E^{\text{HF-PBE}}$ and $E^{\text{LDA-PBE}}$ energies and evaluate the density-error-sensitivity measure [143]

$$\tilde{S}_{\text{proc}} = |\Delta E^{\text{HF-PBE}}_{\text{proc}} - \Delta E^{\text{LDA-PBE}}_{\text{proc}}|. \quad (17)$$

This measure reveals whether there are fundamental differences between the HF and KS orbitals and hence whether we can expect density errors to significantly affect any given (GGA or vdW-DF) DFT characterization [143]. For a benchmark set, one can also define an average value $\tilde{S}_{\text{av}}$ over case-specific $\tilde{S}_{\text{proc}}$ values [143], essentially adapting the ideas of benchmark MAD assessments. If $\tilde{S}_{\text{av}}$ ($\tilde{S}_{\text{proc}}$) is asserted as larger than 2 kcal/mol, then the benchmark set (process) should be considered as density sensitive [90,143].

Using this assessment procedure, we presently add documentation that the PX13 (barrier height) and the C60ISO (large-system isomerization) sets are also prone to density-driven errors, i.e., given by characteristic sensitive measures $\tilde{S}_{\text{av}} > 2$ kcal/mol. The present $\tilde{S}_{\text{av}}$-based mapping supplements the literature identification of pronounced sensitivities for BH76, G2RC, and RSE43 [90]. In the literature cases, the measures are comparable even to the PBE MAD values themselves. For C60ISO (and to some extent also for PX13), we find that the measure represents a significant fraction of the PBE MAD value.

Table III contrasts the PBE, CX, vdW-DF2, HSE + D3, AHCX, and AHBR performances, asserted as MAD values, on those density-sensitive benchmarks [90]. The table shows that the AHBR here performs at the same level or better than HSE-D3, and systematically better than AHCX. This latter finding is expected because we give arguments (in Sec. II) that the condition that exists for CX (to fully leverage its Lindhard-screening foundation discussed in Sec. II) might make the CX more susceptible to density-driven errors. The first observation is important for encouraging broad vdW-DF method testing: The AHBR has a good general-purpose capability for recognized challenges.

In fact, Table III suggests that the AHBR may also compete favorably with PBE-based density-corrected DFT [90,143] on density-sensitive problems. That approach is denoted DC(HF)-PBE or DC(HF)-PBE + D4 when supplemented with the Grimme-D4 dispersion correction [40]. The D4 inclusion is not proven relevant in these GMTKN55 benchmark cases (BH76, G2RC, and RSE43) [90]. The DF (HF)-PBE approach takes off from the above-discussed HF-PBE description; however, in DC(HF)-PBE, the HF-PBE result replaces only a self-consistent PBE result when the process-specific measure $\tilde{S}_{\text{proc}}$ is larger than 2 kcal/mol. We find that AHBR performs better than DC(HF)-PBE in all three cases, and it is, for example, more robust for both small-molecule reaction energies (RC21) and for transition states (as probed in the barrier-height benchmark BH76).

Table IV provides further documentation of the AHBR ability to navigate molecular DFT challenges. The table compares our assessments for the RSH vdW-DFs with regular functionals (revPBE + D3, CX, vdW-DF2, and B86R) and with HSE + D3. The selection to focus our additional discussion on these benchmark sets is based on two criteria: (1) the benchmark-specific MAD values are

TABLE III. Comparison of PBE, CX, vdW-DF2, HSE + D3, AHCX, and AHBR performance on benchmark sets that have a pronounced density sensitivity, as asserted by a Hartree-Fock (HF) sensitivity measure $\tilde{S}_{av} > 2$ kcal/mol [90]. We also list, where available, literature values for the performance of density-corrected PBE termed DC(HF)-PBE (using HF densities to improve the PBE description when the process or reaction is found sensitive [90,143]). For this density-corrected PBE [143,197], we list literature results for the performance with a Grimme-D4 dispersion correction [40]. The table section sorts the benchmark comparison according to their inclusion in GMTKN55 groups 3, 1, and 2, respectively. The density sensitivity of G21EA [89] is discussed in Appendix B. Benchmark results are represented in MAD values (in kcal/mol) asserted relative to the coupled-cluster results that define the GMTKN55 reference data.

	$\tilde{S}_{av}$	PBE	CX	vdW-DF2	DC(HF)-PBE/+D4	HSE + D3	AHCX	AHBR
BH76	8.0[a]	8.46	9.15	6.90	4.4[a]/4.7[a]	4.21	5.15	4.14
PX13	4.3	12.12	12.80	1.14	$\cdots$	7.38	7.30	4.57
G2RC	11.3[a]	5.85	6.77	9.43	4.3[a]/4.1[a]	6.48	4.71	3.30
G21EA	$\cdots$	3.07	2.80	9.66	$\cdots$	3.40	2.17	2.32
RSE43	3.7[a]	2.54	2.21	1.13	2.0[a]/1.9[a]	1.25	1.01	0.74
C60ISO	5.1	10.06	12.01	10.43	$\cdots$	2.51	3.99	2.72

[a]Reference [90].

large enough to allow a reliable interpretation in terms of XC-functional trends, and (2) the usage-oriented mapping of the density-sensitivity problems (see Ref. [197]) suggests that here we face interesting DFT challenges. That is, we primarily focus on the benchmark sets where a separate assessment [197] finds affirmative answers (listed in the second column) to the question of whether HF-PBE + D4 improves PBE + D4 (and we can again expect an impact of density-driven errors). However, we also direct attention to

performance surprises. For all cases, we simultaneously report the literature answer (third column) to whether the unscreened-hybrid PBE0 + D4 in self-consistent calculations makes for a further improvement over HF-PBE + D4; i.e., whether the use of a hybrid can be expected to resolve the underlying DFT issues.

We want the AHBR to succeed well in all such cases, as we want it to be general purpose. Note that we supplement the selection in the table with the BHPERI barrier-height

TABLE IV. Comparison of revPBE + D3, CX, vdW-DF2, HSE + D3, AHCX, and AHBR performance on benchmark sets that are density sensitive, here as asserted from comparing self-consistent PBE + D4 and HF-PBE + D4 performance measures. For key benchmark examples, the second column asks, "Is the MAD value for HF-PBE + D4 [namely, the key element of DC(HF)-PBE + D4] better than it is for regular (self-consistent) PBE + D4?" using a GMTKN55 survey of density-corrected PBE [197]. The answers are practical identifications of sensitivity. The third column uses those data [197] to answer the question, "Does PBE0 + D4 outperform HF-PBE + D4 for this benchmark set?" I.e., it assesses if an unscreened hybrid can itself be expected to correct for the density sensitivity. The first and bottom sections of the table contrast benchmark performances (listed as MAD values in kcal/mol) for GMTKN55 groups 1–3 and in the inter- and intramolecular NOC-interaction groups 4 and 5, respectively.

	Sensitive?[a]	PBE0 + D4?[a]	revPBE + D3	CX	vdW-DF2	B86R	HSE + D3	AHCX	AHBR
BH76	Yes	Unclear	7.38	9.15	6.90	9.22	4.21	5.15	4.14
PX13	Yes	Yes	9.29	12.80	1.14	11.36	7.38	7.30	4.57
BHPERI	No	Yes	5.74	7.20	3.08	6.08	2.83	4.05	1.84
W4-11	Yes	Yes	5.88	8.55	18.69	6.97	6.77	4.99	9.50
DC13	Yes	Unclear	9.38	7.88	24.21	7.26	8.24	8.35	6.18
SIE4x4	Yes	Yes	21.67	23.80	21.73	23.52	13.58	17.00	15.09
ISOL24	Yes	Yes	4.82	2.65	12.69	3.68	2.42	2.25	1.82
PNICO23	Yes	No	0.84	0.66	0.39	0.56	0.86	0.44	0.25
HAL59	Yes	No	0.82	0.94	0.69	1.00	0.64	0.63	0.58
WATER27	Yes	Unclear	2.63	2.88	1.75	5.10	5.73	2.71	2.52
Amino20x4	Yes	Yes	0.35	0.25	0.39	0.22	0.29	0.22	0.19
IDISP	$\cdots$	$\cdots$	3.25	2.27	7.89	2.69	2.96	1.61	1.50

[a]Reference [197].

set and with the IDISP set. In the case of the BHPERI set, the HF-DFT+D4 is not found to help but the PBE0 + D4 is, so something more than density-driven errors could be at play. We do not find any literature evidence for density sensitivity in the case of the IDISP set. However, we still include it in this discussion, for it is our experience that IDISP and WATER27 are the two NOC-interaction benchmark sets that primarily challenge the vdW-DFs; see Supplemental Material [62].

We find that the RSH vdW-DFs (like HSE + D3) almost always improve the description over comparable regular forms, comparing AHCX and AHBR MAD values with those for CX and B86R, respectively. For HSE + D3, the observation is inferred only: HSE + D3 should ideally be compared to PBE + D3, which we do not assert, but Ref. [69] does identify revPBE + D3 as being the best overall GGA + D3 performer. This trend of RSH strength is generally expected. However, atom descriptions are known to generally challenge hybrids, and we do find that the W4-11 set on atomization energies is the exception to this trend.

For the W4-11 set, we also find that AHCX performs better than AHBR. This is not surprising since the two RSH vdW-DFs are born with different default values of the Fock-exchange mixing. We note that picking instead the same mixing $\alpha = 0.2$ (a choice that we have previously justified for atomization-energy descriptions using the CX0P and hence AHCX [42]) significantly helps the $AHBR_{0.20}$ performance on W4-11; see Supplemental Material [62].

Table IV supports Fig. 1 in showing that AHBR performs better than the HSE + D3 overall also for this set of externally identified DFT challenges. The W4-11 is again an exception, but there are also many cases where the AHBR is the top performer for the sets that are flagged as density sensitive. The AHBR is also better on the BHPERI set even though the PBE-based gauge finds that simply going to the HF-PBE + D4 correction does not help in that class of problems. It is clear that the hybrid benefits for BHPERI is not confined to a selection of dispersion-corrected PBE0. We furthermore observe that Ref. [197] found dispersion-corrected PBE0 insufficient by itself to recoup or improve on a dispersion-corrected HF-PBE description for BH76, DC13, PNICO23, HAL59, and WATER27 sets. It is encouraging that, in contrast, the AHBR does provide accuracy gains over both B86R and HSE + D3 in these special cases.

Taken together, Tables III and IV also show that vdW-DF2 is able to navigate density-driven errors extremely well in some type of problems, but it is overall characterized by having highly uneven performance. The vdW-DF2 advantages seem to primarily manifest themselves in group 3 barrier-height problems, such as the BH76, PX13, and to a lesser extent, the BHPERI sets. It is also good for the WATER27 set as well as, in fact, for most NOC-interaction problems [17]. However, it is a weak performer

in the IDISP and ISOL24 challenges and the Supplemental Material [62] shows that the vdW-DF2 also has substantial limitations for many groups 1 and 2 sets on small- and large-molecule properties.

Some of us have recently documented [44] that a good vdW-DF1 and vdW-DF2 performance can sometimes arise because it has an XC balance that is better set up to handle the case of more diffusive interactions [44]. The CX is considerably more accurate than vdW-DF1 and DF2 for the simpler case of CO_2 adsorption in Mg-MOF-74, but the reverse is true for the more complex cases of CO_2 adsorption in diamine-appended Zn_2(dobpdc) [44]. We find it plausible that the vdW-DF1 and vdW-DF2 succeed (compared to other vdW-DFs) on the more complex m-2-m-Zn_2(dobpdc) system in part by minimizing density-driven errors, given the fact that they navigate such errors in, for example, the BH76 and PX13 sets, above. It is also possible that the vdW-DF1 and vdW-DF2 accuracy on m-2-m-Zn_2(dobpdc) energies is simply fortuitous, as these functionals worsen the description of structure, for example, in m-2-m-Zn_2(dobpdc) [44]. However, the relevance of using the rPW86 exchange in vdW-DF2 (that, like AHBR, uses a Schwinger-scaling argument to set the nonlocal correlation [8]) was asserted by documenting that rPW86 mimics a Fock-exchange description for intermolecular interactions [64]. Since vdW-DF2 does excel at many types of transition-state and NOC-interaction problems (see Supplemental Material [62], Tables SV–SVII), we find it wise to respect the lessons of vdW-DF2 progress. This is especially so now that AHBR offers us a chance to combine its nonlocal-correlation design with a screened-Fock-exchange form. We therefore include below an additional AHBR test asserting its performance for m-2-m-Zn_2(dobpdc).

E. Further lessons from small and large systems

Figure 5 summarizes the inter- and intramolecular NOC-interaction parts of our functional-performance comparison. The figure shows the benchmark groups that give different indications for a convenient AHCX and AHBR choice of default Fock-exchange mixing. For the vdW-DFs and rVV10 [58,61], as well as dispersion-corrected revPBE + D3 and HSE + D3, the group-averaged performance is represented in a scatter plot that relies on taking a raw, so-called TMAD, performance indicator [201] on NOC-interaction systems (from the GMTKN55 suite). This measure is defined by taking a simple average over the MAD values that we obtain for the individual benchmarks, as described in the Supplemental Material of Ref. [17]. We use the intermolecular (intramolecular) NOC TMAD value for group 4 (group 5) to set the abscissa (ordinate); Table SIV of the Supplemental Material [62] contains a listing of the TMAD values that are reported in the panels of Fig. 5 (as well as for those evaluated for the other GMTKN55 benchmark groups).
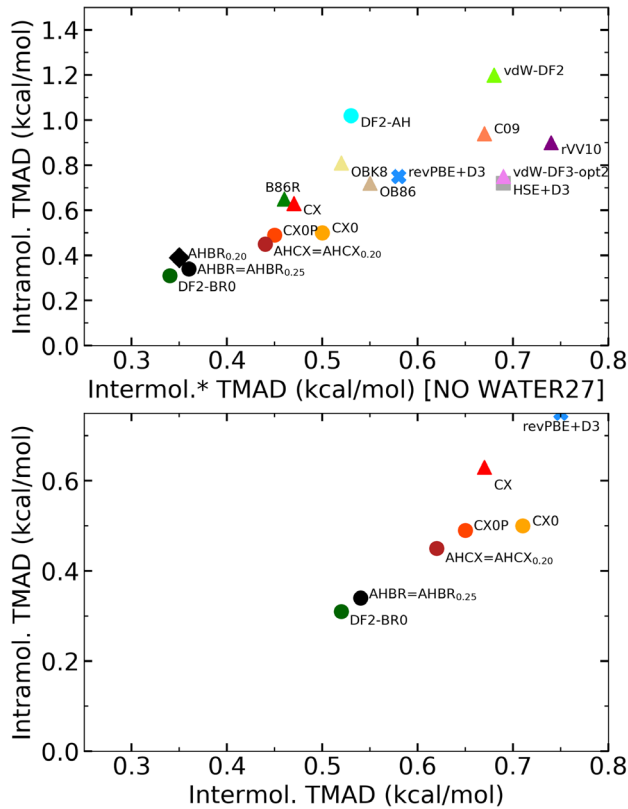
FIG. 5. Performance comparisons of vdW-DFs (as well as dispersion-corrected [95] revPBE and HSE) for NOC interactions. We report and correlate total MADs [17,201] (TMADs) formed as a simple average over benchmark MAD values of intermolecular and intramolecular NOC interactions. Table SIV of the Supplemental Material [62] shows a quantitative listing. The survey of RSH vdW-DF performance is tracked at two different choices of the Fock-exchange mixings (subscripts). The top panel relies on raw plane-wave-DFT results, as indicated by the asterisk. We must then omit the WATER27 benchmark set [17,89]. The bottom panel presents the corresponding survey as it results when we use an electrostatic-handling procedure (see Appendix B) to also assert the performance for the proton-transfer processes in the WATER27 set.

Figure 5 also highlights the key impact of excluding (top panel) or including (bottom panel) the impact of the WATER27 benchmark. This benchmark is often excluded in functional comparisons on vdW problems [17,201], because it contains the negatively charged small radical OH$^-$, and it is therefore not accessible in a simple benchmarking [17,18,89]. Like for the systems in the G21EA benchmark set, this radical has pronounced self-interaction errors [89] as well as convergence challenges that prompt us to pursue the more general plane-wave-benchmarking procedure defined in Appendix B. Insight into water in general and accuracy in WATER27 benchmarking are essential on science grounds and when pursuing systematic XC development.

We show that the correct inclusion of the WATER27 benchmark set (Appendix B and Fig. 5) has dramatic

impact on what we consider XC-functional promise for NOC interactions. The assessment map is clearly affected as we switch from the top to the bottom panel of Fig. 5. In fact, it is alone the consistent-exchange class (CX, CX0P and CX0, and AHCX), the unscreened DF2-BR0, and the new AHBR that remain good options for this challenge, at least as asserted by our plane-wave benchmarking of the GMTKN55 suite.

In a recent paper, we suggested that there is value in using the tool chain of closely related CX, CX0P, and AHCX designs for a systematic exploration of bulk materials [18]. Here we propose the use of AHBR for explorations on molecules and their adsorption. It is known that density-corrected DFT should not always be used [90]. For traditional hybrids (like HSE), there is an expectation that such a hybrid PBE will worsen the thermophysical description of solids, especially for magnetic elements and transition-metal adsorption [66,202–205]. The reason for exploring is that we want to know what limitations hold for the RSH vdW-DFs and for AHBR in particular. More broadly, we want to learn to assert, *a priori*, when one should use both nonlocal correlation and nonlocal exchange in combination and when the regular vdW-DF (CX or B86R) suffices. Interestingly, we find, here and in Refs. [17,18], that AHCX and AHBR improve descriptions of bulk structure and, at least, some adsorption problems (over the underlying regular versions, CX and B86R). For molecular properties, it is instead securing a balanced and robust progress that is the challenge for hybrid vdW-DFs.

In this light, it is interesting to note that the impact of including the WATER27 challenge on the first tool chain (comprising CX-CX0 and CX0P-AHCX) is, overall, smaller than that on the B86R design. The B86R itself is, in fact, moved out off the figure range for intermolecular-NOC assessment values. However, the corresponding B86R-based hybrids, DF2-BR0 and the new AHBR, remain exceptionally well suited to meet the full set of NOC challenges, at least as presently asserted. Also, looking at the quantitative measures in Table SIV of the Supplemental Material [62], we find that AHBR$_{0.20}$ appears to perform slightly better than AHBR$_{0.25}$ on intermolecular NOC interactions in the approximate assessment (top panel), but the actual status is different (bottom panel).

Overall, we see the robustness of CX, CX0P, and AHCX, and DF2-BR0 and AHBR as an indication of the value and usefulness as we seek to map for and understand outstanding DFT challenges [18,69]. For the NOC-interaction, small-molecular, and barrier cases, the AHBR is the more robust, error-resilient design; see Figs. 1 and 5.

Figure 6 considers the C60 isomerization problems using the reference data of the C60ISO benchmark set for an analysis of a large-system transformation (group 2) case. The C60ISO is a benchmark set where all regular vdW-DFs fail and where hybrids are needed; see Supplemental Material [62]. It is also a case where we document that
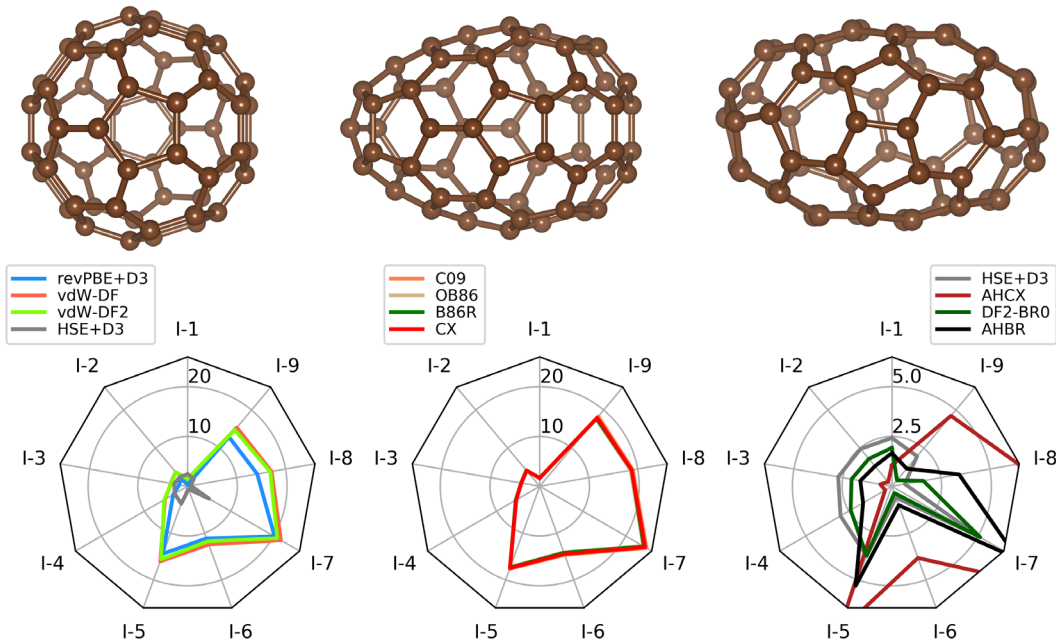
FIG. 6. Performance of original vdW-DF releases (left panel), recent regular vdW-DFs (middle panel), and hybrid vdW-DFs (right panel) on a set of C_{60} isomerization problems. The top left (right) panel shows the regular (highly distorted) configuration. The middle panel depicts one of the intermediate configurations in the transformation, as tracked in the C60ISO benchmark set [69]. The bottom left (middle) panel shows MAD values (in kcal/mol) characterizing the performance of the original vdW-DF releases (recent regular vdW-DFs) on describing energy differences between such configurations. The bottom right panel shows that the hybrid vdW-DFs are needed to substantially improve the description.

there are pronounced density-driven errors at play, and compare the C60ISO values that we compute for $\tilde{S}_{av}$ and PBE in Table III.

The top panels of Fig. 6 illustrate the nature of the C60ISO benchmark set in the large-system isomerization group 2 of the GMTKN55 suite. The benchmark set considers the energy differences among ten metastable forms of C_{60} of energy E_n. The top left panel shows the stable fullerene form ("$n = 1$") and, the top right panel shows the oblate form ("$n = 10$"). Between them are also states of increasing deformations (denoted "2" to "9"), and the GMTKN55 suite provides reference data for nine isomerization energy-difference problems denoted "In" (for $n = 1$ through $n = 9$). These C60ISO problems are specified by reference values for the set of differences $E_{n+1} - E_1$ ($n = 1$ through 9). The top middle panel shows the atomic geometry configuration for the frustrated structure "$n = 8$"; i.e., a form that determines isomerization problem "I7" and that is often hard to accurately describe.

The set of bottom panels provides a radar-plot comparison that reveals both vdW-DF limitations and vdW-DF promise. Specifically, the bottom left (middle) panel shows that vdW-DF1 and vdW-DF2 both fail (that recent releases and variants including CX and B86R offer no improvements). As the benchmark is prone to density-driven errors, Table III, it is no surprise that HSE + D3 provides a significantly improved description over regular vdW-DFs. As shown it the bottom left panel (note the change

in scale), the AHCX helps, but AHBR is needed to improve the description to the HSE-D3 level.

We interpret the nonhybrid-vdW-DF performance issues as arising because here we must describe stretched and frustrated binding. The fact that there are density-driven errors is not surprising, for this isomerization problem can also be seen as another transition-state case. In fact, the set of metastable C_{60} configurations can be seen as configurations that define some effective deformation paths taking us from configuration "1" to "10."

We can expect that the DF2-BR0 and AHBR are accurate also for the C60ISO set (as it is documented in the lower right panel). However, given the status for the (barrier-height) benchmark group 3 and given that this is a transition-state problem, it is perhaps surprising that the vdW-DF1 and vdW-DF2 are not acceptable performers here. It appears that there are more than one type of challenge in describing the transition states. We can certainly still learn from vdW-DF2 and vdW-DF1, but it is also clear that we need to cast a wider net to identify good development ideas. This can, as suggested here, be done by the use of the more robust AHBR.

F. Need for vdW-DF hybrids: Molecular examples

Transition-state problems stand out because they involve a comparison of energy terms that must simultaneously reflect several different types of binding, for example, relaxed and stretched or diffusive. Some of us have recently

characterized functional performance in the description of CO_2-MOF adsorption that happens in concert with a site-specific reaction and resulting CO_2 insertion in a diamine-appended MOF [44]. There, the vdW-DF1 and vdW-DF2 also have an accuracy edge, but it does not apply for CO_2 adsorption in the simpler Mg-MOF-74 system [44]. The transition-state problems can be seen as key drivers for XC development [90,195].

Figure 1 and Figs. S1–S2 of the Supplemental Material [62] provide a broad illustration that the vdW-DF tool bag must include the set of new hybrid vdW-DFs, i.e., DF2-BR0, AHCX, and AHBR. The set of recent regular vdW-DFs (including CX and B86R) do not remain uniformly accurate when tracked across the seven individual barrier-height benchmarks of GMTKN55; see Fig. 1 (right panel) and Supplemental Material [62]. Inspecting Supplemental Material [62] Tables SV–SX makes it clear that problems of a transition-state nature (such as we deem those of the C60ISO and MB16-43 sets), in general, challenge the nonhybrid vdW-DFs. Nevertheless, we find that the DF2-BR0 performance stands out in terms of both accuracy and cross-benchmark resilience even at transition-state problems. As we note in the Introduction, in turn, the DF2-BR0 resilience and transferability for molecular problems motivate the AHBR completion.

Meanwhile, the underlying benchmarking data (see Tables SII–SX of the Supplemental Material [62]) show that the vdW-DF2-ah hybrid [17] is not a reliable option for the study of broad molecular properties (just like it failed for bulk). Like the vdW-DF2, it has an acceptable performance for NOC-interaction and barrier-height problems. However, vdW-DF2 and vdW-DF2-ah have real shortcomings when the focus is instead moved to general properties of small- and large-molecule systems.

More broadly, the GMTKN55 survey suggests that we cannot hope for one gradient-corrected exchange form (as used in the present type of nonhybrid-vdW-DF designs) to always succeed. We see that the assessments of GMTKN55 performance show a spread in performance for all nonhybrid vdW-DFs among different classes of problems; see Supplemental Material [62]. The same is true, but to a significantly smaller extent, for the CX and B86R-based hybrids. There are many problems, and it is not trivial to secure a good XC balance in the present type of vdW-DF designs across all of such problems. Specifically, in the vdW-DFs, we add an attractive nonlocal-correlation term to the spurious LDA-exchange overbinding [63]. The nonlocal correlation contains more than pure dispersion effects, while it also goes beyond GGA correlation at shorter distances [43]. At the same time, in the nonhybrid vdW-DF we must rely on nothing but gradient-corrected exchange for stabilization in the presence of both LDA overbinding and the enhanced attraction of these nonlocal-correlation effects [4,44,64].

The fact that the strength of the vdW attraction may enhance in select situations [44] suggests an additional mapping role for vdW-DF hybrids. The plan is simply to use and contrast AHCX and AHBR for explorations, for example, in cases with diffusive interactions [44], when interactions compete [11], and when phase transformations compete [18,126,206]. In the latter case, the presence of an actual or incipient ferroelectric transformation will itself affect the magnitude of the dielectric constant. For example, while the unscreened-hybrid CX0P is highly accurate for $BaZrO_3$ [206], we need more to address $SrTiO_3$ [18]. Access to RSH vdW-DFs means that we better map the nature of specific challenges, correlate progress with design choices, and eventually implement new ideas in XC developments.

In Fig. 7, we identify a key set of molecular-type challenges that we think can be used to drive XC development, without going directly to more complex (but technologically relevant) cases. For example, an accurate description of some transition-state problems (benchmark sets I, II, IV, and V in the left panel) requires a unique XC balance that vdW-DF2 occasionally provides, yet vdW-DF2 often fails spectacularly, as seen in the Supplemental Material [62]. Reference [44] provides an adsorption case where vdW-DF2 also shines by delivering an exceptionally large repulsion by gradient-corrected exchange, but such a repulsion is not always needed [44]. It is therefore good to seek a simpler way to survey for XC issues, as in Fig. 7. Our proposal is based on the experience that we gain by plane-wave benchmarking across both the entire GMTKN55 and for CO_2 uptake in MOFs, for example, in Refs. [11,17,18,44,80,81]. We mostly echo, but also simplify, the logic that led to the definition of the full GMTKN55 suite [69]. In making this identification, we are assuming that we are working with a vdW-inclusive functional, like the vdW-DFs, so that the design is also capable of dealing with the groups 4 and 5 types of NOC-interaction problems.

Well-known challenges for any DFT are, of course, still found in the SIE4x4 set (on self-interaction errors in neutral and positively charged systems), the MB16-43 (mindless benchmarking) set, and the DC13 (difficult for DFT) set. To these sets we add the G21EA and WATER27 sets because these two sets suffer from pronounced SIE effects, and in the latter case will also significantly impact the performance of any given candidate on the group 4 problems. Additionally, we include the IDISP set as it is almost always the challenge that dominates in setting the performance of an XC functional on group 5 of intramolecular NOC interactions.

From the barrier-height class, we find that the performance varies prominently when inspecting the BHPERI, PX13, and WCPT18 sets. At least it is clear that these benchmarks allow the hybrid benefits to directly manifest themselves. Finally, we point to the above-discussed C60ISO set as a supplement to the focus on barrier-height problems: It clearly reflects both a transition-state nature,
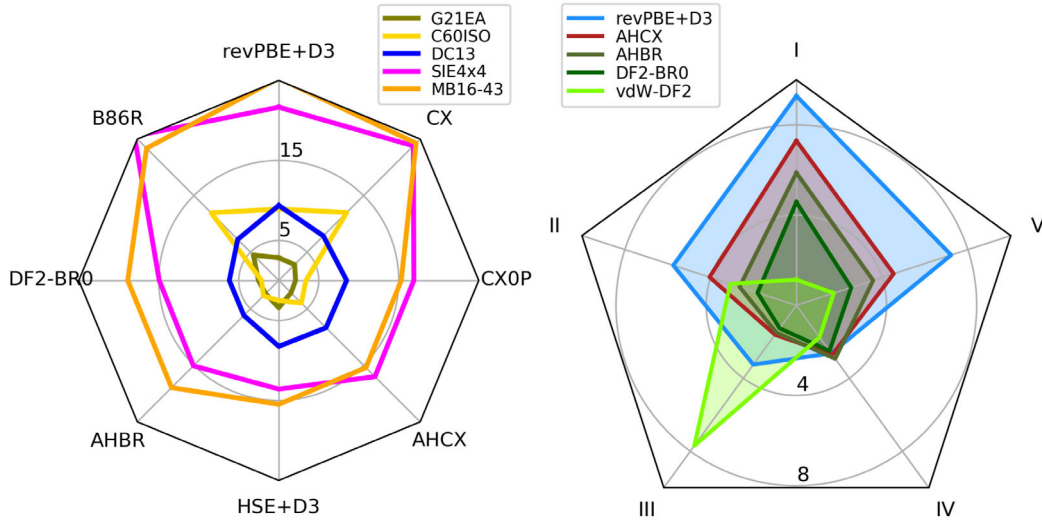
FIG. 7. Drivers for XC development in the GMTKN55 suite of benchmarks [69]. Performance of vdW-DF-based hybrids on traditional molecular challenges (identified in left panel) and on what we consider key transition-state challenges (right panel) in benchmark set PX13 (I), BHPERI (II), IDISP (III), WATER27 (IV), and WCPT18 (V). Self-interaction errors play an essential role not only in the SIE4x4 set but also in G21EA (WATER27) due to the presence of negative ions and radicals [89] requiring an electrostatic-environment approach for reliable assessments (see Appendix B). The traditional challenges include the so-called "difficult-for-DFT" (DC13) and "mindless benchmarking" (MB16-43) sets, as well as fullerene isomerization problems (collected in benchmark set C60ISO).

but it also points to an additional, yet-to-be-identified aspect. This is because the vdW-DF1 and vdW-DF2 barrier-height successes at the WCPT18 and PX13 benchmark sets do not port well to this C60ISO set.

Finally, Fig. 7 illustrates the usefulness of simplifying functional comparisons while focusing on where we can learn more. The figure compares the performance of the CX, CX0P, and AHCX functionals and the B86R, DF2-BR0, and AHBR functionals in two types of radar plots. The left panel makes the comparison based on G21EA as well as the sets where there are often massive deviations between the DFT results and reference data from quantum-chemistry calculations [69]. The right panel compares the selection of barrier problems and NOC-interaction problems. The overall impression is that the robustness of DF2-BR0 and AHBR is confirmed from the testing summary presented in Fig. 1 and the Supplemental Material [62]. However, we also see that the MB16-43 benchmark set identifies an example set of problems where we can still learn more from the Lindhard-screening logic (summarized in Sec. II) and the screened-exchange gradient expansion result [46] that underpins CX and hence AHCX [43].

G. CO adsorption on Pt

Figure 8 presents a schematics of CO/Pt(111) contrasting the atomic configurations in two competing adsorption sites, denoted "TOP" (for being on top of a surface atom) and "FCC" (for being in a position that corresponds to an extension of the face-centered cubic atomic organization of the Pt substrate). We note that the CX has a lattice constant

that is in close agreement with experimental characterizations of Pt; see Table I. This observation motivates our assessment strategy: to keep the adsorption structure fixed at the CX description. We concentrate on directly comparing and discussing the new XC-functional accuracy in the CO/Pt(111) adsorption within a fixed-nuclei framework.

We compute the site variation in the adsorption or binding energy

$$E_{\text{bind}}^{\text{TOP/FCC}} = E_{\text{CO/Pt}}^{\text{TOP/FCC}} - E_{\text{Pt,surf}} - E_{\text{CO,mol}}, \quad (18)$$

where $E_{\text{Pt,surf}}$ ($E_{\text{mol}}^{\text{CO}}$) represents the energy of the clean surface (isolated molecule) and where $E_{\text{CO/Pt}}^{\text{TOP/FCC}}$ denotes the total energy of the adsorption configuration, as described with CO at the TOP or FCC site. We focus on discussing the site-preference energy
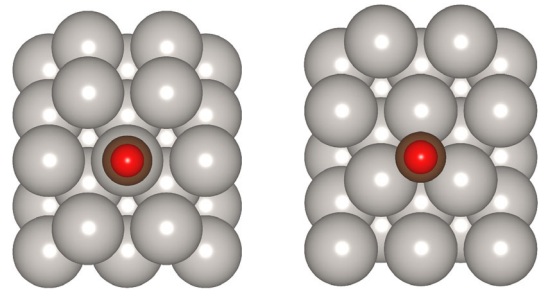

FIG. 8. Schematics of the CO-on-Pt(111) problem: Competition between TOP- and FCC-site adsorption. The image is generated using the VESTA program [207].

TABLE V. Comparison of TOP- and FCC-site CO/Pt(111) binding energies E_{bind}, site-preference energies $\Delta E_{site} = E_{bind}^{TOP} - E_{bind}^{FCC}$, as well as molecular-gap results E_{gap}^{CO} (all in eV). The first and second blocks are for CX-AHCX and B86R-AHBR, respectively. For both tool chains, we also illustrate the impact of the choice of the Fock mixing (as identified in the functional-label subscript). All results are provided for the CX-provided substrate lattice constant $a_0 = 3.929$ Å, molecular structure, and adsorption-induced deformations. Experimental observations of CO adsorption find TOP-site adsorption with binding energy $\Delta E_{site} = -1.32$ eV [208].

	CX	AHCX	AHCX$_{0.25}$	B86R	AHBR$_{0.20}$	AHBR
E_{bind}^{TOP}	−1.830	−1.949	−1.974	−1.683	−1.801	−1.824
E_{bind}^{FCC}	−1.966	−1.954	−1.940	−1.780	−1.767	−1.752
ΔE_{site}	0.133	0.005	−0.034	0.097	−0.034	−0.072
E_{gap}^{CO}	7.048	8.768	9.192	7.081	8.798	9.222

$$\Delta E_{site} = E_{bind}^{TOP} - E_{bind}^{FCC}. \qquad (19)$$

Experimental studies clearly indicate that TOP-site adsorption (at binding energy −1.30 eV) applies for dilute coverage at room temperatures (corresponding to 0.026 eV) [208]. The results obtained using the random-phase approximation concurs with these observations [209].

Accordingly, DFT calculations with an accurate XC functional should find ΔE_{site} negative and with a magnitude that exceeds the 0.026-eV value. However, this problem is a long-standing challenge for DFT, in the sense that essentially all non-vdW-DFs (including HSE and PBE0 [151,152]) fail when considered at or close to the actual Pt lattice constant [17,92,210–216]. We observe that density-driven errors are expected to complicate the DFT setting of the correct CO/Pt(111) adsorption-site preference [92].

Table V summarizes our comparison of RSH vdW-DF performance for the classic CO/Pt(111) problems. We note that the AHBR lattice constant for Pt is slightly larger (and further from experiment) than the CX choice we use. An AHBR adsorption study at the AHBR lattice constant will have a more narrow Pt d band and therefore yield smaller adsorption energies [92,212–214,216–218].

We find that neither CX nor the default AHCX description (using a 0.20 fraction of Fock-exchange mixing) offers an improvement in the description of the site-preference challenge. In contrast, the new AHBR works (as do AHBR$_{0.20}$ and AHCX$_{0.25}$), bringing the site-preference description in alignment with experimental observations. Still, the AHBR does not offer a complete resolution of the CO/Pt(111) problem because it is overestimating the actual adsorption energy E_{bind}.

Figure 9 presents a mapping of correlation between the CO gap and the site-preference energy, as obtained in the CX-AHCX chain of functionals and in the B86R-AHBR chain. The adsorption is often discussed in terms of the Blyholder model [219] and, as such, controlled by the
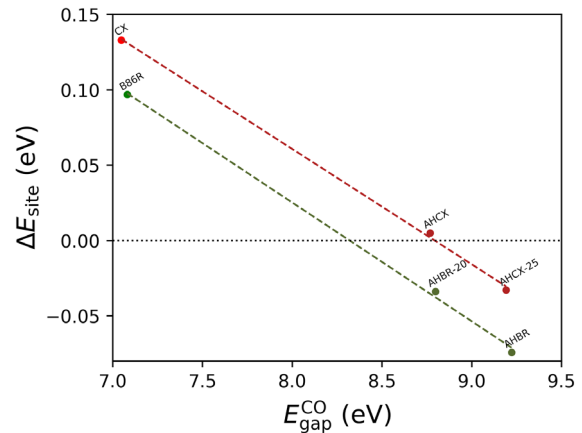

FIG. 9. Correlation between the results for the CO molecular gap E_{gap}^{CO} and for the CO/Pt(111) site-preference energy ΔE_{site} as computed in the CX-AHCX functional chain and B86R-AHBR functional chain. We keep the adsorption geometry fixed in all studies.

substrate electronic structure (which we must accurately characterize to correctly describe the molecule-to-substrate charge transfer) and the molecular gap (that we must accurately characterize to correctly describe the back donation). We keep the adsorption geometry fixed in all calculations, and thus contrast the direct effects that the functionals have on both the molecule gap and substrate electronic structure [220].

There are several lessons from Fig. 9. First, there is a strong impact on the molecular gap by moving from a regular function to the associated RSH. Second, this gap variation effectively controls the prediction of site preference within a given tool chain. Third, there is also a systematic effect of switching between the tool chains and thus changing the substrate electronic structure. In effect, the figure documents that the well-defined AHCX-AHBR differences (in terms of nonlocal-correlation and exchange-design details) have a direct impact on the Pt(111) electronic description. This impact is making the AHBR better at reflecting the true site variation in the CO/Pt(111) adsorption energy.

H. CO$_2$ adsorption in Mg-MOF-74 and m-2-m-Zn$_2$(dobpdc) MOFs

Figure 10 contrast the nature of CO$_2$ adsorption in the simpler Mg$_2$(dobdc) known as Mg-MOF-74, upper panel, and in the more complex case of the diamine functionalized m-2-m-Zn$_2$(dobpdc), lower panel. The panels show atomic coordinates as obtained in fully relaxed CX character-izations that form the starting points for our performance comparisons and discussion.

Here we assert the AHBR (and AHCX) performance by systematically calculating the CO$_2$ binding enthalpy at room temperature H_{ads}^{room} for Mg-MOF-74 and the Born-Oppenheimer (frozen-atom) binding energy
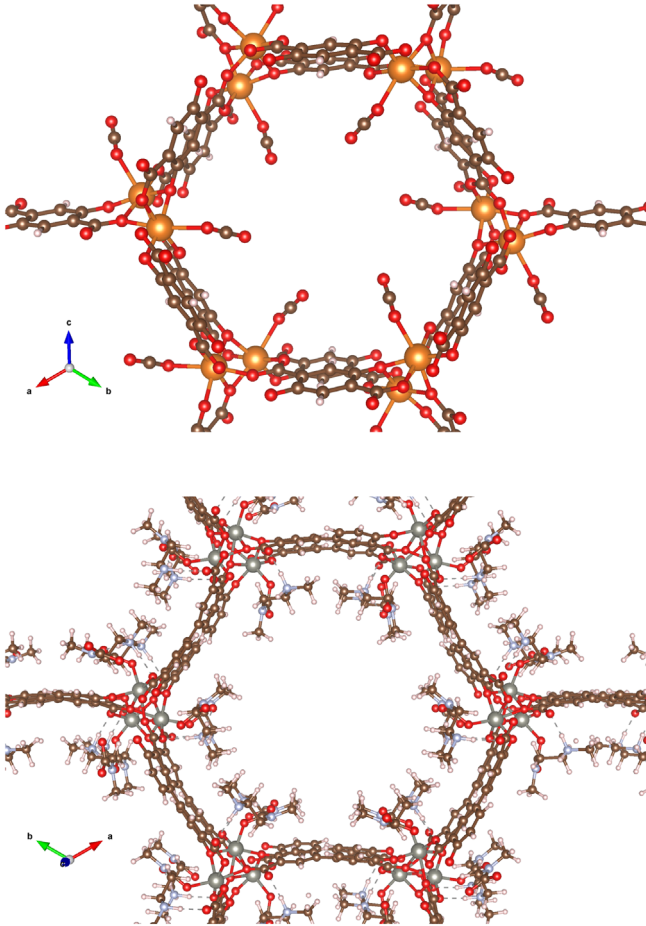
FIG. 10.   Optimized crystal structures of CO_2-adsorbed Mg-MOF-74 (upper panel) and CO_2-inserted m-2-m-Zn_2(dobpdc) (lower panel). The gray, orange, red, sky blue, brown, and pink circles represent Zn, Mg, O, N, C, and H atoms, respectively. The images are generated using the VESTA program [207].

$$E_{ads,BO} = E_{CO_2\text{-}MOF} - (E_{MOF} + E_{CO_2}) \qquad (20)$$

in the larger (more expensive) case of the diamine-functionalized MOF. In Eq. (20), we evaluate the difference between the total energy of CO_2-adsorbed MOF ($E_{CO_2\text{-}MOF}$) and the total-energy sum of Mg-MOF-74 or m-2-m-Zn_2(dobpdc) (E_{MOF}) and gas phase CO_2 (E_{CO_2}). For the gas phase CO_2 energy, we optimize the geometry within a $20 \times 20 \times 20$ Å^3 cubic cell. We verify that our computational setup Appendix A converges the CO_2 binding-energy results for Mg-MOF-74 and m-2-m-Zn_2(dobpdc) adsorptions to 1 kJ/mol.

To simplify the comparison among functionals, and to limit computational costs, we provide all calculations with the MOF structures kept fixed at the CX results for the adsorption geometry. This strategy is similar to that we use for discussing the CO/Pt(111) problem, above. However, in the case of carbon capture in Mg-MOF-74, we permit the CO_2 molecules to relax according to the forces that we compute in the specific functionals.

We seek to compare with room-temperature measurements of the CO_2 heat of adsorption, H_{ads}^{room} [76,81]. The DFT (and the true) internal-energy-binding description are thus affected by vibrational zero-point energy (ZPE) and thermal-energy (TE) corrections:

$$H_{ads}^{room} = E_{ads,BO} + \Delta ZPE + \Delta TE. \qquad (21)$$

Accordingly, for the simpler Mg-MOF-74 system, we also compute and contrast the vibrational frequencies of adsorbed CO_2 and free CO_2 using a finite-difference approach with the PHONOPY package [221]. Specifically, we displace each atom of CO_2 in 12 random directions with a constant displacement distance (0.03 bohr) to extract corrections $\Delta ZPE + \Delta TE$ that hold at 298 K.

In the larger, more complex diamine-functionalized case, we stick with comparing the Born-Oppenheimer results, Eq. (20), directly with the measured $H_{ads}^{room} = -57$ kJ/mol value. Based on experience from asserting the performance of density-explicit vdW-DFs, in Ref. [44], we expect that a plausible back-corrected experimental value would be approximately -63 to -60 kJ/mol as the computed $\Delta ZPE + \Delta TE$ value is about 3–6 kJ/mol (see Ref. [44]).

Table VI compares our results, contrasting the vdW-DF tool-chain descriptions of CO_2 uptake in the Mg-MOF-74 (in the diamine-functionalized MOF) with experiments in the upper (lower) section. In the case of Mg-MOF-74, we

TABLE VI.   Comparison of performance for AHBR and for the CX-based tool chain on the CO_2 adsorption energies in Mg-MOF-74, top section, and in m-2-m-Zn_2(dobpdc), bottom section. All calculations are performed at the CX characterizations for the MOF geometries. For Mg-MOF-74, we permit the CO_2 to relax as described in the stated functional and list the results for the characteristic bond length. We present energy (bond length) results in kJ/mol (in Å) to facilitate an easy comparison with a recent MOF study covering regular vdW-DFs and revPBE + D3 [44]. The subscript "BO" identifies Born-Oppenheimer results, while the superscript "room" identifies adsorption free-energy values that include the effects of vibrations as described at room temperature, using Eq. (21) to facilitate a direct comparison to experimental values for Mg-MOF-74. The values in parentheses represent an estimate of how a back correction for vibrations would impact the measured m-2-m-Zn_2(dobpdc) $H_{ads}^{room} = -57$ kJ/mol value [81].

	CX[a]	AHCX	AHCX$_{0.25}$	AHBR	Experiment
Mg–O	2.29	2.27	2.26	2.25	2.27[b]
$E_{ads,BO}$	-53.7[a]	-58.5	-59.7	-50.3	$\cdots$
ΔZPE	2.8	2.4	2.5	2.6	
ΔTE	1.1	1.6	1.3	1.1	
H_{ads}^{room}	-49.7	-54.5	-55.9	-46.6	-43.5[b]
$E_{ads,BO}$	-94.6	-98.7	-99.7	-86.8	-57[c] (-63–-60)

[a]Reference [44].
[b]Reference [81].
[c]Reference [78].

find that the AHCX result for the Mg-O distance is excellent but that AHBR is also accurate. For adsorption energies, we find that AHCX systematically strengthens the CX binding results in both MOF cases. In the complex diamine-functional MOF case, we therefore find that moving to AHCX does not repair a clear overbinding tendency that we have very recently documented for present vdW-DFs [44].

In contrast, the results for CO_2 adsorption in the new RSH vdW-DF shows a trend of vdW-DF repairing. The AHBR result $H_{ads}^{room} = -46.6$ kJ/mol for the Mg-MOF-74 is in itself excellent, being in close agreement with the experimental value -43.5 kJ/mol [81]. The AHBR outperforms all of the vdW-DFs that we have previously tried (see Supplemental Material associated with Ref. [44]), for example, lifting the underbinding B86R $H_{ads}^{room} = -38.9$ kJ/mol value.

Meanwhile, in the case of the diamine-functionalized MOF [44], the AHBR $E_{ads,BO} = -86.8$ kJ/mol result instead lowers the clearly overbinding B86R $H_{ads}^{room} = -92.1$ kJ/mol value [44] toward the value of the measurement, at -57 kJ/mol [78]. According to previous vdW-DF experience in characterizing vdW-DF vibrational corrections to $E_{ads,BO}$ [44], this AHBR characterization leads to the estimate $H_{ads}^{room} \approx -84$ to -81 kJ/mol. The AHBR therefore outperforms SCAN, SCAN + rVV10, and the recent vdW-DFs (vdW-DF1 and vdW-DF2 are better on energies but have too-long binding lengths). The AHBR has an accuracy that matches the semiempirical rVV10 for this MOF challenge [44]. Unlike in the case of Mg-MOF-74, the AHBR does not perform at the revPBE + D3 level for m-2-m-Zn_2(dobpdc). However, unlike the AHCX, the AHBR is able to move the nonempirical vdW-DFs toward a binding softening. Robustness, a repairing behavior (documented here and for many density-driven challenges), is needed when the vdW-DF method faces significant charge relocations that, in turn, challenge the XC balancing [44].

I. Base-pair stacking in a DNA model

DNA can be seen as a stacking of Watson-Crick (WC) base pairs that are essentially flat and therefore have a significant (eV-scale) vdW attraction [25–29,86,222–224] from one base pair to the next. The WC pairs are steps in the resulting double-helix DNA structure. There are in total ten possible combinations for two steps, i.e., base-pair combinations that are here denoted ApA, ApT, ApC, ApG, CpC, CpG, GpC, TpT, TpC, and TpG; Ref. [225] identifies and illustrates a set of possible atomic positions for these base-pair combinations. We want to compute such base-pair stepping energies [26,27] since the mutual vdW attraction might have driven the DNA self-assembly in the first place, as life emerged [226,227].

Some of the DNA cohesion comes, of course, from the presence of the sugar-phosphate backbones that incorporate and organize the WC bases into two strands, with the

sequence of WC bases adenine (*A*), thymine (*T*), cytosine (*C*), or guanine (*G*) setting the genetic code. The strands are complementary in the sense that the WC-base sequence must be exactly matched, with each of the individual bases having only one suitable counter part, i.e., forming steps that must have one of the *A-T*, *T-A*, *C-G*, or *G-C* forms. The base-pair-combination nomenclature, ApA though TpG, reflects the observation that it is sufficient to track the code sequence on one of the DNA strands. The DNA strands are mutually bonded by a combination of hydrogen and vdW binding [42], but the energy of the WC pairings (*A-T*, *T-A*, *C-G*, *G-C*, among one base and its counterpart directly across) is not our present focus. Instead, we seek to understand the extent that the mutual step-binding energies contribute to the DNA cohesion, using a DNA model that ignores the backbone but instead relies on hydrogen terminations of the bases [26,27,225].

To set us up for future, more general DNA explorations, we contrast the performance of the first and second vdW-DF tool chains relative to the reference descriptions provided in Ref. [225]. That is, we compare with so-called domain-based pair natural orbital coupled-cluster [DLPNO-CCSD(T)] calculations [228] at fixed reference base-pair combination structures [225]. The DLPNO-CCST(T) method is also used for setting reference energies of the GMTKN55 suite [69]. We compute the base-pair stepping energies as total-energy differences between the full system and the two WC base pairs, for example, in the case of the ApC combination

$$\Delta E_{WC\text{-step}}^{ApC} = E_{ApC} - E_{A\text{-}T} - E_{C\text{-}G}. \tag{22}$$

The reference work [225] also provides data for the sum of pair interactions among the four bases $\Delta E_{B\text{-pair}'}$, excluding the two WC pairings (as indicated by the prime). This pair summation is illustrated in the abstract figures of Refs. [225,229].

Tables SXVI and SXVII of the Supplemental Material [62] compare the performance of CX, AHCX, AHCX$_{0.25}$ and B86R, AHBR$_{0.20}$, and AHBR for each of the base-pair combinations, reporting (in kcal/mol) the $\Delta E_{WC\text{-step}}$ and $\Delta E_{B\text{-pair}'}$, respectively. We also report mean deviation and MAD values relative to the DLNPO-CCSD(T) calculations [225]. Table VII summarizes the performance comparison (in terms of ten-base-pair-combination averages) and makes it clear that the AHBR is a strong performer for the description of the DNA base-pair assembly.

We find that B86R performs better that CX and that the AHBR functional design is in fact very accurate also for descriptions of the DNA stepping energies. This is especially true when it is used in the suggested default mode with a 0.25 Fock-exchange mixing. The description is significantly more accurate than a standard choice of the dispersion-corrected hybrid that DFT provides, as also listed in Table VII. This result is in itself encouraging.

TABLE VII. Comparison of the CX-based and B86R-based tool-chain performance for DNA assembly. We report MAD values (in kcal/mol) as extracted by averaging the deviations of vdW-DF results relative to coupled-cluster calculations [225] on the ten different base-pair stacking configurations, using the specific configurations that are provided in Ref. [225]. We report on ONCV-SG15/160 Ry results, but we also compare with the literature values as well as an assessment obtained from a separate ultrasoft-PP study ("GBRV"). The reference calculations use DLPNO-CCST(T) [228] to compute the step energy $\Delta E_{\text{WC-step}}$ and $\Delta E'_{B\text{-pair}}$ which is a sum over relevant molecular-pair contributions.

XC study	$\Delta E_{\text{WC-step}}$	$\Delta E'_{B\text{-pair}}$
B3LYP + D3[a]	0.89	...
CX[b]	1.73	0.44
CX$^{\text{GBRV}}$	1.17	1.49
CX	1.48	1.75
AHCX	3.06	3.30
AHCX$_{0.25}$	3.47	3.69
B86R	0.38	0.82
AHBR$_{0.20}$	0.12	0.60
AHBR	0.08	0.52

[a]Reference [225].
[b]Reference [229].

We also observe that the AHBR is somewhat less accurate when it is instead used to study energies from the sum of pair contributions, $\Delta E_{B\text{-pair}'}$. As in Ref. [229], we find that the vdW-DF-based descriptions of the stepping energies benefit from a cancellation of errors that affect the descriptions of pairing between individual bases.

Finally, Table VII reveals an important difference between the performance trend in the CX-AHCX and B86R-AHBR functional chains for this class of large molecular problems. We find that moving to a hybrid form significantly worsens the CX and AHCX descriptions, whereas we find that such a step slightly improves the B86R- and AHBR-type description. In both tool chains, we find that including and increasing the Fock-exchange fraction strengthens the interactions, but the changes are small in the AHBR case. Including Fock exchange makes AHBR very accurate, but the most important lesson is perhaps that the B86R-AHBR functionals have an inherent stability here: They start and remain accurate on the DNA assembly energies.

IV. CONCLUSION AND OUTLOOK

We develop a new, accurate, nonempirical RSH vdW-DF termed vdW-DF2-ahbr, and we document general-purpose capabilities for molecular problems as well as promise for bulk and adsorption properties. Since AHBR is based on a range separation of the Coulomb interaction, it is set up (and coded) to allow for the use of a physics-based tuning of both the Fock-exchange mixing α and the RSH inverse screening length γ. This means that it is also possible to

ameliorate residual RSH vdW-DF errors in charge-transfer descriptions [165]. In this first presentation, however, we deliberately keep these values fixed to allow a simple demonstration of broad AHBR capabilities and usefulness.

Figure 1 and Figs. S1 and S2 of the Supplemental Material [62] highlight two important takeaway messages of this paper: (1) The use of RSH vdW-DFs, and the new AHBR in particular, provides substantial accuracy improvements over regular, density-explicit vdW-DFs for broad molecular properties, and (2) using the B86R-based hybrids, i.e., the DF2-BR0 and the here-defined AHBR, provides an evenly robust performance, heightening the accuracy over all types of molecular problems.

Figures 1 and 5 exemplify a key conclusion of the AHBR advantage: It has robust ability to navigate so-called density-driven DFT errors [90].

This vdW-DF2-AHBR resilience, in combination with its emphasis on a MBPT foundation, suggests that it will be accurate also beyond the successes that we document here for a set of DFT challenges in molecule, layered, bulk, and surface systems. When using formal MBPT to compute the total energy, there is an inherent robustness toward making approximations [137]. That robustness also extends to the exact XC-energy functional [138]. We rely on MBPT guidance in making XC-energy approximations (such as CX, AHCX, and AHBR) so that these vdW-DFs can potentially benefit from that inherent robustness. However, as we also discuss, such benefits can emerge only in practice when the actual XC-functional approximation delivers accurate orbitals, for example, as tested on the quality of its density description [90]. That AHBR matches or exceeds B3LYP/HSE + D3 for transition-state problems means that it generally navigates density-driven errors and therefore outperforms the B3LYP/HSE + D3 broadly, for example, as summarized in Figs. S1 and S2 of the Supplemental Material [62]. Like the HSE + D3, it has both a strong resilience to density errors and the MBPT foundation to benefit from the formal-MBPT robustness toward XC-functional approximations [137,138].

We argue that this general-purpose character suggests that AHBR should be used to map strengths and weaknesses of the vdW-DF method on molecules, just like the AHCX can serve us in that role for bulk systems [18].

An overall outcome of this vdW-DF2-AHBR work is also a roadmap with a DFT-usage feedback strategy for making further functional improvements in the vdW-DF framework. Since both the AHCX and AHBR are found to be fairly robust in all tested problems, we can contrast performance differences over a broad range of systems. Furthermore, since the pair of RSH vdW-DFs have systematic design differences, we can correlate the performance differences in terms of the nature of the underlying physics input to the XC designs. The AHBR and AHCX are particularly useful because they are complementary, representing one of two internally consistent classes of MBPT input on how exchange effects impact all XC

components. Specifically, as we explain in Secs. II. A and II. B, the AHBR and AHCX rely on valid but different interpretations of formal MBPT. They correspond to systematic reliance of molecular or a weakly-perturbed-bulk perspective on screening, respectively. Taken together, the observations allow us to interpret the DFT-usage feedback and draw development conclusions concerning which types of MBPT inputs to prioritize. This DFT-feedback strategy is in many ways just a continuation of the electron-gas tradition that, as we see it, has pushed MBPT-based DFT from LDA over constraint-based GGAs and the vdW-DF method.

ACKNOWLEDGMENTS

APPENDIX A: COMPUTATIONAL DETAILS

All calculations are carried out using the QE code suite [153–155], using an in-house coding for the AHBR design. The AHBR code will be released to QE once the paper is accepted for publication.

For hybrids, we use the adaptive-compressed-exchange (ACE) implementation [155,171] to speed up the Fock-exchange evaluation (except in a few cases—ionized Li, Na, and K atoms—where it seems to prevent an easy convergence). We use the spin vdW-DF formulation [13] (for regular and hybrid vdW-DFs [18]), when relevant.

We systematically use the ONCV-SG15 [230,231] set of PPs at a 160-Ry wave-function-energy cutoff for all of the here-reported molecular, layered-material, and bulk benchmarking as well as for demonstrator work on base-pair stepping energies in DNA assembly and for a description of CO/Pt(111) adsorption. To document the PP sensitivity, we also provide a characterization of the DNA base-pair stepping energies using the ultrasoft GBRV PP set [232] at 50-Ry wave-function-energy cutoff and 400-Ry density cutoff. For a RSH vdW-DF demonstration on green-technology problems, we calculate the CO_2 binding enthalpy in Mg_2(dobdc) [75,81] known as Mg-MOF-74, and in the diamine-appended or -functionalized m-2-m − -Zn_2(dobpdc) [44,76,78] using the ONCV-SG15 PPs with a wave-function-energy cutoff of 220 Ry.

For the molecular benchmarking, we use a Γ-point-only wave-vector sampling, and we employ the same cubic unit-cell size for all systems within a given benchmark set. The size is determined automatically in a PYTHON setup of QE input files. This is done by first finding the largest Cartesian-coordinate extension (among all set-specific problems) and then systematically adding an extra 10-Å vacuum in all directions. This vacuum padding ensures that there is at least 10 Å between the largest x, y, and z position of one image to the smallest x, y, and z position in the next in all of the GMTKN55 benchmarks. Having a cubic cell, we can use the Makov-Payne correction [233] to help control spurious electrostatics coupling among the periodic images in our plane-wave setup.

Appendix B describes the nature of our strategy to secure convergence at the 0.01 kcal/mol level for benchmarking across the full GMTKN55 suite. The argument has three steps. First we show—in a pilot survey relying on the more electron-sparse ABINIT PPs [234] at 80 Ry—that the impact of false vdW attraction on the per-benchmark MAD values never exceed 0.01 kcal/mol; see Table SXII of the Supplemental Material [62]. Here we use an in-house code to extract the asymptotic vdW-DF interactions (among unit cells) that, as discussed in Refs. [5,24,235], can be formulated in terms of per-unit-cell effective molecular C_6^{mol} coefficients and a molecular E_{vdW} attraction-energy estimate [235].

Next, Table VIII summarizes our survey of the impact caused by spurious intercell electrostatic couplings that we find is also limited at 0.01 kcal/mol. This documentation is again done in a pilot study approach (using the ABINIT PPs [234]) by direct QE calculations, using the automatic setups but changing the assumed vacuum padding from 10 to 15 Å (as indicated by subscripts). The comparison is provided for a subset (the easily accessible GMTKN53 [17]) of the GMTK55 suite, that is, excluding (in the GMTKN55 groups identified by asterisks) the G21EA and WATER27 benchmark sets and suitably adapting the WTMAD1 measures [17].

Finally, the cornerstone of our here-presented molecular-benchmarking strategy and the main message of Appendix B is the following. While negative ions and small radicals in the G21EA and WATER27 benchmarks present fundamental computational challenges [89], we can still complete well-converged full GMTKN55 assessments in plane-wave DFT.

TABLE VIII. Size convergence of functional-performance assessments: Pilot study comparison of characteristic WTMAD1 values [17,69] (in kcal/mol) as obtained for "GMTKN53," a 53-benchmark part [17] of the GMTKN55 suite [69]. We contrast the plane-wave performance characterizations that result when using a standard 10-Å and a larger 15-Å choice of vacuum padding (see text). The convergence tests are done for the ABINIT PP set [234], at 80-Ry wave-function cutoff. We focus on the "easily accessible GMTKN53" subsuite [17] that excludes (as indicated by asterisks) the G21EA benchmark set from the GMTKN55 [69] group 1 and the WATER27 set from the GMTKN55 group 4. This is done because these sets require a separate dielectric handling [193,236]; see Appendix A.

Tests	CX (10 Å)	CX (15 Å)
Group 1*	5.19	5.20
Group 2	4.93	4.92
Group 3	7.22	7.22
Group 4*	3.36	3.35
Group 5	3.78	3.79
Group 6 (4* and 5)	3.55	3.55
GMTKN53 (GMTKN55*)	4.79	4.79

The challenges exist because small negative systems have pronounced SIEs [89] that make it impossible (impractical) to complete a direct plane-wave assessment on the G21EA (WATER27) set [17,18]. Specifically, the highest-occupied level of some small charged systems will eventually be pushed above the vacuum level of the plane-wave-DFT potential, exactly because we seek size convergence [237]; see Refs. [17,89] and Appendix B. However, the electrostatics-plus-SIE nature of the challenge [17,89] suggests the workaround: We pursue plane-wave-GMTKN55 benchmarking in the presence of fictitious dielectric constants $\varepsilon_\infty > 1$ and then adiabatically remove this environment perturbation.

For our survey of the bulk-structure performance of AHBR, we use again the ONCV-SG15 PPs at 160 Ry, now with an $8 \times 8 \times 8$ k-point sampling (keeping all k-point differences in the ACE-based Fock-exchange evaluation [155,171] for hybrids). This choice of setup permits direct comparisons with previously reported CX and AHCX results [17].

Comparing with DMC results [173–176,183] for the graphite crystal (graphene, α-graphyne, and hBN bilayers), we use an $8 \times 8 \times 6$ ($8 \times 8 \times 1$) k-point sampling, keeping half of the k-point differences in the Fock-exchange evaluations, generally using CX to first establish a description of the in-plane atomic structure (that is kept fixed while we vary the layer separation and compute the energy variation in different regular and RSH vdW-DFs). System energies $E(d)$ computed at unit-cell height $2d = 40$ Å and with layer separation $d = 20$ Å are used to estimate the E_{asymp} reference values in Eq. (16). This choice is motivated by observing that for regular graphite-AB, we find

$E(d = 20 \text{ Å}) - E(d = 18 \text{ Å}) = 0.2$ meV for the four-atom unit cell. Using instead the $d = 18$ Å results as references would cause but a vanishing offset in the binding-energy descriptions, Eq. (16).

For a study of the layered phosphorus crystal [177], we note that one of the in-plane lattice constants is sensitive to pressure [238] and hence, likely sensitive to the functional approximation. We therefore keep the in-plane lattice constants fixed at the experimentally observed values [238] $a = 3.3133$ Å and $c = 4.374$ Å. Additionally, we first determine the intra-P-layer structure using CX at that given unit-cell description. This gives an in-layer atom configuration that agrees to within 1% of the experimental distance and angles reported in Ref. [238]. The CX-specified atomic configuration for the individual layer is kept fixed as we subsequently compute the crystal total-energy variation at varying choices of the cell height $2d$ (where d is set by the layer-separation definition that is used in the DMC study [177]).

For the CO/Pt(111) adsorption demonstrator of AHBR usefulness, we use a six-layer surface slab (with two-by-two in-surface repetition) together with a $6 \times 6 \times 1$ k-point sampling (here keeping a $3 \times 3 \times 1$ grid of k-point differences in hybrids studies), as before with the use of the ONCV-SG15 setup. The B86R (and AHBR) is found to have slightly larger lattice constants than the CX and AHCX descriptions. That may favor AHBR over AHCX in terms of accurate predictions of the adsorption site preference, although the lattice-constant differences are small. We eliminate this indirect effect by making the toolchain comparison at the frozen geometry that results when CX tracks the adsorption-induced relaxations. We note that CX is accurate on the Pt lattice constant and on the elastic-energy description [17]. Our frozen-geometry approach can therefore be considered a good model of the actual CO adsorption problem.

For the carbon-capture-usage illustration, we characterize CO_2-in-Mg-MOF-74 adsorption and CO_2 insertion in diamine-functionalized m-2-m–Zn_2(dobpdc), focusing on adsorption energies and using a Γ-point sampling of the Brillouin zone for Mg-MOF-74 and a $1 \times 1 \times 3$ k-point grid sampling for m-2-m–Zn_2(dobpdc). For the Mg-MOF-74 case, we also determine CO_2 vibrations and can thus compare directly to room-temperature observations of the heat of CO_2 adsorption. Here we first use CX to compute the unit-cell structure and identify the adsorption geometry. For the Mg-MOF-74 case, we proceed to determine functional-specific relaxations for the CO_2 molecules, using the access to forces. For the significantly larger m-2-m–Zn_2(dobpdc) system, we rely systematically on a CX characterization of the adsorption. We characterize the CO_2 vibrations in the Mg-MOF-74 in a finite-distortion setup using PHONOPY [221].

Finally, we provide illustrations of using AHBR (and AHBR and B86R tool chain) in both a biomolecular and a

carbon-capture setting. For the biomolecule illustration, we compare with coupled-cluster reference calculations for a model that replaces the DNA backbone with hydrogen terminations on the individual bases [26,27,225]. Here, we perform Γ-point calculations for the set of ten different two-base-pair combinations (at representative geometries identified in Ref. [225]) using a 30-Å-cubed unit cell and electrostatic decoupling. In effect, we thus assert the AHBR on energies that characterize the DNA assembly.

APPENDIX B: PLANE-WAVE MOLECULAR BENCHMARKING

This appendix summarizes our strategy for completing a plane-wave molecular benchmarking across the full GMTKN55 suite [69]. In particular, we explore the nature and impact of convergence-related factors that make benchmarking challenging, but which, as we show, can also systematically be handled and circumvented. As such, this appendix motivates and validates the molecular benchmarking that we also report in this paper.

1. Impact of spurious vdW attraction

Our focus on nonlocal-correlation functionals presents, in principle, a problem for plane-wave benchmarking: The vdW attraction is long-ranged and causes at least some spurious coupling between the periodically repeated images. However, we can document that the net impact by false, intercell vdW coupling on each of the GMTKN55 benchmarks is vanishing, well within our overall benchmarking target of 0.01 kcal/mol [237]. To that end, we consider the asymptotic limit of the vdW-DF method [5,24,235].

We proceed as follows. First, for the atomic configurations of molecules or cluster (in each of the roughly 2450 different atomic configurations that define the GMTKN55 suite [69]), we evaluate an effective molecular or cluster C_6^{mol}-interaction coefficient. These coefficients characterize the spurious vdW couplings in the asymptotic vdW-DF limit that is defined and used in Refs. [24,235]. Here we use an in-house extension of the QE code suite, starting on a set of CX calculations for the self-consistent electron-density variation. This initial step is done in a pilot study using the more electron-sparse ABINIT PPs [234] at 80-Ry cutoff, and typically in our standard benchmarking setup, i.e., with a minimum of 10-Å vacuum padding in the choice of unit cells. However, we use smaller unit-cell sizes in the G21EA set and for the negatively charged OH^- radical in the WATER27 set [18], for reasons that are further discussed below.

We also compute (for every unit-cell problem in GMTKN55) a corresponding interaction-energy contribution to a given unit cell i [235],

$$E_{\mathrm{vdW},i} = -\sum_{j \neq i} \frac{C_6^{\mathrm{mol}}}{|\mathbf{R}_j - \mathbf{R}_i|^6}. \quad \text{(B1)}$$

Here, $\mathbf{R}_j$ denotes a Bravais vector of the periodic computational setup in our QE calculations. We observe that this measure of asymptotic vdW attraction, Eq. (B1), is different from a full vdW-DF method study [24] on fundamental reasons that are discussed in Refs. [9,235]. We would not, for example, get exactly the same values if we track the spurious coupling in a supercell study. However, we are setting up a molecular benchmarking with a large vacuum padding; see Appendix A. The use of Eq. (B1) is therefore an acceptable approximation that can gauge the expected magnitude of spurious vdW coupling in our plane-wave calculations.

Table SXII in the Supplemental Material [62] illustrates how we use Eq. (B1) to validate that the spurious vdW impact on our benchmarking is truly neglectable. From Eq. (B1), we determine the extent that the spurious intercell-vdW coupling is causing an offset on the periodic-cell vdW-DF results, for each of the 1500 molecular-process energies in the GMTKN55 suite [69] (roughly 2450 single-point calculations per functional). Next, we define a set of 55 per-benchmark MAD-offset values by tracking the offset relative to the reference energies. Table SXII in the Supplemental Material [62] reports these benchmark-specific error estimates in descending order (truncated to five sets). The largest impact seems to appear for the G21EA set, but that impact estimate is also an exaggeration. This is because we dump the pilot study to a reduced unit-cell size (8–10 Å total) whenever we face convergence issues for the negatively charged ions and small radicals in the G21EA set [17,18,89]. Table SXII of the Supplemental Material [62] makes it clear that the false vdW impact on our plane-wave molecular benchmarking is significantly less that 0.01 kcal/mol.

2. Impact of spurious electrostatic coupling

Table VIII provides documentation that we use a sufficiently large plane-wave-benchmarking setup. The table summarizes the following testing that our use of a standard 10-Å vacuum padding (in our automatic scripting of QE input files) is sufficient to ensure an electrostatic decoupling among the images in the periodic-cell setup, bringing the assessment error down to a desired 0.01 kcal/mol limit [237] for averaged measures.

This validation of our benchmarking strategy is done brute force, that is, by repeating a standard CX testing with one where instead we use a 15-Å vacuum padding. Again we use the ABINIT-PP setup (at 80 Ry) but otherwise follow the regular problem specifications for all of the individual problems. However, the focus is limited here to the easily accessible GMTKN53 subset of the GMTKN55, excluding the G21EA and WATER27 sets, as was also done in Ref. [17].

We find (see Table VIII) that the net impact of going to a truly large vacuum padding in the setup is bounded by 0.01 kcal/mol. Here the assessment is done in terms of

the weighted WTMAD1 measures as resolved on the GMTKN55 bench groups. As indicated by asterisks, the reported WTMAD1 measures are slightly adjusted (as described in Ref. [17]) due to the GMTKN53 focus. We deem the use of our standard (10 Å) vacuum padding setup (see Appendix A) validated also in terms of securing sufficient electrostatic decoupling [237].

3. Instabilities driven by self-interaction errors

A plane-wave-benchmarking setup like ours can technically reach only a true complete-basis limit [237] when we document size convergence, at least in principle, to the infinite-size limit. Effectively, the QE plane-wave code sets the average potential to zero [239]. This means that, for any finite unit-cell size, the potential value in regions far from the nuclei (in isolated molecule problems) lies slightly above the true vacuum floor. A SIE impact that arises in small negative ions [89] will, in part, be masked by this potential offset in the plane-wave code. For sufficiently small unit-cell sizes, one can even craft a fictitious electron trapping in general XC functionals, even if nonhybrids may not actually be able to trap it at all in a fully converged description [17,18,89]. Unfortunately, a direct discussion of convergence with unit-cell size for all of the GMTKN55 is of limited meaning.

Figure 11 reports a successful (but absurdly tedious and difficult) electronic-structure convergence that we provide for CX (in a plain QE) for the OH⁻ system, as described in our setup for characterizing it in the WATER27 set. Here the use of our automatic (benchmark-specific) setting of the unit-cell size leads to use of a 22.8-Å cell size. This is a highly challenging choice of the unit cell (in terms of convergence) for a negatively charged system, as represented in a plane-wave code. The figure shows the variation of the electrostatic potential along the O-H axis, together with the energy position of the highest-occupied molecular (HOMO) level of the negatively charged radical. The inset focuses on the near-molecule regions and makes it clear that the HOMO level of OH⁻ is similar to but cannot be approximated by the lowest-unoccupied molecular level of the corresponding (spin-polarized but neutral) OH system. The vacuum level of the plane-wave calculation sits here at 0.1 eV above the vacuum floor for description of a truly isolated molecule. This value is estimated by the value that the potential attains at a point farthest from the atoms. The electronic-structure convergence indicates a trapping of the HOMO level at −0.7 eV, well below the vacuum level. Thus, we can ascribe some, but not a complete, trust in this CX-based characterization of the SIE impact [89] on the OH⁻ system.

Still, the convergence of the OH⁻ HOMO level is a cumbersome process involving a convergence ruse: Starting at a low convergence criteria and a significant temperaturelike smearing, we carry out a sequence of DFT calculations that gradually increase the criteria on density consistency and lower the smearing. We find that we must protect against electron defections even after the KS
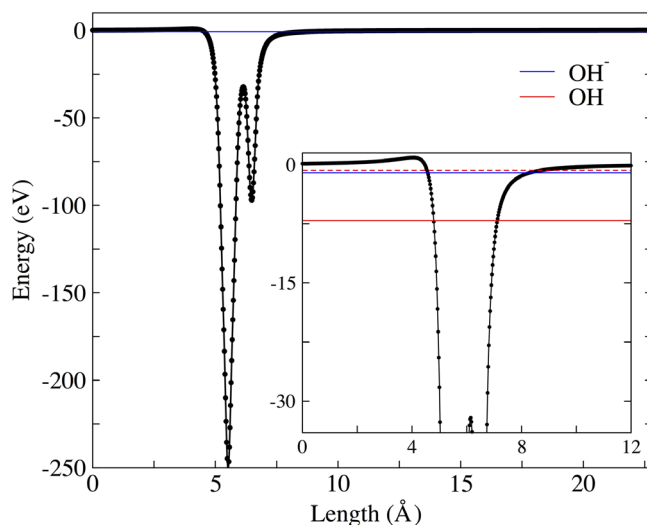

FIG. 11. Convergence challenge for the OH⁻ radical producing potential density-driven DFT errors. The instability here is driven by SIE effects [89], and the potential error is evident by noting a closeness of the highest-occupied molecular orbital (HOMO) energy position and the vacuum level, i.e., the zero-energy value. Convergence of negatively charged ions and radicals is a challenge not only in this CX calculation but for all XC functionals (even hybrids [17]) since we seek a proper size convergence and therefore push our plane-wave calculations close to the complete-basis-set limit [89]. The figure shows the self-consistently computed electrostatic potential along a ray containing the nuclei (potential dips) and OH⁻ bonding region. The QE approximation for the vacuum level is found at the plateau value, here located just above the OH⁻ HOMO level (solid blue horizontal bar). The inset provides a closer look, showing the potential barriers surrounding the molecular regions and tracking differences between the neutral OH lowest-unoccupied molecular level (broken red bar) and the OH⁻ HOMO level.

convergence algorithm begins to trust the existence of an actual HOMO level, and the process takes weeks of human time. The brute-force ruse approach given in Fig. 11 is not practical for a systematic exploration of convergence with unit-cell size for the OH⁻ radical. Worse, an attempt to port such a direct, brute-force strategy to the G21EA set will fail on fundamental grounds [17,89].

We note that these SIE-impact problems are important for DFT usage, yet a general plane-wave-DFT characterization appears impossible [89]. We need to track and understand the problems as they relate to charge-transfer processes, and they point to potentially deeper SIE problems of XC functionals. However, to quantify the SIE impact on the G21EA and WATER27 benchmark sets, we do need to actually trap the HOMO level, and that is not directly possible in a complete-basis approach for some negative ions [89] (and small radicals).

There is a good solution available from analysis [193,236], given the electrostatic nature of the SIE-impact problems in G21EA and WATER27 benchmarking [89].
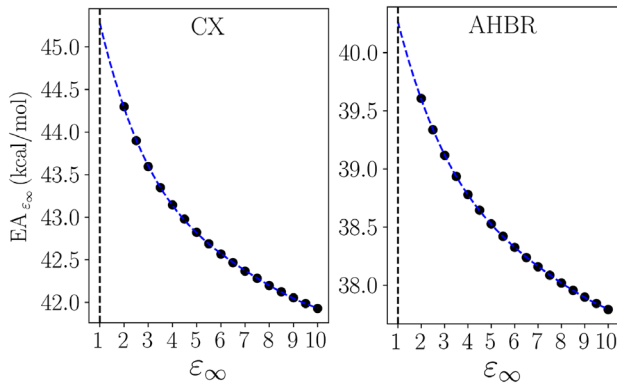
FIG. 12. Robust, environment-extended QE determination of the OH⁻ electron-affinity energies EA in CX (left panel) and hybrid AHBR (right panel). The choice of a fictitious vacuum-dielectric constant $\varepsilon_\infty > 1$ counteracts [193] the SIE-driven instability [89]. The resulting (environment-adjusted) OH⁻ electron-affinity energies $\mathrm{EA}_{\varepsilon_\infty}$ (shown as dots) vary with ε_∞ but have a rapid convergence with the choice of the cell dimensions.

Trapping the HOMO level in a negatively charged small system is difficult (see Fig. 11) because the electrostatic potential, on the one hand, must overshoot to positive values and, on the other hand, will be set by an (unphysical) exponential decay in the crossover to that asymptotic-repulsion region [89]. As a consequence, the trapping region becomes excessively narrow, pushing the would-be HOMO level above the (true) vacuum level, in some cases [89]. Meanwhile, plane-wave DFT sets the average potential to zero; see, for example, Ref. [239] giving an asymptotic potential variation with a floor that will approach the true vacuum (and thus cause QE problems) as we push for size convergence. Frustratingly, our plane-wave benchmarking appears to be foiled by its very strength, namely, that we can fairly easily approach the complete-basis-set limit.

Fortunately, the electrostatic nature of the problem also gives us a way to leverage the plane-wave advantages for size-converged G21EA, WATER27 benchmarking, and hence for complete GMTKN55 assessments. The idea [193,236] is to (1) introduce a control knob that systematically affects the vacuum position in QE, (2) obtain well-defined G21EA and WATER27 assessments as a function of the control-knob value, and (3) extrapolate these estimates as we turn off the controlled stabilization. We simply do perturbation theory in reverse.

In practice, we rely on an electrostatic-environment extension [193] of the QE code suite. Use of a fictitious dielectric constant $\varepsilon_\infty > 1$ softens the repulsion in the electrostatic potential for the HOMO-level trapping. For sufficiently large ε_∞ values, we reduce the spurious quantum-confinements effects [89] and can thus obtain a SIE-robust G21EA and WATER27 assessment that works at general unit-cell sizes.

Figure 12 shows the procedure used to assess the OH electron affinity (as described for the WATER27 setup) for both CX (left panel) and AHBR (right panel). Noting that convergence of the neutral OH system is always robust, it is a simple process to converge these characterizations to actual WATER27 assessments. For the G21EA set, we use this procedure on all of the individual electron-affinity problems. The set of larger dots in Fig. 12 show actual calculations obtained (at CX and AHBR) at varying ε_∞ values together with fitted approximations (dashed curves). We use those to extrapolate the electron-affinity descriptions to the $\varepsilon_\infty \to 1$ results that we actually need for benchmarking. Comparing those limit values to reference data [69] gives us a well-defined assessment of SIEs in WATER27 and G21EA for all types of XC functionals.

[1] Y. Andersson, D. C. Langreth, and B. I. Lundqvist, *van der Waals Interactions in Density-Functional Theory*, Phys. Rev. Lett. **76**, 102 (1996).

[2] J. F. Dobson and B. P. Dinte, *Constraint Satisfaction in Local and Gradient Susceptibility Approximations: Application to a van der Waals Density Functional*, Phys. Rev. Lett. **76**, 1780 (1996).

[3] H. Rydberg, B. I. Lundqvist, D. C. Langreth, and M. Dion, *Tractable Nonlocal Correlation Density Functionals for Flat Surfaces and Slabs*, Phys. Rev. B **62**, 6997 (2000).

[4] H. Rydberg, M. Dion, N. Jacobson, E. Schröder, P. Hyldgaard, S. I. Simak, D. C. Langreth, and B. I. Lundqvist, *van der Waals Density Functional for Layered Structures*, Phys. Rev. Lett. **91**, 126402 (2003).

[5] M. Dion, H. Rydberg, E. Schröder, D. C. Langreth, and B. I. Lundqvist, *van der Waals Density Functional for General Geometries*, Phys. Rev. Lett. **92**, 246401 (2004).

[6] M. Dion, H. Rydberg, E. Schröder, D. C. Langreth, and B. I. Lundqvist, *van der Waals Density Functional for General Geometries*, Phys. Rev. Lett. **92**, 246401 (2004); **95**, 109902(E) (2005).

[7] T. Thonhauser, V. R. Cooper, S. Li, A. Puzder, P. Hyldgaard, and D. C. Langreth, *van der Waals Density Functional: Self-Consistent Potential and the Nature of the van der Waals Bond*, Phys. Rev. B **76**, 125112 (2007).

[8] K. Lee, È. D. Murray, L. Kong, B. I. Lundqvist, and D. C. Langreth, *Higher-Accuracy van der Waals Density Functional*, Phys. Rev. B **82**, 081101(R) (2010).

[9] P. Hyldgaard, K. Berland, and E. Schröder, *Interpretation of van der Waals Density Functionals*, Phys. Rev. B **90**, 075148 (2014).

[10] K. Berland and P. Hyldgaard, *Exchange Functional that Tests the Robustness of the Plasmon Description of the van der Waals Density Functional*, Phys. Rev. B **89**, 035412 (2014).

[11] K. Berland, C. A. Arter, V. R. Cooper, K. Lee, B. I. Lundqvist, E. Schröder, T. Thonhauser, and P. Hyldgaard, *van der Waals Density Functionals Built upon the Electron-Gas Tradition: Facing the Challenge of Competing Interactions*, J. Chem. Phys. **140**, 18A539 (2014).

[12] K. Berland, V. R. Cooper, K. Lee, E. Schröder, T. Thonhauser, P. Hyldgaard, and B. I. Lundqvist, *van der Waals Forces in Density Functional Theory: A Review of the vdW-DF Method*, Rep. Prog. Phys. **78**, 066501 (2015).

[13] T. Thonhauser, S. Zuluaga, C. A. Arter, K. Berland, E. Schröder, and P. Hyldgaard, *Spin Signature of Nonlocal Correlation Binding in Metal-Organic Frameworks*, Phys. Rev. Lett. **115**, 136402 (2015).

[14] K. Berland, Y. Jiao, J.-H. Lee, T. Rangel, J. B. Neaton, and P. Hyldgaard, *Assessment of Two Hybrid van der Waals Density Functionals for Covalent and Noncovalent Binding of Molecules*, J. Chem. Phys. **146**, 234106 (2017).

[15] Y. Jiao, E. Schröder, and P. Hyldgaard, *Extent of Fock-Exchange Mixing for a Hybrid van der Waals Density Functional?*, J. Chem. Phys. **148**, 194115 (2018).

[16] D. Chakraborty, K. Berland, and T. Thonhauser, *Next-Generation Nonlocal van der Waals Density Functional*, J. Chem. Theory Comput. **16**, 5893 (2020).

[17] V. Shukla, Y. Jiao, C. M. Frostenson, and P. Hyldgaard, *vdW-DF-ahcx: A Range-Separated van der Waals Density Functional Hybrid*, J. Phys. Condens. Matter **34**, 025902 (2022).

[18] C. M. Frostenson, E. J. Granhed, V. Shukla, P. A. T. Olsson, E. Schröder, and P. Hyldgaard, *Hard and Soft Materials: Putting Consistent van der Waals Density Functionals to Work*, Electronic Struct. Magn. Inorg. Comp. **4**, 014001 (2022).

[19] B. I. Lundqvist, A. Bogicevic, K. Carling, S. V. Dudiy, S. Gao, J. Hartford, P. Hyldgaard, N. Jacobson, D. C. Langreth, N. Lorente, S. Ovesson, B. Razaznejad, C. Ruberto, H. Rydberg, E. Schröder, S. I. Simak, G. Wahnström, and Y. Yourdshahyan, *Density-Functional Bridge between Surfaces and Interfaces*, Surf. Sci. **493**, 253 (2001).

[20] H. Rydberg, N. Jacobson, P. Hyldgaard, S. I. Simak, B. I. Lundqvist, and D. C. Langreth, *Hard Numbers on Soft Matter*, Surf. Sci. **532–535**, 606 (2003).

[21] J. Kleis, P. Hyldgaard, and E. Schröder, *van der Waals Interaction of Parallel Polymers and Nanotubes*, Comput. Mater. Sci. **33**, 192 (2005).

[22] J. Kleis and E. Schröder, *van der Waals Interaction of Simple, Parallel Polymers*, J. Chem. Phys. **122**, 164902 (2005).

[23] J. Kleis, B. I. Lundqvist, D. C. Langreth, and E. Schröder, *Towards a Working Density-Functional Theory for Polymers: First-Principles Determination of the Polyethylene Crystal Structure*, Phys. Rev. B **76**, 100201(R) (2007).

[24] J. Kleis, E. Schröder, and P. Hyldgaard, *Nature and Strength of Bonding in a Crystal of Semiconducting Nanotubes: van der Waals Density Functional Calculations and Analytical Results*, Phys. Rev. B **77**, 205422 (2008).

[25] J. Hooper, V. R. Cooper, T. Thonhauser, N. A. Romero, F. Zerilli, and D. C. Langreth, *Predicting $C-H/\pi$ Interactions with Nonlocal Density Functional Theory*, ChemPhysChem **9**, 891 (2008).

[26] V. R. Cooper, T. Thonhauser, A. Puzder, E. Schröder, B. I. Lundqvist, and D. C. Langreth, *Stacking Interactions and the Twist of DNA*, J. Am. Chem. Soc. **130**, 1304 (2008).

[27] V. R. Cooper, T. Thonhauser, and D. C. Langreth, *An Application of the van der Waals Density Functional: Hydrogen Bonding and Stacking Interactions between Nucleobases*, J. Chem. Phys. **128**, 204102 (2008).

[28] S. D. Chakarova-Käck, E. Schröder, B. I. Lundqvist, and D. C. Langreth, *Application of van der Waals Density Functional to an Extended System: Adsorption of Benzene and Naphthalene on Graphite*, Phys. Rev. Lett. **96**, 146107 (2006).

[29] S. D. Chakarova-Käck, Ø. Borck, E. Schröder, and B. I. Lundqvist, *Adsorption of Phenol on Graphite (0001) and α-Al_2O_3 (0001): Nature of van der Waals Bonds from First-Principles Calculations*, Phys. Rev. B **74**, 155402 (2006).

[30] S. D. Chakarova-Käck, A. Vojvodic, J. Kleis, P. Hyldgaard, and E. Schröder, *Binding of Polycyclic Aromatic Hydrocarbons and Graphene Dimers in Density Functional Theory*, New J. Phys. **12**, 013017 (2010).

[31] S. Grimme, *Accurate Description of van der Waals Complexes by Density Functional Theory Including Empirical Corrections*, J. Comput. Chem. **25**, 1463 (2004).

[32] A. D. Becke and E. R. Johnson, *A Density-Functional Model of the Dispersion Interaction*, J. Chem. Phys. **123**, 154101 (2005).

[33] A. D. Becke and E. R. Johnson, *Exchange-Hole Dipole Moment and the Dispersion Interaction Revisited*, J. Chem. Phys. **127**, 154108 (2007).

[34] S. Grimme, *Semiempirical Hybrid Density Functional with Perturbative Second-Order Correlation*, J. Chem. Phys. **124**, 034108 (2006).

[35] P. L. Silvestrelli, *van der Waals Interactions in DFT Made Easy by Wannier Functions*, Phys. Rev. Lett. **100**, 053002 (2008).

[36] A. Tkatchenko and M. Scheffler, *Accurate Molecular van der Waals Interactions from Ground-State Electron Density and Free-Atom Reference Data*, Phys. Rev. Lett. **102**, 073005 (2009).

[37] V. G. Ruiz, W. Liu, E. Zojer, M. Scheffler, and A. Tkatchenko, *Density-Functional Theory with Screened van der Waals Interactions for the Modeling of Hybrid Inorganic-Organic Systems*, Phys. Rev. Lett. **108**, 146103 (2012).

[38] A. Tkatchenko, R. A. DiStasio, R. Car, and M. Scheffler, *Accurate and Efficient Method for Many-Body van der Waals Interactions*, Phys. Rev. Lett. **108**, 236402 (2012).

[39] A. Ambrosetti and P. L. Silvestrelli, *van der Waals Interactions in Density Functional Theory Using Wannier Functions: Improved C_6 and C_3 Coefficients by a Different Approach*, Phys. Rev. B **85**, 073101 (2012).

[40] E. Caldeweyher, S. Ehlert, A. Hansen, H. Neugebauer, S. Spicher, C. Bannwarth, and S. A. Grimme, *A Generally Applicable Atomic-Charge Dependent London Dispersion Correction*, J. Chem. Phys. **150**, 154122 (2019).

[41] M. Kim, W. J. Kim, T. Gould, E. K. Lee, S. Lebeque, and H. Kim, *uMBD: A Materials-Ready Dispersion Correction that Uniformly Treats Metallic, Ionic, and van der Waals Bonding*, J. Am. Chem. Soc. **142**, 2346 (2020).

[42] Y. Jiao, E. Schröder, and P. Hyldgaard, *Signatures of van der Waals Binding: A Coupling-Constant Scaling Analysis*, Phys. Rev. B **97**, 085115 (2018).

[43] P. Hyldgaard, Y. Jiao, and V. Shukla, *Screening Nature of the van der Waals Density Functional Method: A Review*

and Analysis of the Many-Body Physics Foundation, J. Phys. Condens. Matter **32,** 393001 (2020).

[44] J.-H. Lee, P. Hyldgaard, and J. B. Neaton, *An Assessment of Density Functionals for Predicting* CO_2 *Adsorption in Diamine-Functionalized Metal-Organic Frameworks*, J. Chem. Phys. **156,** 154113 (2022).

[45] K. Rapcewicz and N. W. Ashcroft, *Fluctuation Attraction in Condensed Matter: A Nonlocal Functional Approach*, Phys. Rev. B **44,** 4032 (1991).

[46] D. C. Langreth and S. H. Vosko, *Exact Electron-Gas Response Functions at High Density*, Phys. Rev. Lett. **59,** 497 (1987).

[47] L. Hedin and B. I. Lundqvist, *Explicit Local Exchange-Correlation Potentials*, J. Phys. C **4,** 2064 (1971).

[48] O. Gunnarsson and B. I. Lundqvist, *Exchange and Correlation in Atoms, Molecules, and Solids by the Spin-Density-Functional Formalism*, Phys. Rev. B **13,** 4274 (1976).

[49] J. P. Perdew and Y. Wang, *Pair-Distribution Function and Its Coupling-Constant Average for the Spin-Polarized Electron Gas*, Phys. Rev. B **46,** 12947 (1992).

[50] J. P. Perdew, K. Burke, and M. Ernzerhof, *Generalized Gradient Approximation Made Simple*, Phys. Rev. Lett. **77,** 3865 (1996).

[51] J. P. Perdew, A. Ruzsinszky, G. I. Csonka, O. A. Vydrov, G. E. Scuseria, L. A. Constantin, X. Zhou, and K. Burke, *Restoring the Density-Gradient Expansion for Exchange in Solids and Surfaces*, Phys. Rev. Lett. **100,** 136406 (2008).

[52] J. Sun, A. Ruzsinszky, and J. P. Perdew, *Strongly Constrained and Appropriately Normed Semilocal Density Functional*, Phys. Rev. Lett. **115,** 036402 (2015).

[53] H. Peng, Z.-H. Yang, J. P. Perdew, and J. Sun, *Versatile van der Waals Density Functional Based on a Meta-Generalized Gradient Approximation*, Phys. Rev. X **6,** 041005 (2016).

[54] D. C. Langreth and J. P. Perdew, *The Gradient Approximation to the Exchange-Correlation Energy Functional: A Generalization that Works*, Solid State Commun. **31,** 567 (1979).

[55] F. Tran, L. Kalantari, B. Traoré, X. Rocquefelte, and P. Blaha, *Nonlocal van der Waals Functionals for Solids: Choosing an Appropriate One*, Phys. Rev. Mater. **3,** 063602 (2019).

[56] I. Hamada, *van der Waals Density Functional Made Accurate*, Phys. Rev. B **89,** 121103(R) (2014).

[57] J. Klimeš, D. R. Bowler, and A. Michaelides, *Chemical Accuracy for the van der Waals Density Functional*, J. Phys. Condens. Matter **22,** 022201 (2010).

[58] O. A. Vydrov and T. Van Voorhis, *Nonlocal van der Waals Density Functional: The Simpler the Better*, J. Chem. Phys. **133,** 244103 (2010).

[59] V. R. Cooper, *van der Waals Density Functional: An Appropriate Exchange Functional*, Phys. Rev. B **81,** 161104(R) (2010).

[60] J. Klimeš, D. R. Bowler, and A. Michaelides, *van der Waals Density Functionals Applied to Solids*, Phys. Rev. B **83,** 195131 (2011).

[61] R. Sabatini, T. Gorni, and S. de Gironcoli, *Nonlocal van der Waals Density Functional Made Simple and Efficient*, Phys. Rev. B **87,** 041108(R) (2013).

[62] See Supplemental Material at http://link.aps.org/supplemental/10.1103/PhysRevX.12.041003 for a list of functional abbreviations or short hands and for figures and tables summarizing functional-performance comparisons as asserted on molecular and bulk benchmark sets.

[63] J. Harris, *Simplified Method for Calculating the Energy of Weakly Interacting Fragments*, Phys. Rev. B **31,** 1770 (1985).

[64] É. D. Murray, K. Lee, and D. C. Langreth, *Investigation of Exchange Energy Density Functional Accuracy for Interacting Molecules*, J. Chem. Theory Comput. **5,** 2754 (2009).

[65] A. D. Becke, *Perspective: Fifty Years of Density-Functional Theory in Chemical Physics*, J. Chem. Phys. **140,** 18A301 (2014).

[66] K. Burke, *Perspective on Density Functional Theory*, J. Chem. Phys. **136,** 150901 (2012).

[67] J. A. Pople, M. Head-Gordon, D. J. Fox, K. Raghavachari, and L. A. Curtiss, *Gaussian-1 Theory: A General Procedure for Prediction of Molecular Energies*, J. Chem. Phys. **90,** 5622 (1989).

[68] L. Goerigk and S. Grimme, *A General Database for Main Group Thermochemistry, Kinetics, and Noncovalent Interactions—Assessment of Common and Reparameterized (Meta-)GGA Density Functionals*, J. Chem. Theory Comput. **6,** 107 (2010).

[69] L. Goerigk, A. Hansen, C. Bayer, S. Ehrlich, A. Najibi, and S. Grimme, *A Look at the Density Functional Theory Zoo with the Advanced GMTKN55 Database for General Main Group Thermochemistry, Kinetics and Noncovalent Interactions*, Phys. Chem. Chem. Phys. **19,** 32184 (2017).

[70] N. Rosi, J. Eckert, M. Eddaoudi, D. Vodak, J. Kim, M. O'Keeffe, and O. Yaghi, *Hydrogen Storage in Microporous Metal-Organic Frameworks*, Science **300,** 1127 (2003).

[71] D. C. Langreth, B. I. Lundqvist, S. D. Chakarova-Käck, V. R. Cooper, M. Dion, P. Hyldgaard, A. Kelkkanen, J. Kleis, L. Kong, S. Li, P. G. Moses, E. Murray, A. Puzder, H. Rydberg, E. Schröder, and T. Thonhauser, *A Density Functional for Sparse Matter*, J. Phys. Condens. Matter **21,** 084203 (2009).

[72] L. Kong, V. R. Cooper, N. Nijem, K. Li, J. Li, Y. J. Chabal, and D. C. Langreth, *Theoretical and Experimental Analysis of* H_2 *Binding in a Prototypical Metal-Organic Framework Material*, Phys. Rev. B **79,** 081407(R) (2009).

[73] Q. Li and T. Thonhauser, *A Theoretical Study of the Hydrogen-Storage Potential of* $(H_2)_4CH_4$ *in Metal Organic Framework Materials and Carbon Nanotubes*, J. Phys. Condens. Matter **24,** 424204 (2012).

[74] V. R. Cooper, Y. Ihm, and J. R. Morris, *Hydrogen Adsorption at the Graphene Surface: A vdW-DF Perspective*, Phys. Procedia **34,** 34 (2012).

[75] A. R. Millward and O. M. Yaghi, *Metal-Organic Frameworks with Exceptionally High Capacity for Storage of Carbon Dioxide at Room Temperature*, J. Am. Chem. Soc. **127,** 17998 (2005).

[76] T. M. McDonald, W. Lee, J. A. Mason, B. M. Wiers, C. S. Hong, and J. R. Long, *Capture of Carbon Dioxide from Air and Flue Gas in the Alkylamine-Appended Metal-Organic Framework* mmen-Mg_2(dobpdc), J. Am. Chem. Soc. **134,** 7056 (2012).

[77] T.-H. Bae and J. R. Long, CO_2/N_2 Separations with Mixed-Matrix Membranes Containing Mg_2(dobdc) Nanocrystals, Energy Environ. Sci. **6**, 3565 (2013).

[78] T. M. McDonald et al., Cooperative Insertion of CO_2 in Diamine-Appended Metal-Organic Frameworks, Nature (London) **519**, 303 (2015).

[79] S. Zuluaga, P. Canepa, K. Tan, Y. J. Chabal, and T. Thonhauser, Study of van der Waals Bonding and Interactions in Metal Organic Framework Materials, J. Phys. Condens. Matter **26**, 133002 (2014).

[80] R. Poloni, K. Lee, R. F. Berger, B. Smit, and J. B. Neaton, Understanding Trends in CO_2 Adsorption in Metal Organic Frameworks with Open-Metal Sites, J. Phys. Chem. Lett. **5**, 861 (2014).

[81] W. L. Queen, M. R. Hudson, E. D. Bloch, J. A. Mason, M. I. Gonzalez, J. S. Lee, D. Gygi, J. D. Howe, K. Lee, T. A. Darwish, M. James, V. K. Peterson, S. J. Teat, B. Smit, J. B. Neaton, J. R. Long, and C. M. Brown, Comprehensive Study of Carbon Dioxide Adsorption in the Metal-Organic Frameworks $M2$(dobdc) (M = Mg, Mn, Fe, Co, Ni, Cu, Zn), Chem. Sci. **5**, 4569 (2014).

[82] E. Lee and K. A. Persson, Li Absorption and Intercalation in Single Layer Graphene and Few Layer Graphene by First Principles, Nano Lett. **12**, 4624 (2012).

[83] K. Persson, Y. Hinuma, Y. S. Meng, A. Van der Ven, and G. Ceder, Thermodynamic and Kinetic Properties of the Li-Graphite System from First-Principles Calculations, Phys. Rev. B **82**, 125416 (2010).

[84] V. Shukla, N. K. Jena, S. R. Naqvi, W. Luo, and R. Ahuja, Modelling High-Performing Batteries with MXenes: The Case of S-Functionalized Two-Dimensional Nitride MXene Electrode, Nano Energy **58**, 877 (2019).

[85] V. Shukla, R. B. Araujo, N. K. Jena, and R. Ahuja, Borophene's Tryst with Stability: Exploring 2D Hydrogen Boride as an Electrode for Rechargeable Batteries, Phys. Chem. Chem. Phys. **20**, 22008 (2018).

[86] D. Le, A. Kara, E. Schröder, P. Hyldgaard, and T. S. Rahman, Physisorption of Nucleobases on Graphene: A Comparative van der Waals Study, J. Phys. Condens. Matter **24**, 424210 (2012).

[87] S. Umrao, A. Maurya, V. Shukla, A. Grigoriev, R. Ahuja, M. Vinayak, R. Srivastava, P. Saxena, I.-K. Oh, and A. Srivastava, Anticarcinogenic Activity of Blue Fluorescent Hexagonal Boron Nitride Quantum Dots: As an Effective Enhancer for DNA Cleavage Activity of Anticancer Drug Doxorubicin, Mater. Today Bio **1**, 100001 (2019).

[88] K. Berland and P. Hyldgaard, Analysis of van der Waals Density Functional Components: Binding and Corrugation of Benzene and C_{60} on Boron Nitride and Graphene, Phys. Rev. B **87**, 205421 (2013).

[89] D. Lee, F. Furche, and K. Burke, Accuracy of Electron Affinities of Atoms in Approximate Density Functional Theory, J. Phys. Chem. Lett. **1**, 2124 (2010).

[90] S. Song, S. Vuckovic, E. Sim, and K. Burke, Density-Corrected DFT Explained: Questions and Answers, J. Chem. Theory Comput. **18**, 817 (2022).

[91] T. M. Henderson, B. G. Janesko, and G. E. Scusseria, Generalized Gradient Approximation Model Exchange Holes for Range-Separated Hybrids, J. Chem. Phys. **128**, 194105 (2008).

[92] A. Patra, H. Peng, J. Sun, and J. P. Perdew, Rethinking CO Adsorption on Transition-Metal Surfaces: Effect of Density-Driven Self-Interaction Errors, Phys. Rev. B **100**, 035442 (2019).

[93] J. Heyd, G. E. Scuseria, and M. Ernzerhof, Hybrid Functionals Based on a Screened Coulomb Potential, J. Chem. Phys. **118**, 8207 (2003).

[94] J. Heyd, G. E. Scuseria, and M. Ernzerhof, Hybrid Functionals Based on a Screened Coulomb Potential, J. Chem. Phys. **118**, 8207 (2003); **124**, 219906(E) (2006).

[95] S. Grimme, J. Antony, S. Ehrlich, and H. Krieg, A Consistent and Accurate Ab Initio Parametrization of Density Functional Dispersion correction (DFT-D) for the 94 Elements H–Pu, J. Chem. Phys. **132**, 154104 (2010).

[96] A. D. Becke, Density-Functional Thermochemistry. III. The Role of Exact Exchange, J. Chem. Phys. **98**, 5648 (1993).

[97] C. Lee, W. Yang, and R. G. Parr, Development of the Coll-Salvetti Correlation-Energy Formula into a Functional of the Electron Density, Phys. Rev. B **37**, 785 (1988).

[98] S. Seyedraoufi and K. Berland, Improved Proton-Transfer Barriers with van der Waals Density Functionals: Role of Repulsive Non-Local Correlation, J. Chem. Phys. **156**, 244106 (2022).

[99] D. C. Langreth and J. P. Perdew, The Exchange-Correlation Energy of a Metallic Surface, Solid State Commun. **17**, 1425 (1975).

[100] D. C. Langreth and J. P. Perdew, Exchange-Correlation Energy of a Metallic Surface: Wave-Vector Analysis, Phys. Rev. B **15**, 2884 (1977).

[101] D. C. Langreth and J. P. Perdew, Theory of Nonuniform Electronic Systems. I. Analysis of the Gradient Approximation and a Generalization that Works, Phys. Rev. B **21**, 5469 (1980).

[102] D. C. Langreth and M. J. Mehl, Easily Implementable Nonlocal Exchange-Correlation Energy Functional, Phys. Rev. Lett. **47**, 446 (1981).

[103] D. C. Langreth and S. H. Vosko, Response Functions and Non-Local Functionals, Adv. Quantum Chem. **21**, 175 (1990).

[104] Here and below, we suppress the double spatial coordinates of this nonlocal function for brevity.

[105] A. C. Maggs and N. W. Ashcroft, Electronic Fluctuation and Cohesion in Metals, Phys. Rev. Lett. **59**, 113 (1987).

[106] S. Ma and K. Brueckner, Correlation Energy of an Electron Gas with a Slowly Varying High Density, Phys. Rev. **165**, 18 (1968).

[107] M. Rasolt and D. J. W. Geldart, Gradient Corrections in the Exchange and Correlation Energy of an Inhomogeneous Electron Gas, Phys. Rev. Lett. **35**, 1234 (1975).

[108] O. Gunnarsson, M. Jonson, and B. I. Lundqvist, Descriptions of Exchange and Correlation Effects in Inhomogeneous Electron Systems, Phys. Rev. B **20**, 3136 (1979).

[109] B. I. Lundqvist, Single-Particle Spectrum of Degenerate Electron Gas. I. Structure of Spectral Weight Function, Phys. Kondens. Mater. **6**, 193 (1967).

[110] J. P. Perdew and Y. Wang, Accurate and Simple Density Functional for the Electronic Exchange Energy: Generalized Gradient Approximation, Phys. Rev. B **33**, 8800 (1986).

[111] A. Pribram-Jones, D. A. Gross, and K. Burke, *DFT: A Theory Full of Holes*, Annu. Rev. Phys. Chem. **66**, 283 (2015).

[112] F. London, *Zur Theorie und Systematik der Molekularkräfte*, Z. Phys. **63**, 245 (1930).

[113] G. D. Mahan, *van der Waals Forces in Solids*, J. Chem. Phys. **43**, 1569 (1965).

[114] D. C. Langreth, M. Dion, H. Rydberg, E. Schröder, P. Hyldgaard, and B. I. Lundqvist, *van der Waals Density Functional Theory with Applications*, Int. J. Quantum Chem. **101**, 599 (2005).

[115] K. Berland, *Connected by Voids: Interactions and Screening in Sparse Matter*, Ph.D. thesis, Chalmers University of Technology, 2012.

[116] F. London, *The General Theory of Molecular Forces*, Z. Phys. Chem. **33**, 8 (1937) [English translations, H. Hettema, *Quantum Chemistry, Classic Scientific Papers* (World Scientific, Singapore, 2000) and F. London, Trans. Faraday Soc. **33**, 8b (1937)].

[117] H. Rydberg, *Nonlocal Correlations in Density Functional Theory*, Ph.D. thesis, Chalmers University of Technology, 2001.

[118] M. Dion, *van der Waals Forces in Density Functional Theory*, Ph.D. thesis, Rutgers University, 2004.

[119] D. C. Langreth, *Singularities in the X-Ray Spectra of Metals*, Phys. Rev. B **1**, 471 (1970).

[120] L. Hedin, *Effects of Recoil on Shake-Up Spectra in Metals*, Phys. Scr. **21**, 477 (1980).

[121] O. Gunnarsson, V. Meden, and K. Schönhammer, *Corrections to Migdal's Theorem for Spectral Functions: A Cumulant Treatment of the Time-Dependent Green's Function*, Phys. Rev. B **50**, 10462 (1994).

[122] B. Holm and F. Aryasetiawan, *Self-Consistent Cumulant Expansion for the Electron Gas*, Phys. Rev. B **56**, 12825 (1997).

[123] A. Y. Sokolov, A. C. Simmonett, and H. F. Schaefer III, *Density Cumulant Functional Theory: The DC-12 Method, an Improved Description of the One-Particle Density Matrix*, J. Chem. Phys. **138**, 024107 (2013).

[124] G. Román-Pérez and J. M. Soler, *Efficient Implementation of a van der Waals Density Functional: Application to Double-Wall Carbon Nanotubes*, Phys. Rev. Lett. **103**, 096102 (2009).

[125] A. Hjorth Larsen, M. Kuisma, J. Löfgren, Y. Pouillon, P. Erhart, and P. Hyldgaard, LIBVDWXC: *A Library for Exchange-Correlation Functionals in the vdW-DF Family*, Model. Simul. Mater. Sci. Eng. **25**, 065004 (2017).

[126] E. J. Granhed, G. Wahnström, and P. Hyldgaard, $BaZrO_3$ *Stability under Pressure: The Role of Non-Local Exchange and Correlation*, Phys. Rev. B **101**, 224105 (2020).

[127] J. Schwinger, *Thomas-Fermi Model: The Second Correction*, Phys. Rev. A **24**, 2353 (1981).

[128] J. P. Perdew, K. Burke, and Y. Wang, *Generalized Gradient Approximation for the Exchange-Correlation Hole of a Many-Electron System*, Phys. Rev. B **54**, 16533 (1996).

[129] We see the vdW attraction as arising from electrodynamic coupling among electron-XC-hole pairs [9,12,43,45,46,116]. The nonlocal-correlation component E_c^{NL} must therefore vanish if we can suppress the electron charge. Meanwhile, the vdW-DF method has no auxiliary inputs, so it follows from a simple coupling-constant scaling argument that the exchange-energy component must exactly equal this vanishing-electron-charge limit of the vdW-DF E_{XC} [42,130].

[130] K. Burke, M. Ernzerhof, and J. P. Perdew, *The Adiabatic Connection Method: A Non-Empirical Hybrid*, Chem. Phys. Lett. **265**, 115 (1997).

[131] A. D. Becke, *Density-Functional Exchange-Energy Approximation with Correct Asymptotic Behavior*, Phys. Rev. A **38**, 3098 (1988).

[132] P. Elliott and K. Burke, *Non-Empirical Derivation of the Parameter in the B88 Exchange Functional*, Can. J. Chem. **87**, 1485 (2009).

[133] K. Burke and L. O. Wagner, *DFT in a Nutshell*, Int. J. Quantum Chem. **113**, 96 (2013).

[134] E. H. Lieb and S. Oxford, *Strongly Constrained and Appropriately Normed Semilocal Density Functional*, Int. J. Quantum Chem. **19**, 427 (1981).

[135] J. P. Perdew, A. Ruzsinszky, J. Sun, and K. Burke, *Gedanken Densities and Exact Constraints in Density Functional Theory*, J. Chem. Phys. **140**, 18A533 (2014).

[136] Y. Zhang and W. Yang, *Comment on Generalized Gradient Approximation Made Simple*, Phys. Rev. Lett. **80**, 890 (1998).

[137] J. M. Luttinger and J. C. Ward, *Ground-State Energy of a Many-Fermion System. II*, Phys. Rev. **118**, 1417 (1960).

[138] L. J. Sham and M. Schlüter, *Density-Functional Theory of the Energy Gap*, Phys. Rev. Lett. **51**, 1888 (1983).

[139] T. Jenkins, K. Berland, and T. Thonhauser, *Reduced-Gradient Analysis of vdW Complexes*, Electron. Struct. Magn. Inorg. Comp. **3**, 034009 (2021).

[140] A. Meier de Andrade, J. Kullgren, and P. Broqvist, *Quantitative and Qualitative Performance of Density Functional Theory Rationalized by Reduced Density Gradient Distributions*, Phys. Rev. B **102**, 075115 (2020).

[141] T. Rangel, K. Berland, S. Sharifzadeh, F. Brown-Altvater, K. Lee, P. Hyldgaard, L. Kronik, and J. B. Neaton, *Structural and Excited-State Properties of Oligoacene Crystals from First Principles*, Phys. Rev. B **93**, 115206 (2016).

[142] F. Brown-Altvater, T. Rangel, and J. B. Neaton, *Ab initio Phonon Dispersion in Crystalline Naphthalene Using van der Waals Density Functionals*, Phys. Rev. B **93**, 195206 (2016).

[143] S. Song, A. Song, S. Vuckovic, and K. Burke, *Improving Results by Improving Densities: Density-Corrected Density Functional Theory*, J. Am. Chem. Soc. **144**, 6625 (2022).

[144] J. Wellendorff, K. T. Lundgaard, A. Møgelhøj, V. Petzold, D. D. Landis, J. K. Nørskov, T. Bligaard, and K. W. Jacobsen, *Density Functionals for Surface Science: Exchange-Correlation Model Development with Bayesian Error Estimation*, Phys. Rev. B **85**, 235149 (2012).

[145] J. Klimeš and A. Michaelides, *Perspective: Advances and Challenges in Treating van der Waals Dispersion Forces in Density Functional Theory*, J. Chem. Phys. **137**, 120901 (2012).

[146] O. T. Hofmann, E. Zojer, L. Hörmann, A. Jeindl, and R. J. Maurer, *First-Principles Calculations of Hybrid*

Inorganic-Organic Interfaces: From State-of-the-Art to Best Practice, Phys. Chem. Chem. Phys. **23**, 8132 (2021).

[147] R. Sabatini, E. Küçükbenli, B. Kolb, T. Thonhauser, and S. de Gironcoli, *Structural Evolution of Amino Acid Crystals under Stress from a Non-Empirical Density Functional*, J. Phys. Condens. Matter **24**, 424209 (2012).

[148] A. D. Becke, *On the Large-Gradient Behavior of the Density Functional Exchange Energy*, J. Chem. Phys. **85**, 7184 (1986).

[149] P. R. Antoniewicz and L. Kleinman, *Kohn-Sham Exchange Potential Exact to First Order in $\rho(K)/\rho_0$*, Phys. Rev. B **31**, 6779 (1985).

[150] L. Kleinman and S. Lee, *Gradient Expansion of the Exchange-Energy Density Functional: Effect of Taking Limits in the Wrong Order*, Phys. Rev. B **37**, 4634 (1988).

[151] K. Burke, M. Ernzerhof, and J. P. Perdew, *The Adiabatic Connection Method: A Non-Empirical Hybrid*, Chem. Phys. Lett. **265**, 115 (1997).

[152] C. Adamo and V. Barone, *Towards Reliable Density Functional Methods without Adjustable Parameters: The PBE0 Model*, J. Chem. Phys. **110**, 6158 (1999).

[153] P. Giannozzi *et al.*, QUANTUM ESPRESSO: *A Modular and Open-Source Software Project for Quantum Simulations of Materials*, J. Phys. Condens. Matter **21**, 395502 (2009).

[154] P. Giannozzi *et al.*, *Advanced Capabilities for Materials Modelling with* QUANTUM ESPRESSO, J. Phys. Condens. Matter **29**, 465901 (2017).

[155] I. Carnimeo, S. Baroni, and P. Giannozzi, *Fast Hybrid Density-Functional Computations Using Plane-Wave Basis Sets*, Electron. Struct. Magn. Inorg. Comp. **1**, 015009 (2019).

[156] The DF2-BR0 performance on the 55 specific benchmarks is, in almost all cases, as good as or better than that for CX0 or for CX0P (and they are already strong overall performers) as shown in the Supplemental Material [62]. The W4-11 benchmark set (and, to a lesser extent, the DIPCS10 and MB16-43 sets) forms an exception to this general observation.

[157] M. Ernzerhof and J. P. Perdew, *Generalized Gradient Approximation to the Angle- and System-Averaged Exchange Hole*, J. Chem. Phys. **109**, 3313 (1998).

[158] S. Refaely-Abramson, S. Sharifzadeh, N. Govind, J. Autschbach, J. B. Neaton, R. Baer, and L. Kronik, *Quasiparticle Spectra from a Nonempirical Optimally Tuned Range-Separated Hybrid Density Functional*, Phys. Rev. Lett. **109**, 226405 (2012).

[159] M. Wijzenbroek, D. M. Klein, B. Smits, M. F. Somers, and G.-J. Kroes, *Performance of a Non-Local van der Waals Density Functional on the Dissociation of* H_2 *on Metal Surfaces*, J. Phys. Chem. A **119**, 12146 (2015).

[160] J. P. Perdew, R. G. Parr, M. Levy, and J. J. L. Balduz, *Density-Functional Theory for Fractional Particle Number: Derivative Discontinuities of the Energy*, Phys. Rev. Lett. **49**, 1691 (1982).

[161] A. Seidl, A. Görling, P. Vogl, J. A. Majewski, and M. Levy, *Generalized Kohn-Sham Schemes and the Band-Gap Problem*, Phys. Rev. B **53**, 3764 (1996).

[162] E. Kraisler and L. Kronik, *Piecewise Linearity of Approximate Density Functionals Revisited: Implications for Frontier Orbital Energies*, Phys. Rev. Lett. **110**, 126403 (2013).

[163] S. Refaely-Abramson, S. Sharifzadeh, M. Jain, R. Baer, J. B. Neaton, and L. Kronik, *Gab Renormalization of Molecular Crystals from Density Functional Theory*, Phys. Rev. B **88**, 081204(R) (2013).

[164] Z.-F. Liu, D. A. Egger, S. Refaely-Abramson, L. Kronik, and J. B. Neaton, *Energy Level Alignment at Molecule-Metal Interfaces from an Optimally Tuned Range-Separated Hybrid Functional*, J. Chem. Phys. **146**, 092326 (2017).

[165] D. Wing, G. Ohad, J. B. Haber, M. R. Filip, S. E. Gant, J. B. Neaton, and L. Kronik, *Band Gaps of Crystalline Solids from Wannier-Localization-Based Optimal Tuning of a Screened Range-Separated Hybrid Functional*, Proc. Natl. Acad. Sci. U.S.A. **118**, e2104556118 (2021).

[166] J. H. Skone, M. Govoni, and G. Galli, *Self-Consistent Hybrid Functional for Condensed Systems*, Phys. Rev. B **89**, 195112 (2014).

[167] J. H. Skone, M. Govoni, and G. Galli, *Nonempirical Range-Separated Hybrid Functionals for Solids and Molecules*, Phys. Rev. B **93**, 235106 (2016).

[168] G. Miceli, W. Chen, I. Reshetnyak, and A. Pasquarello, *Nonempirical Hybrid Functionals for Band Gaps and Polaronic Distortions in Solids*, Phys. Rev. B **97**, 121112(R) (2018).

[169] T. Bischoff, I. Reshetnyak, and A. Pasquarello, *Adjustable Potential Probes for Band-Gap Predictions of Extended Systems through Nonempirical Hybrid Functionals*, Phys. Rev. B **99**, 201114(R) (2019).

[170] T. Bischoff, J. Wiktor, W. Chen, and A. Pasquarello, *Nonempirical Hybrid Functionals for Band Gaps of Inorganic Metal-Halide Perovskites*, Phys. Rev. Mater. **3**, 123802 (2019).

[171] L. Lin, *Adaptively Compressed Exchange Operator*, J. Chem. Theory Comput. **12**, 2242 (2016).

[172] L. Gharaee, P. Erhart, and P. Hyldgaard, *Finite-Temperature Properties of Non-Magnetic Transition Metals: Comparison of the Performance of Constraint-Based Semi and Nonlocal Functionals*, Phys. Rev. B **95**, 085147 (2017).

[173] L. Spanu, S. Sorella, and G. Galli, *Nature and Strength of Interlayer Binding in Graphite*, Phys. Rev. Lett. **103**, 196401 (2009).

[174] P. Ganesh, J. Kim, C. Park, M. Yoon, F. A. Reboredo, and P. R. C. Kent, *Binding and Diffusion of Lithium in Graphite: Quantum Monte Carlo Benchmarks and Validation of van der Waals Density Functional Methods*, J. Chem. Theory Comput. **10**, 5318 (2014).

[175] H. Shin, J. Kim, H. Lee, O. Heinonen, A. Benali, and Y. Kwon, *Nature of Interlayer Binding and Stacking of sp-sp^2 Hybridized Carbon Layers: A Quantum Monte Carlo Study*, J. Chem. Theory Comput. **13**, 5639 (2017).

[176] C.-R. Hsing, C. Chen, J.-P. Chou, C.-M. Chang, and C.-M. Wei, *van der Waals Interaction in a Boron Nitride Bilayer*, New J. Phys. **16**, 113015 (2015).

[177] L. Shulenburger, A. D. Baczewski, Z. Zhu, J. Guan, and D. Tomanek, *The Nature of the Interlayer Interaction in Bulk and Few-Layer Phosphorus*, Nano Lett. **15**, 8170 (2015).

[178] S. Lebégue, J. Harl, T. Gould, J. G. Ángyán, G. Kresse, and J. F. Dobson, *Cohesive Properties and Asymptotics of the Dispersion Interaction in Graphite by the Random Phase Approximation*, Phys. Rev. Lett. **105**, 196401 (2010).

[179] T. Olsen and K. S. Thygesen, *Random Phase Approximation Applied to Solids, Molecules, and Graphene-Metal Interfaces: From van der Waals to Covalent Bonding*, Phys. Rev. B **87**, 075111 (2013).

[180] S. Zhou, J. Han, S. Dai, J. Sun, and D. J. Srolovitz, *van der Waals Bilayer Energetics: Generalized Stacking-Fault Energy of Graphene, Boron Nitride, and Graphene/Boron Nitride Bilayers*, Phys. Rev. B **92**, 155438 (2015).

[181] W. Wang, S. Dai, X. Li, J. Yang, D. J. Srolovitz, and Q. Zheng, *Measurement of the Cleavage Energy in Graphite*, Nat. Commun. **6**, 7853 (2015).

[182] B. Rasche, J. Brunner, T. Schramm, M. P. Ghimire, U. Nitzsche, B. Büchner, R. Giraud, M. Richter, and J. Dufouleur, *Determination of Cleavage Energy and Efficient Nanostructuring of Layered Materials by Atomic Force Microscopy*, Nano Lett. **22**, 3550 (2022).

[183] E. Mostaani, N. D. Drummond, and V. I. Fal'ko, *Quantum Monte Carlo Calculation of the Binding Energy of Bilayer Graphene*, Phys. Rev. Lett. **115**, 115501 (2015).

[184] K. Kusakabe, A. Wake, A. Nagakubo, K. Murashima, M. Murakami, K. Adachi, and H. Ogi, *Interplanar Stiffness in Defect-Free Monocrystalline Graphite*, Phys. Rev. Mater. **4**, 043603 (2020).

[185] Y. X. Zhao and I. L. Spain, *X-Ray Diffraction Data for Graphite to 20 GPa*, Phys. Rev. B **40**, 993 (1989).

[186] O. L. Blakslee, D. G. Proctor, E. J. Seldin, G. B. Spence, and T. Wang, *Elastic Constants of Compression-Annealed Pyrolytic Graphite*, J. Appl. Phys. **41**, 3373 (1970).

[187] A. Bosak, M. Krisch, M. Mohr, J. Maultzsch, and C. Thomsen, *Elasticity of Single-Crystalline Graphite: Inelastic X-Ray Scattering Study*, Phys. Rev. B **75**, 153408 (2007).

[188] P. A. T. Olsson, E. Schröder, P. Hyldgaard, M. Kroon, E. Andreasson, and E. Bergvall, *Ab Initio and Classical Atomistic Modelling of Structure and Defects in Crystalline Orthorhombic Polythylene: Twin Boundaries, Slip Interfaces, and Nature of Barriers*, Polymer **121**, 234 (2017).

[189] P. A. T. Olsson, P. Hyldgaard, E. Schröder, E. P. Jutemar, E. Andreasson, and M. Kroon, *Ab Initio Investigation of Martensitic Transformation in Crystalline Polyethylene*, Phys. Rev. Mater. **2**, 075602 (2018).

[190] T. Björkman, A. Gulans, A. V. Krasheninnikov, and R. M. Nieminen, *van der Waals Bonding in Layered Compounds from Advanced Density-Functional First-Principles Calculations*, Phys. Rev. Lett. **108**, 235502 (2012).

[191] T. Björkman, A. Gulans, A. V. Krasheninnikov, and R. M. Nieminen, *Are We van der Waals Ready?*, J. Phys. Condens. Matter **24**, 424218 (2012).

[192] The AHB21 and BH76 sets also contain the OH^- radical (and the IL16 set contains negatively charged ions), but sitting in benchmark sets that we find can use a small unit cell, the convergence problems do not manifest themselves even in raw QE calculations. We still, in our present GMTKN55 survey, use the electrostatic-environment approach to reliably assert also the performance for the AHB21 benchmark set. However, finding no relevant correction for AHB21 relative to the default brute-force (that is, native or environment-free) QE exploration (within the present selection for unit-cell sizes), we focus the

[193] O. Andreussi, I. Dabo, and N. Marzari, *Revised Self-Consistent Continuum Solvation in Electronic-Structure Calculations*, J. Chem. Phys. **136**, 064102 (2012).

[194] The vdW-DF-BEEF performance is not asserted, even if it is also now implemented in the QE code suite. The idea of that design is to seek system-optimized exchange partners for the nonlocal-correlation description, but that idea does not lend itself easily to broad testing and a fair comparison in the fixed-parameter benchmarking strategy that we use.

[195] A. D. Boese and J. M. L. Martin, *Development of Density Functionals for Thermochemical Kinetics*, J. Chem. Phys. **121**, 3405 (2004).

[196] S. A. Seidl, B. Kretz, C. Gehrmann, and D. A. Egger, *Assessing the Accuracy of Screened Range-Separated Hybrids for Bulk Properties of Semiconductors*, Phys. Rev. Mater. **5**, 034602 (2021).

[197] G. Santra and J. M. L. Martin, *What Types of Chemical Problems Benefit from Density-Corrected DFT? A Probe Using an Extensive and Chemically Diverse Test Suite*, J. Chem. Theory Comput. **17**, 1368 (2021).

[198] N. Gerrits, S. V. Egidius W. F. Smeets, A. D. Powell, K. Doblhoff-Dier, and G.-J. Kroes, *Density Functional Theory for Molecule-Metal Surface Reactions: When Does the Generalized Gradient Approximation Get It Right and What to Do If It Does Not*, J. Phys. Chem. Lett. **11**, 10552 (2020).

[199] C. Linderälv, A. Lindman, and P. Erhart, *A Unifying Perspective on Oxygen Vacancies in Wide Band Gap Oxides*, J. Phys. Chem. Lett. **9**, 222 (2018).

[200] A. Hashemi, C. Linderälv, A. V. Krasheninnikov, T. Ala-Nissila, P. Erhart, and H.-P. Komsa, *Photoluminescence Line Shapes for Color Centers in Silicon-Carbide from Density Functional Theory Calculations*, Phys. Rev. B **103**, 125203 (2021).

[201] A. Patra, S. Jana, L. A. Constantin, and P. Samal, *Efficient Yet Accurate Dispersion-Corrected Semilocal Exchange–Correlation Functionals for Non-Covalent Interactions*, J. Chem. Phys. **153**, 084117 (2020).

[202] Y.-R. Jang and B. D. Yu, *Hybrid Functional Study of the Structural and Electronic Properties of Co and Ni*, J. Phys. Soc. Jpn. **81**, 114715 (2012).

[203] P. Janthon, S. Luo, S. M. Kozlov, F. Vines, J. Limtrakul, D. G. Truhlar, and F. Illas, *Bulk Properties of Transition Metals: A Challenge for the Design of Universal Density Functionals*, J. Chem. Theory Comput. **10**, 3832 (2014).

[204] W. Gao, T. A. Abtew, T. Cai, Y.-Y. Sun, S. Zhang, and P. Zhang, *On the Applicability of Hybrid Functionals for Predicting Fundamental Properties of Metals*, Solid State Commun. **234–235**, 10 (2016).

[205] S. Mallikarjun Sharada, R. K. B. Karlsson, Y. Maimaiti, J. Voss, and T. Bligaard, *Adsorption on Transition Metal Surfaces: Transferability and Accuracy of DFT Using the ADs41 Dataset*, Phys. Rev. B **100**, 035439 (2019).

[206] A. Perrichon, E. J. Granhed, G. Romanelli, A. Piovano, A. Lindman, P. Hyldgaard, G. Wahnström, and M. Karlsson, *Unraveling the Ground-State Structure of* $BaZrO_3$ *by Neutron Scattering Experiments and First-Principles Calculations*, Chem. Mater. **32**, 2824 (2020).

discussion of self-interaction-error impact on G21EA and WATER27.

[207] K. Momma and F. Izumi, VESTA 3 for Three-Dimensional Visualization of Crystal, Volumetric and Morphology Data, J. Appl. Crystallogr. **44,** 1272 (2011).

[208] A. V. Myshlyavtsev and P. V. Stishenko, Potential of Lateral Interactions of CO on Pt (111) Fitted to Recent STM Images, Surf. Sci. **642,** 51 (2015).

[209] L. Schimka, J. Harl, A. Stroppa, A. Grüneis, M. Marsman, F. Mittendorfer, and G. Kresse, Accurate Surface and Adsorption Energies from Many-Body Perturbation Theory, Nat. Mater. **9,** 741 (2010).

[210] I. Grinberg, Y. Yourdshahyan, and A. M. Rappe, CO on Pt (111) Puzzle: A Possible Solution, J. Chem. Phys. **117,** 2264 (2002).

[211] R. Olsen, P. Philipsen, and E. Baerends, CO on Pt (111): A Puzzle Revisited, J. Chem. Phys. **119,** 4522 (2003).

[212] A. Stroppa, K. Termentzidis, J. Paier, G. Kresse, and J. Hafner, CO Adsorption on Metal Surfaces: A Hybrid Functional Study with Plane-Wave Basis Set, Phys. Rev. B **76,** 195440 (2007).

[213] M. Alaei, H. Akbarzadeh, H. Gholizadeh, and S. de Gironcoli, CO/Pt (111): GGA Density Functional Study of Site Preference for Adsorption, Phys. Rev. B **77,** 085414 (2008).

[214] A. Stroppa and G. Kresse, The Shortcomings of Semi-Local and Hybrid Functionals: What We Can Learn from Surface Science Studies, New J. Phys. **10,** 063020 (2008).

[215] P. Lazić, M. Alaei, N. Atodiresei, V. Caciuc, R. Brako, and S. Blügel, Density Functional Theory with Nonlocal Correlation: A Key to the Solution of the CO Adsorption Puzzle, Phys. Rev. B **81,** 045401 (2010).

[216] P. Janthon, F. Vines, J. Sirijaraensre, J. Limtrakul, and F. Illas, Adding Pieces to the CO/Pt (111) Puzzle: The Role of Dispersion, J. Phys. Chem. C **121,** 3970 (2017).

[217] B. Hammer and J. K. Nørskov, Electronic Factors Determining the Reactivity of Metal Surfaces, Surf. Sci. **343,** 211 (1995).

[218] B. Hammer and J. K. Nørskov, Why Gold Is the Noblest of All the Metals, Nature (London) **376,** 238 (1995).

[219] G. J. Blyholder, Performance of a Non-Local van der Waals Density Functional on the Dissociation of H_2 on Metal Surfaces, J. Phys. Chem. **68,** 2772 (1964).

[220] The functional choice also has an indirect effect on the adsorption description and the competition between sites. This is because the XC-functional choice sets the lattice constant, which, in turn, adjusts the electronic structure.

[221] A. Togo and I. Tanaka, First Principles Phonon Calculations in Materials Science, Scr. Mater. **108,** 1 (2015).

[222] K. Toyoda, Y. Nakano, I. Hamada, K. Lee, S. Yanagisawa, and Y. Morikawa, First-Principles Study of Benzene on Noble Metal Surfaces: Adsorption States and Vacuum Level Shifts, Surf. Sci. **603,** 2912 (2009).

[223] K. Toyoda, Y. Nakano, I. Hamada, K. Lee, S. Yanagisawa, and Y. Morikawa, First-Principles Study of the Pentacene/ Cu(111) Interface: Adsorption States and Vacuum Level Shifts, J. Electron. Spectrosc. Relat. Phenom. **174,** 78 (2009).

[224] K. Berland, S. D. Chakarova-Käck, V. R. Cooper, D. C. Langreth, and E. Schröder, A van der Waals Density Functional Study of Adenine on Graphene: Single-Molecular Adsorption and Overlayer Binding, J. Phys. Condens. Matter **23,** 135001 (2011).

[225] H. Kruse, P. Banas, and J. Sponer, Investigations of Stacked DNA Base-Pair Steps: Highly Accurate Stacking Interaction Energies, Energy Decomposition, and Many-Body Stacking Effects, J. Chem. Theory Comput. **15,** 95 (2019).

[226] B. J. Cafferty, I. Gallego, M. C. Chen, K. I. Farley, R. Eritja, and N. V. Hud, Efficient Self-Assembly in Water of Long Noncovalent Polymers by Nucleobase Analogues, J. Am. Chem. Soc. **135,** 2447 (2013).

[227] G. P. Smith, T. P. Fraccia, M. Todisco, G. Zanchetta, C. Zhu, E. Hayden, T. Bellini, and N. A. Clark, Backbone-Free Duplex-Stacked Monomer Nucleic Acids Exhibiting Watson-Crick Selectivity, Proc. Natl. Acad. Sci. U.S.A. **115,** E7658 (2018).

[228] C. Riplinger, P. Pinski, U. Becker, E. F. Valeev, and F. Neese, Sparse Maps—A Systematic Infrastructure for Reduced-Scaling Electronic Structure Methods. II. Linear-Scaling Domain Based Pair Natural Orbital Coupled Cluster Theory, J. Chem. Phys. **144,** 024109 (2016).

[229] M. Kim, T. Gould, D. Rocca, and S. Lebeque, Establishing the Accuracy of Density Functional Approaches for the Description of Noncovalent Interactions in Biomolecules, Phys. Chem. Chem. Phys. **22,** 21685 (2020).

[230] D. R. Hamann, Optimized Norm-Conserving Vanderbilt Pseudopotentials, Phys. Rev. B **88,** 085117 (2013).

[231] M. Schlipf and F. Gygi, Optimization Algorithm for the Generation of ONCV Pseudopotentials, Comput. Phys. Commun. **196,** 36 (2015).

[232] K. F. Garrity, J. W. Bennett, K. M. Rabe, and D. Vanderbilt, Pseudopotentials for High-Throughput DFT Calculations, Comput. Mater. Sci. **81,** 446 (2014).

[233] G. Makov and M. C. Payne, Periodic Boundary Conditions in Ab Initio Calculations, Phys. Rev. B **51,** 4014 (1995).

[234] X. Gonze, M. Rignanese, M. Verstraete, J. M. Beuken, Y. Pouillon, R. Caracas, F. Jollet, M. Torrent, G. Zerah, M. Mikami, P. Ghosez, M. Veithen, J. Y. Raty, V. Olevanov, F. Bruneval, L. Reining, R. Godby, G. Onida, D. R. Hamann, and D. C. Allen, A Brief Introduction to the ABINIT Software Package, Z. Kristallogr. **220,** 558 (2005).

[235] J. Tao, Y. Jiao, Y. Mo, Z.-H. Yang, J.-X. Zhu, P. Hyldgaard, and J. P. Perdew, First-Principles Study of the Binding Energy between Nanostructures and Its Scaling with System Size, Phys. Rev. B **97,** 155143 (2018).

[236] I. Dabo, B. Kozinsky, N. E. Singh-Miller, and N. Marzari, Electrostatics in Periodic Boundary Conditions and Real-Space Corrections, Phys. Rev. B **77,** 115139 (2008).

[237] J. Wittea, J. B. Neaton, and M. Head-Gordon, Push It to the Limit: Comparing Periodic and Local Approaches to Density Functional Theory for Intermolecular Interactions, Mol. Phys. **117,** 1298 (2019).

[238] L. Cartz, S. R. Srinivasa, R. J. Riedner, J. D. Jorgonsen, and T. G. Workton, Effects of Pressure on Bonding in Black Phosphorus, J. Chem. Phys. **71,** 1718 (1979).

[239] S. Racioppi, P. Lolur, P. Hyldgaard, and M. Rahm, A Density Functional Theory for the Average Electron Energy, 10.26434/chemrxiv-2022-22s75-v2.